

TECHNISCHE UNIVERSITÄT BERGAKADEMIE FREIBERG



Fakultät: Geowissenschaften, Geotechnik und Bergbau

Studiengang: International Master of Science in Advanced Mineral Resources Development

THEMA DER MASTERARBEIT:

Possibilities of Utilizing Cutting Force Analysis for Sensing Different Lithologies during Mechanical Excavation

bearbeitet von: Herrn Pherto Rimos

zur Erlangung des akademischen Grades: Master of Science

1. Prüfer/Gutachter: Prof. Dr. Carsten Drebenstedt
2. Prüfer/Gutachter: Dr. Taras Shepel

Übergabetermin des Themas: 01.01.2017

Abgabetermin der Masterarbeit: 01.07.2017


Vorsitzender des Prüfungsausschusses


Prüfer

Declaration of Authorship

I declare in lieu of an oath that this Master Thesis is my original work and no part of it has been copied from any other source except where due acknowledgement is made. I have mentioned all the sources used and that I have cited them correctly according to established academic citation rules. Any use of the works of any other author, in any form, is properly acknowledged at their point of use. I give permission for my assessment response to be reproduced, communicated compared and archived for the purposes of detecting plagiarism.

I know that a false declaration will have legal consequences. This paper was not previously presented to another examination board and has not been published.

Date: _____

Pherto Rimos: _____

Acknowledgment

Foremost I would like to express my wholehearted thankfulness and gratefulness to the God for his divine blessing, which gives me passion and strength to accomplish this Master Thesis successfully. Apart from the Eternal, I would take the opportunity to show my indebtedness to the people, who have been instrumental to carry out this Master Thesis.

Firstly, my earnest gratitude goes to my advisor Prof. Dr. Carsten Drebenstedt for the continuous support of my study and research, for his patience, motivation, enthusiasm, and immense knowledge. His guidance helped me in all the time of research and writing of this thesis.

Finally, I must express my very profound gratitude to my parents for providing me with unfailing support and continuous encouragement throughout my years of study and through the process of researching and writing this thesis. This accomplishment would not have been possible without them

This work is financially supported by the European Union (European Social Fund) and the Saxonian Government (Grant No. 100270113) and part of the Project *InnoCrush - Dynamic methods of mechanical excavation and comminution for high selective production chains in Critical Raw Materials in Saxony*.



Table of Contents

INTRODUCTION	1
Chapter 1 Issue Analysis	2
1.1 Principle of Excavation with point attack picks	2
1.2 Influencing parameters to the cutting process	4
1.2.1 Properties of the rock	4
1.2.2 Cutting and cutting tool parameters	7
1.3 Mechanical Excavation Application	11
1.3.1 Existing Mechanical Excavation Machines	11
1.3.2 Automation technologies of mechanical excavation	14
1.4 Formulating the Research Problem	18
Chapter 2 Material	19
2.1 Equipment	19
2.1.1 The cutting machine	19
2.1.2 Hand-held X-Ray Fluorescence Analyzer (hXRF)	21
2.2 Specimen	24
2.2.1 Geology	25
2.2.2 Sample preparation	27
2.3 Conditions of the experimental study	27
2.3.1 Set up	28
2.3.2 Element measurement set up	29
2.3.3 Cutting process set up	30
Chapter 3 Method	33
3.1 Cutting Force	33
3.1.1 Moving average	34
3.1.2 Investigated parameter	35
3.1.3 Description of the cutting force process	36
3.2 Element measurement process	37
3.2.1 Kriging estimator	38
3.2.2 Hardness of the mineral	38
3.2.3 Mineralogy	40
3.2.4 Description of the element measurement	41

Chapter 4 Result	42
4.1 Cutting force	42
4.1.1 Influence of cutting depth.....	44
4.1.2 Accuracy of the model.....	46
4.2 Element Presence.....	49
4.2.1 Element presence analysis	49
4.2.2 Correlation element presence and cutting resistance.....	52
Chapter 5 Conclusion and Outlook	57
Bibliography	59
List of Figure	67
List of Tables.....	69
List of Abbreviations.....	70
Annex Table of Contents.....	72

INTRODUCTION

The world population is growing faster per annum, and mineral consumption will increase as well as more consumers enter the market for minerals. Additionally, as wealth is increasing in many parts of the world, the consumption per capita is increasing as well. Mineral producers have the obligation to supply this continuously increasing demand. At the same time, rich deposits that are easy to access become more and more depleted. Rising environmental standards and objections against the mining industry as a whole put additional pressure on companies. This results in the need for a drastic increase in the efficiency of mineral producing chains.

Recently, there are two of the most economical methods of excavation: mechanical excavation and drill and blast. Today, mechanical excavation takes an increasing share in the excavation industry as an alternative to conventional drill-blast. This technology is not only used in mining industry, but also in the civil industry for tunneling projects all over the world [1]. This happens, because mechanical excavation methods have some advantages over drill and blast methods. For instance, mechanical excavation can operate as a continuous operation that can reach high production rates. Does not require explosives handling, and blast fume ventilation, is less impact to the surrounding rock mass and does not influence adjacent communities by vibrations. Therefore, cutting tool technology and its development will determine the future mechanical excavation.

One major contributor to increase the efficiency of these can be highly selective mining coupled with highly automated processes. The general results of this can be:

- Reducing waste ore / tailing materials by selective excavation
- Optimizing wear and maintenance
- Optimizing blending capabilities to increase the efficiency of enrichment steps
- Increasing work safety

In addition, many research have been done in order to increase the automated technology in mechanical excavation, like utilizing the infrared system or high definition camera to identify the material at the working face [2]. However, in accordance to increase the technology of mechanical excavation, this thesis shows another possibility to identify the difference materials by utilizing the cutting force information during the excavation.

Chapter 1 Issue Analysis

In the 20th century the mining industry established large-scale surface mining operations. Hartman (1987) published almost all nonmetallic minerals (more than 95%), most metallic ores (more than 90%), and a large fraction of coal (more than 60%) are mined by surface methods [3]. However, on the turn of the 21st century as near to surface and easy to mine mineral deposits become more and more depleted, the extraction of mineral raw materials faces upcoming challenges. Extracting the material will be more complicated and expensive, thus mining technology, equipment and mining systems for extracting complex deposits will have to be developed. Additionally, innovative mining technologies that apply high standards in health, safety, and productivity must be implemented.

Due to the current situation, research is being carried out to improve the existing systems. The new technologies have to be able to mitigate the risks of mining activities, also in the field of excavation. Excavation as the one of the first steps in the mineral process chain can have a huge influence towards the overall production chains effectivity. There are two methods of excavation commonly used in mining of hard rock: mechanical excavation and drilling and blasting. Even, both methods in the mining and civil industry, but the mechanical excavation is more rapidly improved over the blasting method. Therefore, mechanical excavation is continuously increasing in some universities and private industrial or governmental institutions in some countries [1]. In addition, mechanical excavation shows good synergy effects when being combined with automation technologies. This kind of technology promises significant increases in safety, production rates and increased selectivity.

1.1 Principle of Excavation with point attack picks

Mechanical excavation is widely used for rock fragmentation in civil and mining industry. The rock cutting mechanism was initially investigated in the early 1950s to obtain a deep understanding of the mechanical behavior of the rock. In General, mechanical excavation involves using a cutting tool as an indenter to break the rock [4] and divided into three stages: the building up of the stress field, formation of the crush zone, cracking and chipping of the subsurface materials. In Figure 1-1 shows a crushed zone near the tool top and transmitted into the intact rock.

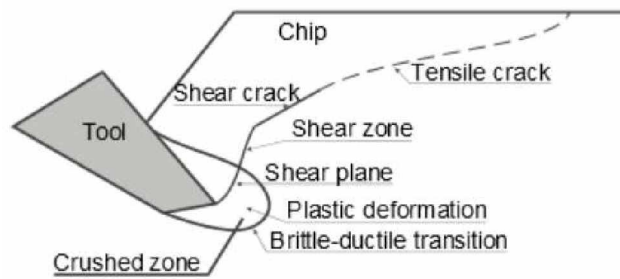


Figure 1-1: Failure mode during cutting [5]

Further understanding of the chip formation, at the beginning cracks are generated when the pick continuously presses the rock and some of these cracks propagate to the surface to form rock chips. After the chip is formed, the reaction forces lower again until the next chip is broken off. Secondary chipping and crushing are presented in the process (see in Figure 1-2). Figure 1-2 shows a typical force signal obtained during cutting tool cutting at constant depth. This cycle repeats continuously and is randomly occurred [6].

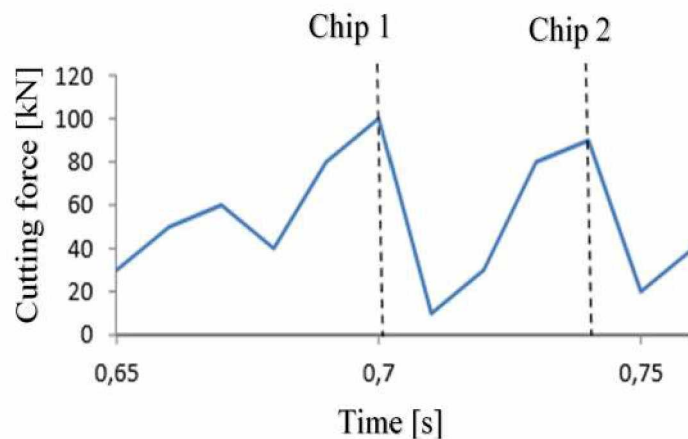


Figure 1-2: Scheme of chip formed in cutting force graph [7]

Experiments showed that the crushed zone near the cutting tip makes up for up to 90% of the total energy spent for rock cutting. For analyses of cutting force it is usual to resolve the resultant force acting on the tool into three orthogonal components: cutting force (F_c), normal force (F_n) or thrust force, sideways or lateral component forces (F_s) [5].

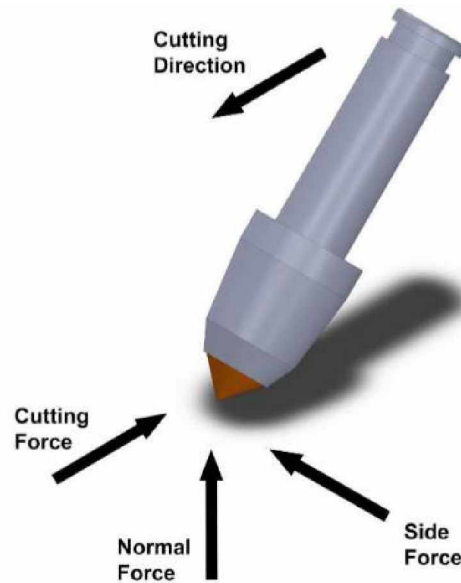


Figure 1-3: Pick force components [8]

1.2 Influencing parameters to the cutting process

To enhance understanding of rock breakage, several studies explain parameters that affect the mechanical rock excavation process. They can be divided into physical and mechanical properties of the rock and cutting tool parameters.

1.2.1 Properties of the rock

Uniaxial compressive strength (UCS)

Unconfined compressive strength (UCS) is the parameters of rock strength. This method is commonly used in mining for geotechnical purposes. UCS is formulated in Equation (1-1).

$$\sigma_c = \frac{F_{max}}{A} \quad (1-1)$$

Where:

σ_c = Uniaxial compressive strength [MPa]

F_{max} = Maximum force on the sample before failure [N]

A = Cross-section area of the sample [mm²]

In rock cutting, Evan investigated theoretically that compressive strength and tensile strength is influenced for determining cutting force with chisel or point attack tools. The criterion of the rock in consideration of UCS estimation is seen in Table 1-1.

Table 1-1: Simple ways of estimating UCS [9]

Term	UCS, MPa	Field Attribute
Extremely strong	>250	Chipped with a geological hammer
Very strong	100–250	Many blows with geological hammer to break core
Strong	50–100	More than one blow with geological hammer to break core
Medium strong	25–50	Cannot be scraped or peeled with pocket knife; core can be broken with single blow from hammer
Weak	5–25	Can be peeled with pocket knife; shallow indentation made by firm blow with point of geological hammer
Very weak	1–5	Crumbles under firm blow with point of hammer; can be peeled with a pocket knife
Extremely weak	0.25–1	Indented by fingernail

Brazilian tensile strength

Brazilian tensile strength is designed to measure the tensile strength. Tensile strength rock is influencing rock deformability. Brazilian strength is formulated by using equation (1-2).

$$\sigma_t = \frac{2P}{\pi L D} \quad (1-2)$$

Where:

σ_t = Brazilian tensile strength [MPa]

P = Maximum force on the sample before failure [N]

L = Length of the sample [mm]

D = Diameter of the sample [mm]

Cerchar abrasivity Index

This test is intended to indicate the degree of rock abrasivity, for classifying and predicting cutter wear rate and cost. In mechanical excavation, the cerchar-abrasivity-index is commonly used to predict models for TBM tunneling and for roadheaders excavations [10].

The Cerchar-Abrasivity-Index (CAI) is then calculated as equation (1-3).

$$CAI = 10 \frac{d}{c} \quad (1-3)$$

Where:

CAI = Cerchar-Abrsivity-index

d = diameter of wear flat [mm]

c = unit correction factor

The common classification for the Cerchar-Abrasivity-Index varies between 0 and 6 in seen in Table 1-2 [10]. The lower value is softer and less abrasive the rock for cutter, A CAI of 1 is soft, while 6 extremely abrasive.

Table 1-2: Classification the Cerchar-Abrasivity-Index [10]

CAI [0.1]	Abrasivity classification	Examples
0.0-0.3	not abrasive	organic material
0.3-0.5	not very abrasive	mudstone, marl
0.5-1.0	slightly abrasive	slate, limestone
1.0-2.0	(medium) abrasive	schist, sandstone
2.0-4.0	very abrasive	basalt, quartzitic sdst.
4.0-6.0	extremely abrasive	amphibolite, quartzite

Rock mass rating (RMR)

Rock mass rating is the method to describe the condition of the rock masses based on some parameters. To provide an overall rating of the rock classification, RMR system involves six parameters into account, they are [11]:

- The uniaxial compressive strength of the intact rock
- RQD
- Discontinuity spacing
- Condition of discontinuity surface
- Groundwater condition; and
- Orientation of discontinuities

Those parameters add together scores to obtain a value out of 100, for detail score of each parameter can be seen in Annex C. Overall, this rock classification method can be used for defining the cutting tool selection, force generation and wear effect to the bit.

1.2.2 Cutting and cutting tool parameters

Depth of cut

Cutting depth and spacing are two parameters which is affected specific energy in cutting process. Roxborough reported that specific energy decreased dramatically to a certain level with increasing depth of cut. This indicates that cutting efficiency of the pick improves as the depth of cut increases [12]. In Figure 1-4 shows the correlation between specific and depth of cut.

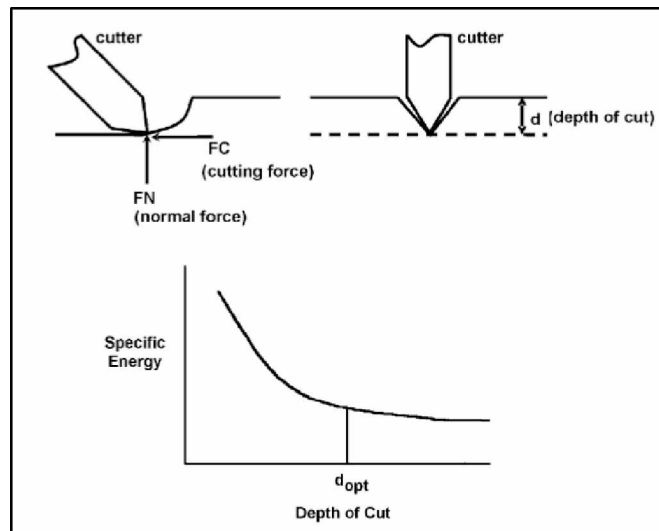


Figure 1-4: Relieved cutting mode (interaction between grooves) [12]

In real application, due to cutter spacing on cutting drum is fixed on the machine, the only way to excavate in optimum condition is by adjusting the desired depth of cut. The study investigated on 22 rocks and found that the optimum ration of spacing to depth of cut varies between 2 and 5 [12].

Spacing

Spacing between cuts affect cutting efficiency in the cutting process. the spacing between cuts should be superimposed to get the optimum result. As an illustration, Figure 1-5 shows general effect of cutter spacing on specific energy.

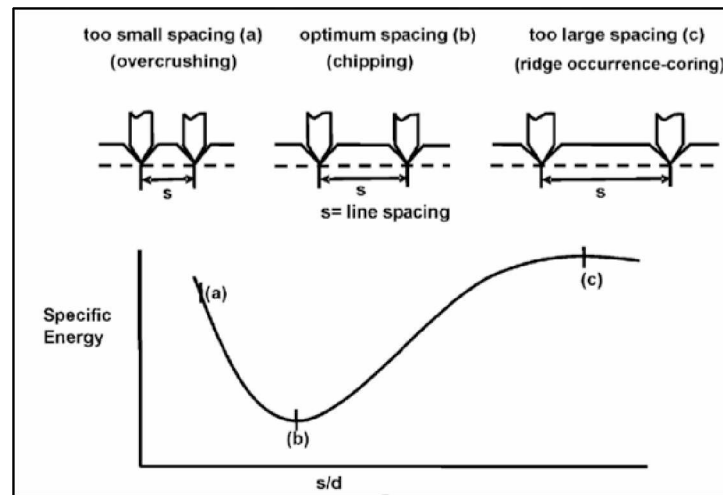


Figure 1-5: General effect of cutter spacing on specific energy [4]

The graphic shows, if the spacing between cuts is too close, the cutting is not efficient because the rock is over-crushed. Same result is happened, when the spacing between cuts is too wide, the cutting is not efficient due to the chip are not generated. In addition, the minimum specific energy is occurred in optimum ratio between spacing and depth of cut. It is between 1 and 5 times depth of cut [1, 4].

Cutting speed

This parameter is an important consideration in excavation process. For instance, cutting speed is not directly affected wear rate of the cutting tool. The effect of blunting of the cutting tool due to heat at the tool-rock contact area that generated from increasing the speed. Because of this the maximum of cutting speed should be limited to prevent excessive wear rate. Conversely, cutting speed has no influence on the magnitude of the force level [13].

Angles

In rock cutting practice, cutting tool should be set in suitable parameters. Otherwise, many disadvantages are overcome during the cutting process. Several studies showed the influence of angle act in consideration of the wear effect and efficiency of the rock breakage. Several angles affecting the performance of the cutting process are rake angle, clearance angle and attack angle (drag tools employed). The angles are defined in Figure 1-6.

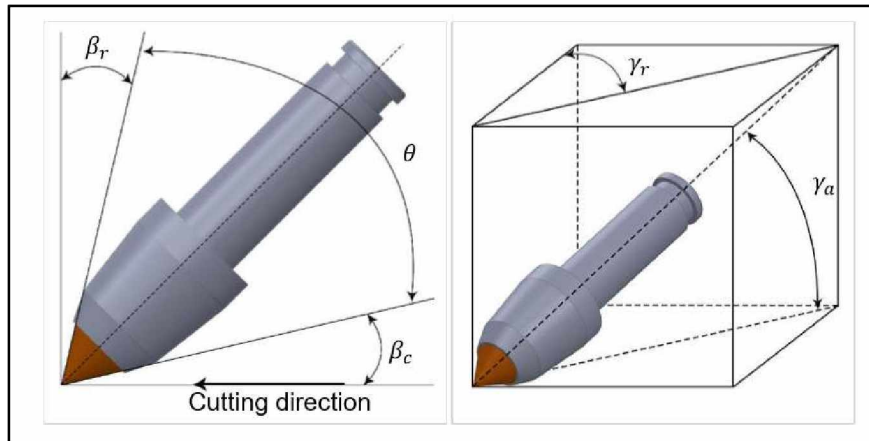


Figure 1-6: Cutting geometry of point-attack picks [8]

Where:

- θ = pick angle;
- γ_a = attack angle;
- γ_r = rotation angle;
- β_c = clearance angle;
- β_r = rake angle.

Clearance angle (β_c)

Clearance angle is defined as the angle between the back face of the pick and the plane parallel to the cutting direction. The study showed that the clearance angle affects the wear effect. When the cutting tool has a large clearance angle, it can reduce the wear effect and provides better efficiency. Furthermore, the force drop sharply after value of around 5° and stay sensibly constant [14].

Rake angle (β_r)

The rake angle is formed between the front of the pick and the line that is perpendicular to the plane parallel to the cutting direction. When the cutting tools has large rake angle, with the exception of the high-strength rocks, it can be cut the rock efficiently and that is necessity to have as large angle as possible. Furthermore, in high-strength rock, increasing the rake angle can cause the damage of the pick. Therefore, low or negative rake angles are necessity [15]

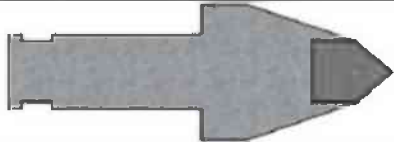
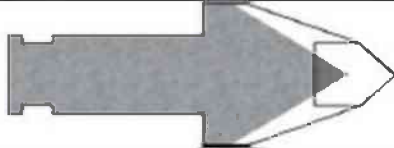
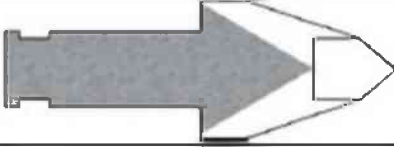



Attack angle (γ_a)

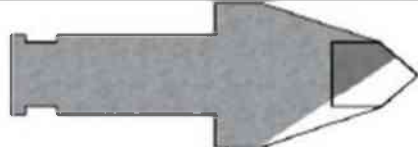

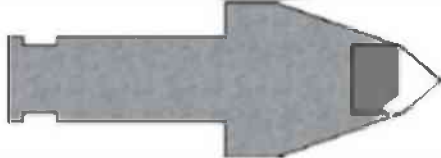
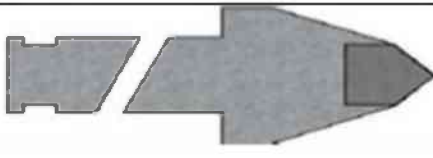
Attack angle is defined as the angle between the pick axis and the plane parallel to the cutting direction under the pick. In coal experiment, the study showed the most ideal angle of attack at $30^\circ - 45^\circ$ and hence less force is required to break the coal. In addition, the 60° attack angle is similar to the 15° . It concluded that too small and too large angle of attack can generate large force magnitude [16].

Wear of cutting tools

Wear properties of the rocks should be considered into account since they affect tool cutting performance and hence understanding about wear mechanism of cutting tools and the abrasivity of the rocks is required. For example, rates of tool wear are very dependent on structure, composition, and properties of the excavated material [1]. when the information of these parameters is incorrectly known, it can be directly affected to the cutting tools.

Table 1-3: Wear effect on conical cutting tool [7]

wear	Wear condition	Description
New cutting tool		New, unused cutting tool
Abrasive wear		Normal use: Uniform worn of hard metal and aggregate material.
		Total wear: Distribution of wear type is unknown
		Wear off the holder: wear focuses on the holder material
		Total outbreak: the outbreak of the tip due to faulty bedding
		Tip wear: Prominent flattening of the hard metal tip or wedge angle

		Asymmetrical wear: means one-sided wear of the chisel
wear through brittle fracture		Brittle fracture: brittle fracture is occurred within hard metal of the chisel, leading to partial or complete destruction
		Total outbreak: complete outbreak of the hard metal by failure of the connection between the tool holder and carbide.
		Chisel fracture: fracture at the below of chisel

1.3 Mechanical Excavation Application

The machines are often used for mechanical excavation in mining industry such as tunnel boring machines, continuous miners, drumshearers, roadheaders, etc. Even more, several new technologies are investigated to improve performance of mechanical excavation application.

1.3.1 Existing Mechanical Excavation Machines

Roadheaders

Comparing with TBM, roadheaders are the most flexible and mobile equipment, which commonly used in mining and civil industry. In mining application, roadheaders are widely used in underground mines to excavate soft to medium strength rocks. For example, this application are mostly used in coal mining, industrial minerals and evaporitic rocks. On the other side, this machine is also used for civil works, like building the infrastructure the railway, sewer, roadway, etc. Thus, this makes roadheaders as a common equipment in mining and civil industries. Moreover, its capital cost is generally low compared to the other mechanical excavators [17].

In the past few decades, many improvements have been applied for this machine. For example, the evolution of the cutting bits from simple chisel into robust conical bits.

Recently, heavy-duty roadheaders are able to cut rocks of up to 100 MPa uniaxial compressive stress [17] and that is might be applicable for hard rock excavation in the future.



Figure 1-7: Roadheaders [18]

Generally, components of the machine consist of a boom-mounted cutting head, a loading device usually involving a conveyor, and a crawler-travelling track to move the entire machine forward into the rock face [19]. The principle work for this equipment is by rotating drum mounted in line or perpendicular to the boom and wheel heads pressing the face of the wall.

Continuous miners

Continuous miners are also widely used in mining industry, especially at underground coal mines, but they can be applied in salt, potash and gypsum mines. Continuous miners have been existing since mid-1950s, since then the machine has been developed in size and some variation. For the cutting tools, they are generally fitted with conical bits. In soft thick coal seams, the production rate for this machine reaches 1,000 t/h. Continuous miners can operate in seam as low as 1 m to 5 m [20].

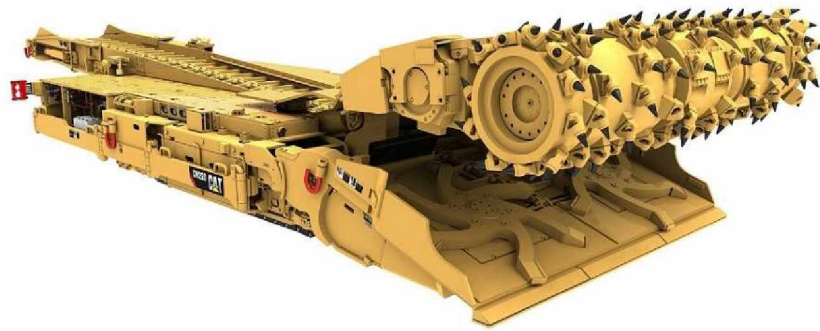


Figure 1-8: Continuous miners [21]

Longwall shearers

For longwall operation, longwall drum shearers are well known for extracting the materials, especially commonly used for coal mines. Performance for this machine for reserve recoveries up to 80%. Similar to continuous miners, drum shearers can operate in seams as low as 1.5 m to 6 m. Furthermore, the production rate can achieve 5,000 t/h at the high cutting speed, it is about 0.83 m/s. For breaking the material, they use conical bits arranged in spiral pattern. Even more, special drums are used along with stronger bits and lower cutting speed to apply for harder roof and floor formation. Besides coal mines, the machines are applied in trona or potash mines [20].



Figure 1-9: longwall shearers [22]

integrated signal processor calculates the coordinate of the coal seam and transfer them to the control of the machine, which is used for the next step excavation. To validate the image of heading face in consideration of geology and mine surveying, the company used additional software for visualization.

First intelligent roadheaders equipped with this sensor system are tested in operation at the Prosper-Haniel in Bottrop colliery [2].

Use of computer vision for automation of a roadheader in selective cutting operation

The research conducted by AITEMIN (Spain), CERCHAR and LAAS (France). They used a computer vision for sensing the mineral and its distribution at the cutting face. The technology used infrared range of the spectrum from the charge-couple device (CCD) solid state video cameras, which have high sensitivity. This device was integrated with a computer-controlled spectrometric analysis system to measure, store and process reflectance spectra. The study showed that color differences among the ores depend on the frequency characteristics of the spectrum and not on its level. After that, the Ore will be distinguished by the spectrums shape [27].

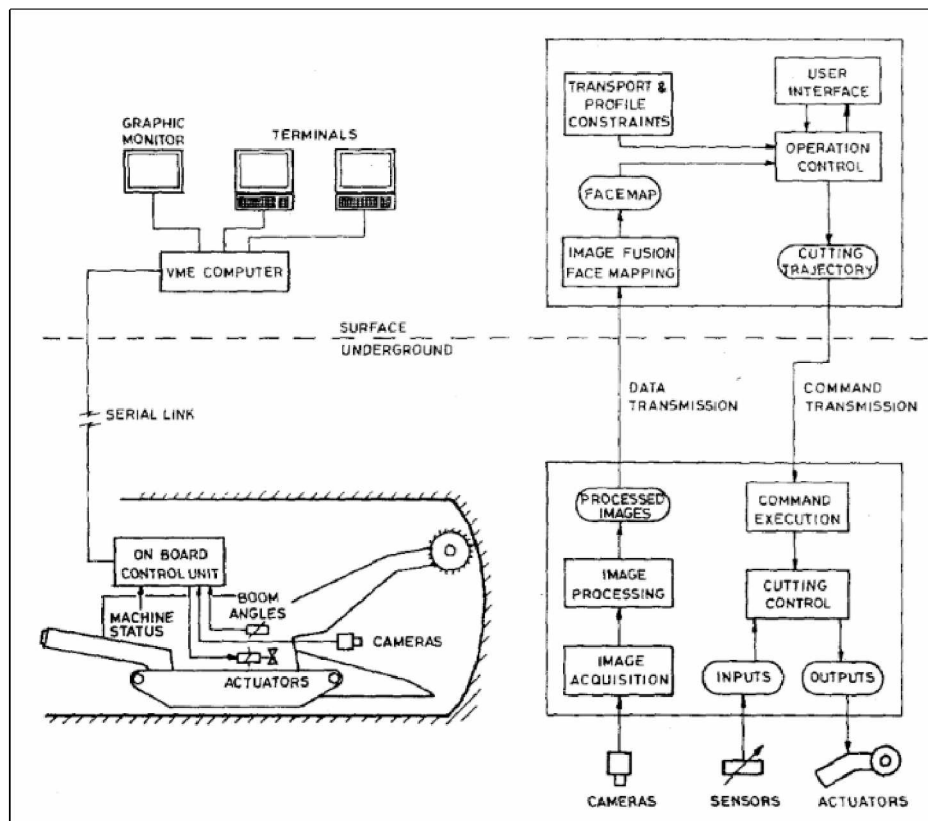


Figure 1-11: Control system structure [27]

In addition, the control system consists of two computer configurations: a real-time control unit located on the roadheader, and a main unit located outside the mine. Those are connected with serial link 4 km long for communication, as shown in Figure 1-11.

To process of all data from cameras and sensors is occupied by control unit at the machine, and for cutting plans received from the main unit through actuators on electric and hydraulic equipment [27].

While conducting the project, some problems were found. For instance, low quality of the images from the camera, which showed insufficient resolution and poor color quality. Consequently, it could not be properly processed by the vision system. However, improvement of technology will soon produce cameras that are able to provide adequate quality of the images [27].

Disc cutter load monitoring and face monitoring in TBM-tunneling.

The experiment was tested at the chair of Subsurface Engineering, Montanuniversität Leoben. This study investigated the disk force measurement (see in Figure 1-12) in Tunnel Boring Machine to examine the process of rock breaking and behavior of the local rock for geotechnical characterization.



Figure 1-12: Disc cutter (left) and discs position in TBM (right) [28]

The disk force measurement is arranged almost in a line ($r = 0.7, 2.65, 4.2\text{m}$) in order to obtain as good a result as possible of the entire cross section of the tunnel (see in Figure

1-12). Briefly, the result showed measured normal force and the data will be interpreted to describe the real condition of the working face.

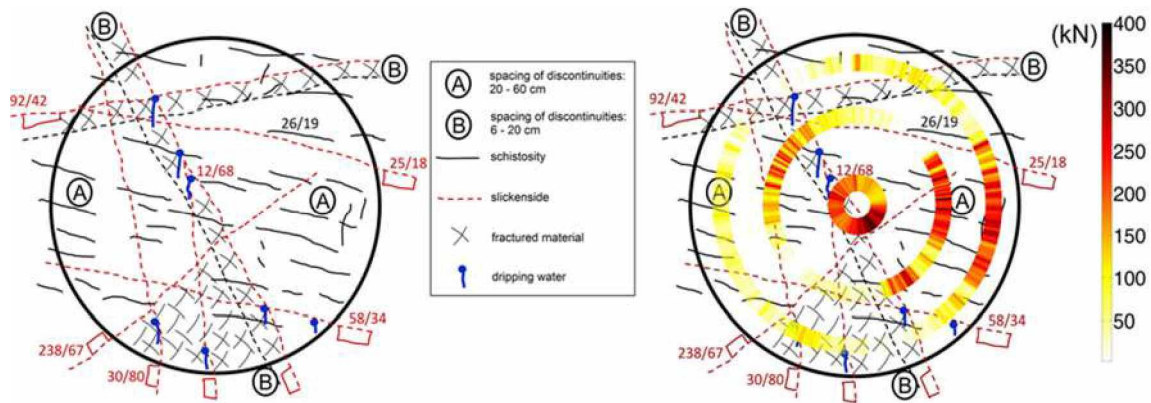


Figure 1-13: Geological mapping – *Schiefergneiss* (left) and results of measured normal force (right) [28]

The experiment shows the measured normal force, plotted on their respective position on measurement place. In Figure 1-13 shows the picture of geological map on the working face and measured normal force map. In a force map shows the range of colours from light to dark, it indicated the force magnitude in the working face from the tunnel, the force in right lower and left upper area are clearly higher than the opposite corner. This information is use for identifying a rock strength in the working face and the result is significantly represented the geological condition of the tunnel, when both of the picture are compared. It showed that the investigation of disk force measuring system provides a good possibility for geotechnical examination of the working face [28].

Automated drilling of Electronic Rig Control System (RCS).

Automated drilling is invented by Atlas Copco since 1998. This technology is operated by wireless tele-remote rig. Automating the control of various rig function replace human experience with the joysticks and switches with computerized inputs based on sensor and software and this allows the operator drill anywhere. Office-based software tool, such as Surface manager, complements automation with easy-to-use reporting interface. Surface manager displays the rig data in sensible layout to map drill usage, evaluate production statistic, track consumables and compare planned outcome against actual result. Those are plotted on charts and graph, this active management tools help with driller training and

provide decision-making support. While RCS performs each repetition with reliable precision and thus automated operating performance can be replicated shift after shift, no matter which human operator is monitoring the automation. The goals for this invented technology are enable operators to accomplish more goals safely and a few of the features being used to gain consistent and sustainable productivity [29].



Figure 1-14: Automated drilling (left) and controlling interface (right) [29]

1.4 Formulating the Research Problem

Based on the existing research and technologies above, the possibilities to implement automated technology are conceivable and that is the objective of this work is to investigate the possibility of utilizing cutting force analysis for sensing different materials within a sample that consists of different known rock types, which can be integrated with automated technology in the future. Within this framework, the focus lies on point attack picks due to their wide application range and simple use.

For the implementation of this objective, the following tasks are carried out within this work:

- Determination of dependencies of material changes on measured cutting forces F_C , F_S and F_N .
- Determination of influence of the increasing cutting depth and spacing between cuts towards the accuracy of the model.
- Obtaining additional information of the influence of the presence of certain minerals towards the cutting resistance of a certain known rock type (possibilities of sub-classification based on cutting forces)

Chapter 2 Material

This experiment was conducted to examine the influence of cutting force to sense difference material within rocks. Some equipment, instrumentation and the specimens that were used during the experiment are explained in this chapter.

2.1 Equipment

In this study, some laboratory equipment are used for conducting the experiment. These equipment are listed and described in the current chapter.

2.1.1 The cutting machine

All tests were investigated at Department of Mining Engineering, TU Bergakademie Freiberg, Germany. The cutting machine was designed and manufactured by ASW-GmbH Naumburg in 2008 for cutting experiment and type of the machines was used HXS 1000-50. General schematic view of the cutting machine used in the experiments is presented in Figure 2-1.

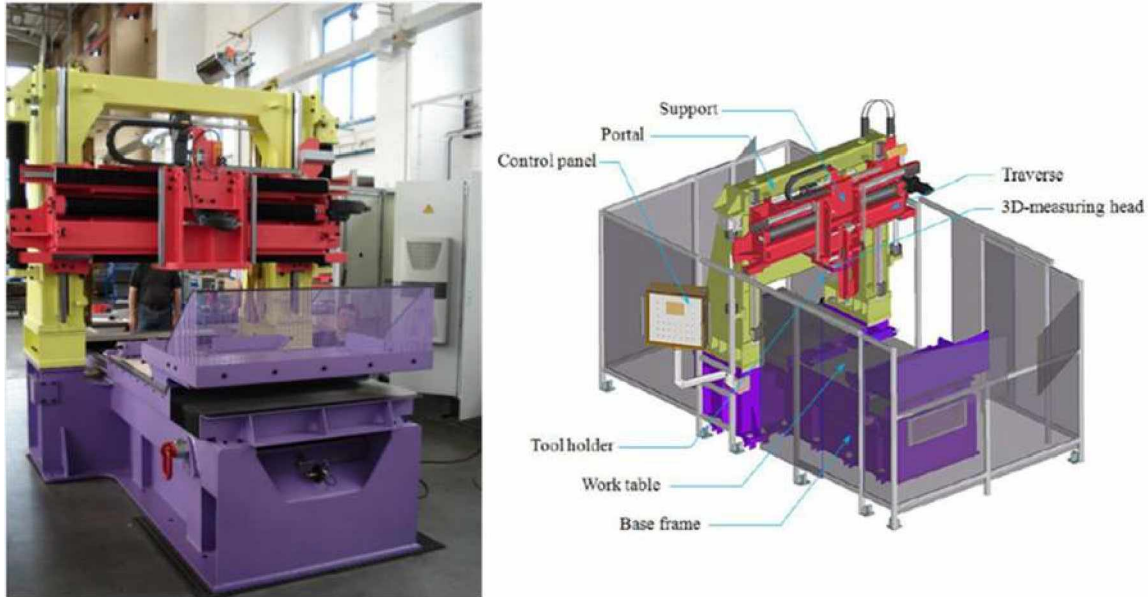


Figure 2-1: Cutting Machine HXS 1000-50 (left) and 3D model (right) [7, 8]

The machine consists of solid metal frame, three-dimensional force gauges, a laser scanner, a cutting table, a control panel, a tool holder. During the cutting process two main parts (cutting table and cutting) are moving. The cutting head moves along two axes, in y-axis

(lateral) and z-axis (vertical), and the cutting table moves only one direction, which moves on x-axis. Figure 2-2 shows the simplification of the axes moving direction.

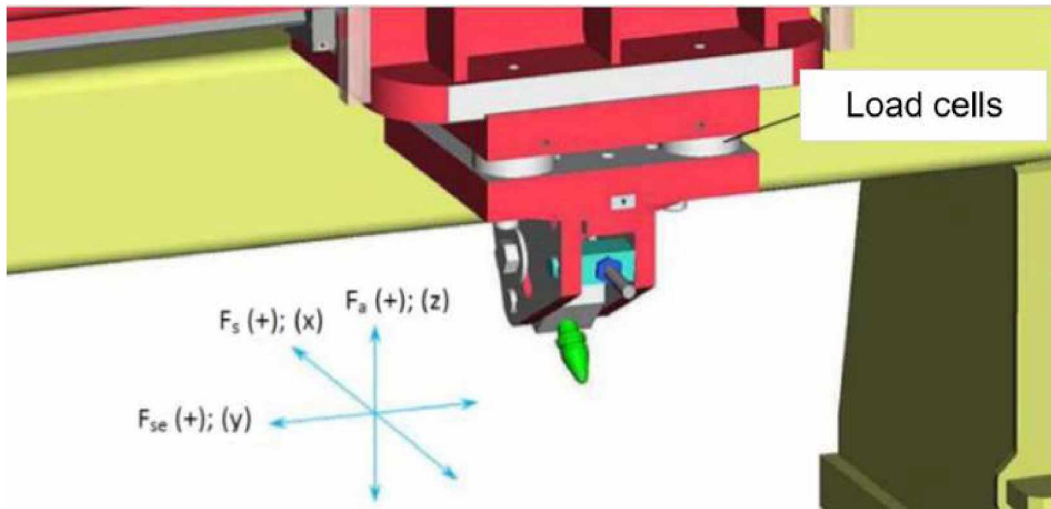


Figure 2-2: Force components of the HSX-1000-50 [8]

The setting for three axes are manually driven by control panel, included setting of depth of cut, spacing and cutting speed. For the specification, this machine can measure forces between the range from -50 to 50 kN and the error of the measurement is equal to 0.5% (0.25 kN). More detail concerning technical data of the cutting machine can be found in Annex B.

The cutting tool

The entire test is carried out with BSR 112 conical pick manufacture by BETEK. Material of the picks are made from steel and tungsten carbide material. This material is effectively fit to destroy the rocks. During the experiment, the pick diameter is modified to fit into the cutting head. The original picks have bigger diameter than the cutting tool head and thus the modification are required. In total, this experiment used four picks, one pick cut one type of the rock and thus every pick cut one rock in whole cutting process. In addition, to provide uniform wearing of the tip, the pick was rotated by 45 degrees after five cuts.

Data acquisitions

To record the data, a computer of type DEWE-5000 (see in Figure 2-3) was used. The computer uses the software package DEWESoft by Dewetron to store the measured data during the process. Seven channels (Figure 2-3) are included on the computer to capture the data: three channels measure X, Y, and Z coordinates of the cutting head, three channels

measures the force values F_C , F_S , and F_N (see also chapter 1.1, page 2 ff.) and the last channel is used for laser scanner measurements. When the cutting process is completely finished, the data obtained can be exported for other purposes into different file formats. The laser unit can scan the surface of the specimen determining distance from the unit to the surface of the sample with a precision of $\leq 70 \mu\text{m}$. With the use of such technology, coordinates of the surface can be mapped out, the cutting track investigated and the cut volume calculated [30].



Figure 2-3: Data acquisition channel (left) and Dewesoft Computer (right).

2.1.2 Hand-held X-Ray Fluorescence Analyzer (hXRF)

The element contents are measured with hand-held X-Ray Fluorescence analyzer, the type of the hXRF was used is Niton XL3t980 analyzer. See in Figure 2-4.



Figure 2-4: Hand-held X-Ray Fluorescence analyzer, Niton XL3

The X-ray fluorescence (XRF) spectrometer is an instrument used for non-destructive detection of major elements and selected trace elements during the investigation of rocks, ores and soils. A hand-held X-ray fluorescence (hXRF) analyzer allows operating on-site for immediate analysis.

The aim of the measurement is to determine a possible correlation of the applied cutting force with certain mineral phases. Because a direct measurement of mineral phases with an XRF device is not possible, the distribution of characteristic elements is used to receive the information about the mineral distribution. This, of course is only possible, when the occurring minerals are already known, it is just not known which mineral can be found where. Further explanations about the geology can be found in chapter 2.2, p. 24 ff.

X-Ray Fluorescence is an analytical technique to determine the elemental composition of a wide variety of materials. Sample which can be tested are e.g. metal alloys, rocks and ores. Basically, this device is designed from two major components: an x-ray source and a detector (see in Figure 2-5).

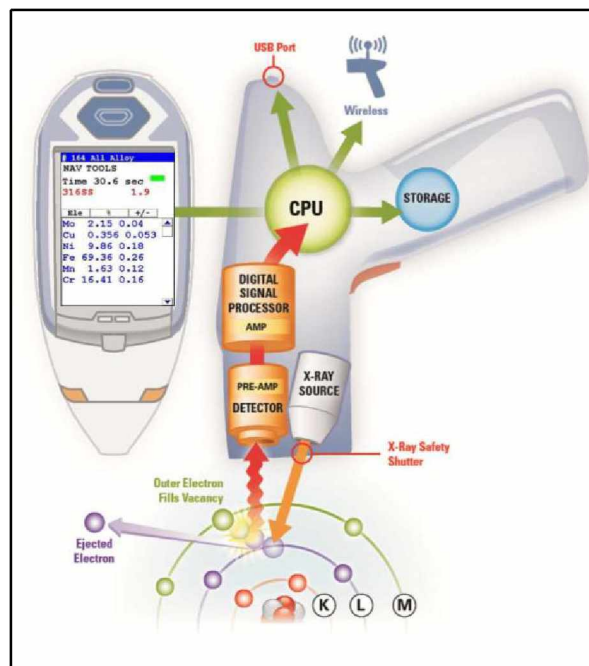


Figure 2-5: Scheme of hXRF structure and functional principle [31]

X-rays are generated by the X-ray tube and directed at the sample's surface. When the beam hits the atoms in sample, they react by generating the fluorescent X-radiation/fluorescence

radiation. The next step, detector is collected and processed the fluorescence radiation that emitted from the sample.

When the sample is radiated by high-energy photons, electrons from the inner orbital shells of sample are ejected from their orbital shell. Then, to restore the stability, an electron from higher energy level fills the electron vacancy. This caused the electron releasing energy in the form of a characteristic fluorescence radiation.

The measuring time depends on the matrix and the actual research aim. The heavy elements are given better result of the measurement in accordance with higher accuracy and reproducibility. The output of the measurement is displayed in ppm. The error in the output file (Excel file) describes the range (+/- measured value) of the reproducibility of the measurement on the same sample under the same measurement.

In addition, regards to the recalibration of measurement with hXRF, comparison of hXRF measurements on cup-filled ore-samples and chemical-analytical values from lab analysis is shown in the Figure 2-6.

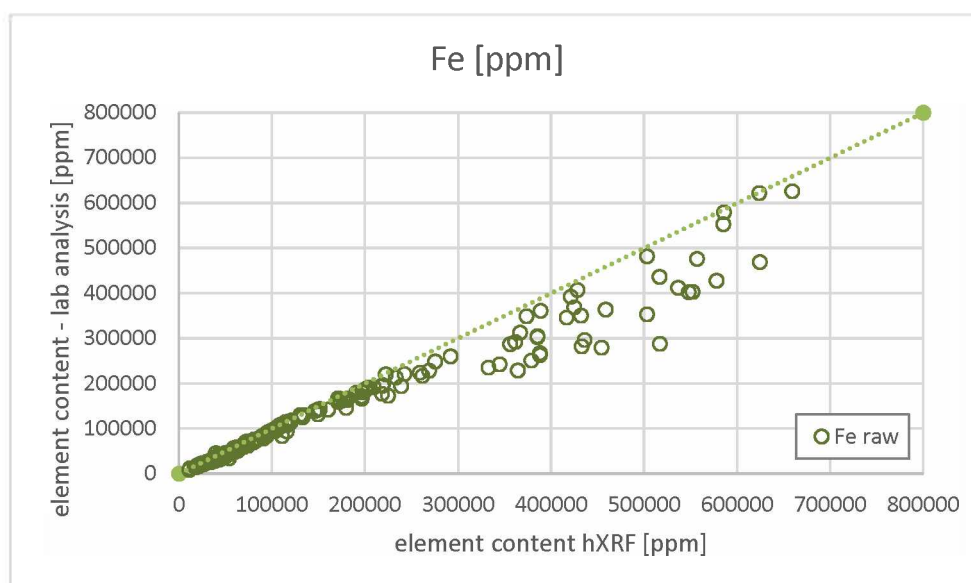


Figure 2-6: Congruency of the hXRF measured (Iron) on milled, cup-filled ore-samples and chemical-analytical values from laboratory analysis [32, 33][personal interview with M. Ussath, Scientific Assitant, TUBAF, Freiberg 25.08.17]

In Figure 2-6 showed an example measurement of iron, it is shown a relative replication of the element contents has good congruency with laboratory values. For iron, a relatively wide

scatter is shown at more than 300,000 ppm (30%). In addition, Lead is also shown a good congruency, because lead is a heavy element and therefore are generally measurable.

With regard to the other elements, especially for light elements, they are shown a relatively wide scatter and partially high deviation, such as calcium, silicon and zinc. For comparisons of the elements are presented in Annex I

2.2 Specimen

The rock for this experiment was collected from education mine “Reiche Zeche” of TU Freiberg, Germany. In total, there are four polymetallic rocks to be tested with the cutting test and dimension of each rock is around 30x14x18 cm (see in Figure 2-7).



Figure 2-7: Rocks before preparation

The rocks contain Quartz, Arsenopyrite, Pyrite, Pyrrhotine (marcasite), Galena and Sphalerite. Those minerals are typically abundant in Reiche Zeche. More information concerning the geology condition and location of the sample can be found in Annex D. The Location of the sampling site within the mine can be seen in Figure 2-8.

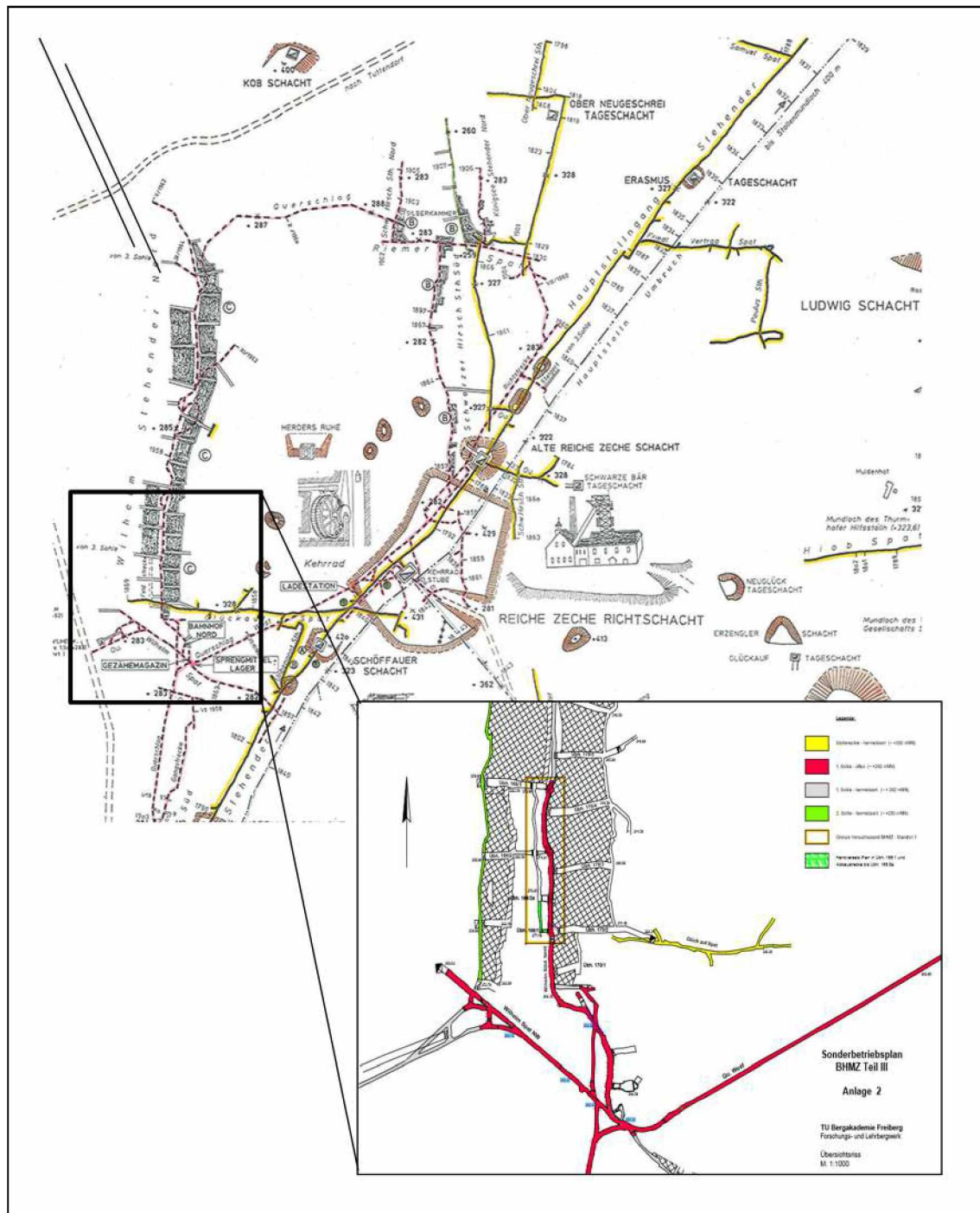


Figure 2-8: Sample location, Reiche Zeche, Freiberg, Germany [34] ,[Ralf Schlüter, Reiche Zeche staff]

2.2.1 Geology

Geology of Freiberg is one of the longest explored and one of the most famous deposits in the world. Mineral characterization is repeated mobilization of the raw material element, which led to a complicated pattern of material [35].

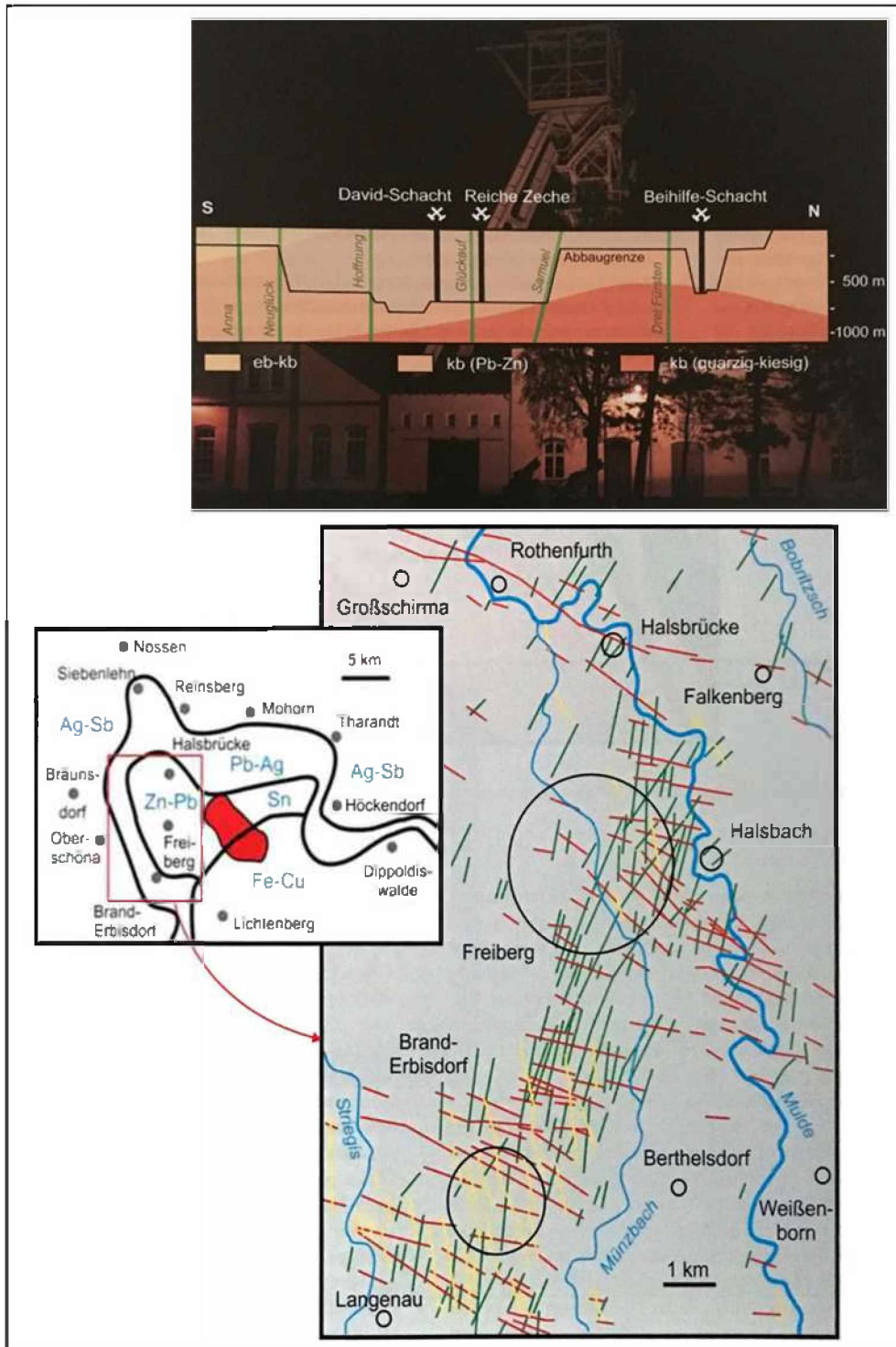


Figure 2-9: Vertical profile of Freiberg (above) and map of main metal raw material in Freiberg (under) [36]

There are four geological formations in this area: Quartz-Polymetallic-Association (kb-formation), Silver-sulfide-Association (eb-formation), The flourbarytic lead-association (fba-formation) and BiCoNiAg-association. According to formation structure, Freiberg is

formed from kb-formation (see in Figure 2-9), these include the economically important Lead-Zinc-Paragenes: Sphalerite-stannine-Chalcopyrite, Quartz-Galenite, Pyrite-Quartz [36].

2.2.2 Sample preparation

Preparation of the sample was conducted at the Institute of Mining and Special Civil Engineering of TU Bergakademie Freiberg. The preparation was designed by:

- Cutting the ore blocks in a way, that at least one clean and even surface was created
- inserting two rocks into one reinforced concrete frame, to prevent the specimens are easily destructed during the cutting process.
- A filling matrix in form of cement mortar was inserted, namely PCI Repaflo.

This material was chosen, as it has short harden time and its high-quality performance (class R4, DE0156/01), which show a compressive strength of 80 MPa after 7 days (detail information can be found in Annex I). The whole process of manufacturing the sample with hardening time was 10 days for each block. As a final result, the blocks have sizes to 57x74x25 cm³ (length x width x height). The prepared block can be seen in Figure 2-10.

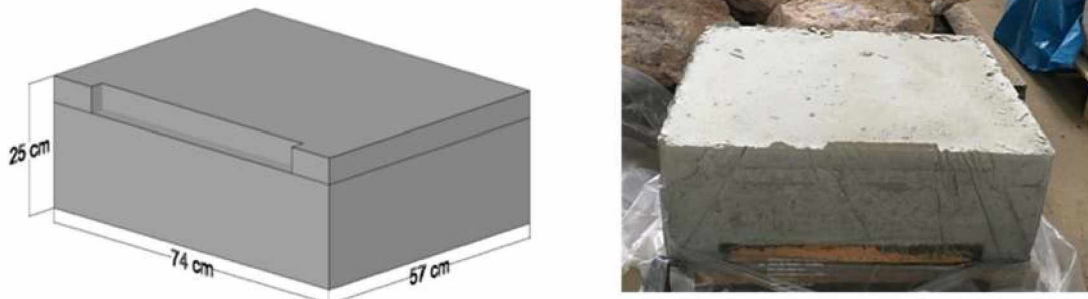


Figure 2-10: Dimension of prepared block

2.3 Conditions of the experimental study

When the sample is ready to be tested, the further experimental steps are divided into two main tasks. They were examination of the element content within the rock and cutting forces measurement. In addition, precondition set up for the sample was required. The description of each condition is presented in this section.

2.3.1 Set up

This step is intended further purposes, especially for obtaining the accuracy when the actual condition is considered in the calculation. Precondition set up were carried out as follows.

Define the offset between the coordinate of pick position and laser scanner point, because they have different position relative to the cutting head (where the coordinated are measured).

Table 2-1: Offset pick and laser coordinates

	X-Axis	Y-Axis
Pick Coordinates	257.6	342.2
Laser Coordinates	260.8	509.4
Offset	3.2	167.2

This is necessary, when both coordinate are needed in the calculation. As can be seen in Figure 2-11, for this study 4 points are recorded for further calculation.

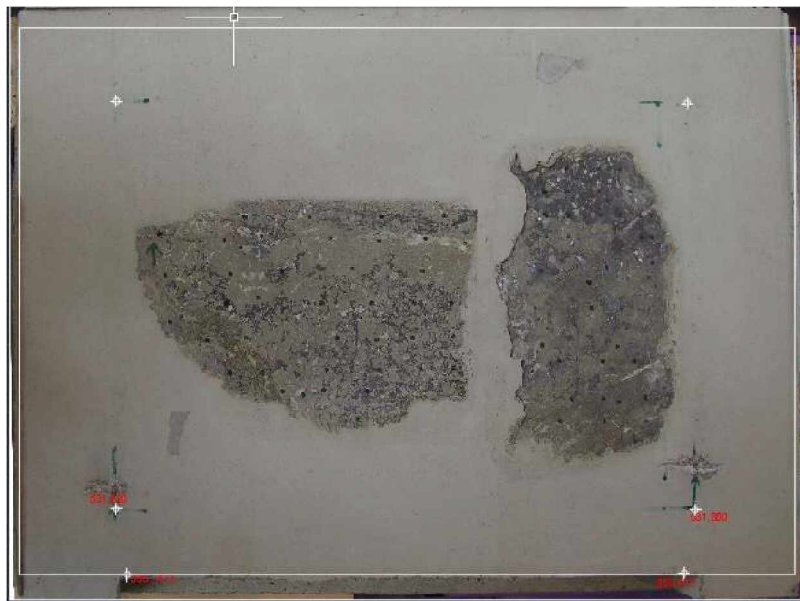


Figure 2-11: Reference point

Mark fix-points on the sample's surface. It allows for an alignment of a photograph to the machines coordinate system. This is a precondition for editing purposes such as aligning the pictures, eliminating distortion and scaling purposes. Figure 2-12 shows the additional points that are drawn on a sample.

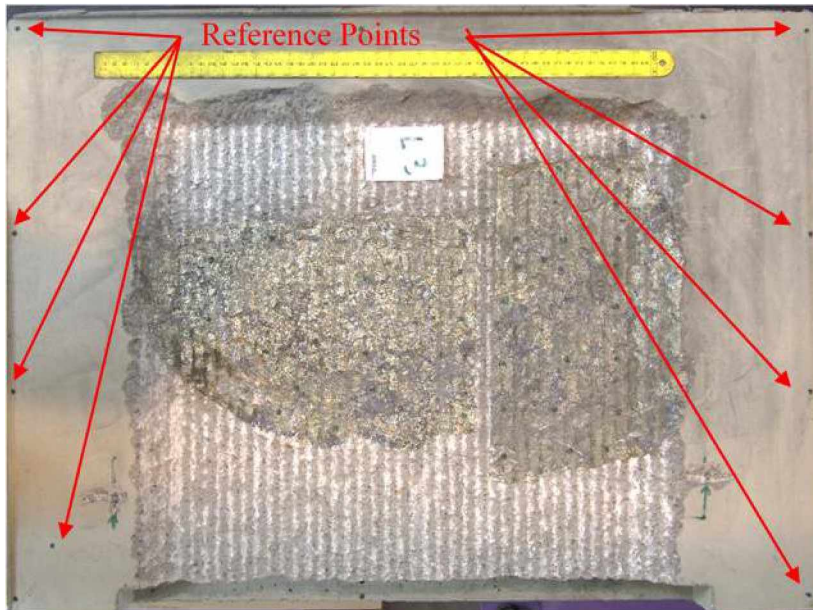


Figure 2-12: Scheme of additional points as references

Capture the digital image of the sample before and after test is necessary. This necessary for further processing. Record all the events before and after executions.

2.3.2 Element measurement set up

For measuring the element contents, the data was collected by X-Ray Fluorescent elemental analyzer (hXRF). Measurement of the element within the rock are applied every layer before the cutting process execution. This measurement is intended to examine the influence of the presence of certain minerals towards the cutting resistance of the rock.

The procedures to examine the points were same throughout the process. Firstly, the points should be determined by visual examination of the ore parts (see in Figure 2-13). The main minerals Pyrite, Sphalerite and Galena have a clear different visual appearance and hence can be easily distinguished. The points where chosen so that different mineralization zones could be measured. As a tradeoff between measurement effort and expected quality of results, it was chosen to do approx. 50 measurements per layer. The measurement of one point takes approx. 40 s without logging of coordinates and processing of the raw data.

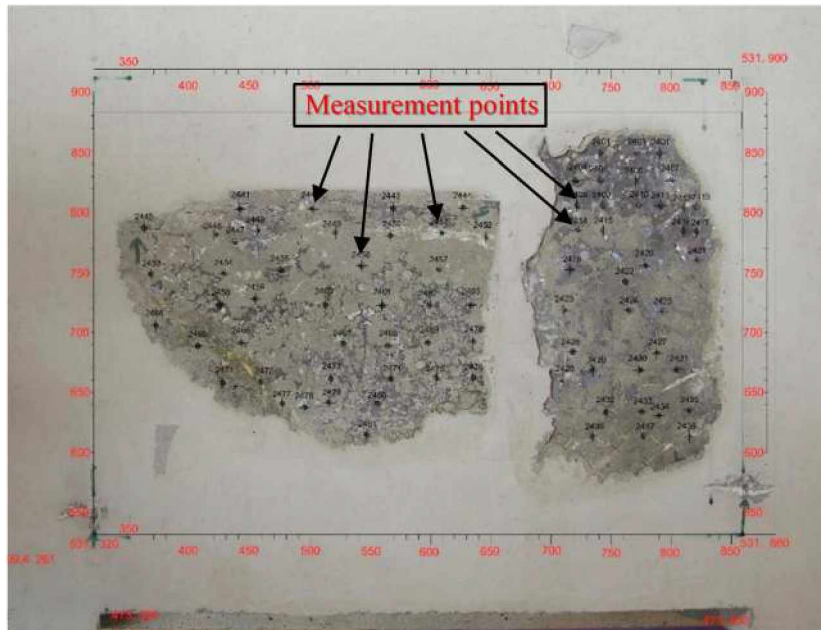


Figure 2-13: Measurement points

2.3.3 Cutting process set up

After all the samples are completely prepared, the next step is a cutting force execution. Before doing the test, initial setting for some parameters are required: i.e. attack of angle, cutting speed, depth of cut and spacing.

Angle of Attack

Angle of attack is a constant condition throughout the cutting process. The angle was set at 45° .

Cutting speed

The effect of the cutting speed was well explained in Chapter 2.3. For current experiment, the speed was set up at 0.1 m/s . It was set up as a constant condition throughout the cutting process.

Number of cuts

Number of cuts for each set is replicated at the most 5 times of cuts. Afterwards the pick was rotated. This was to prevent the wear effect that occur only in one spot of the pick. After all cutting lines in the first layer was completely cut, the next layer was cut in the quarry manner, this mean that the next layer should be directly cut under the second cut of the previous layer. (See in Figure 2-14).

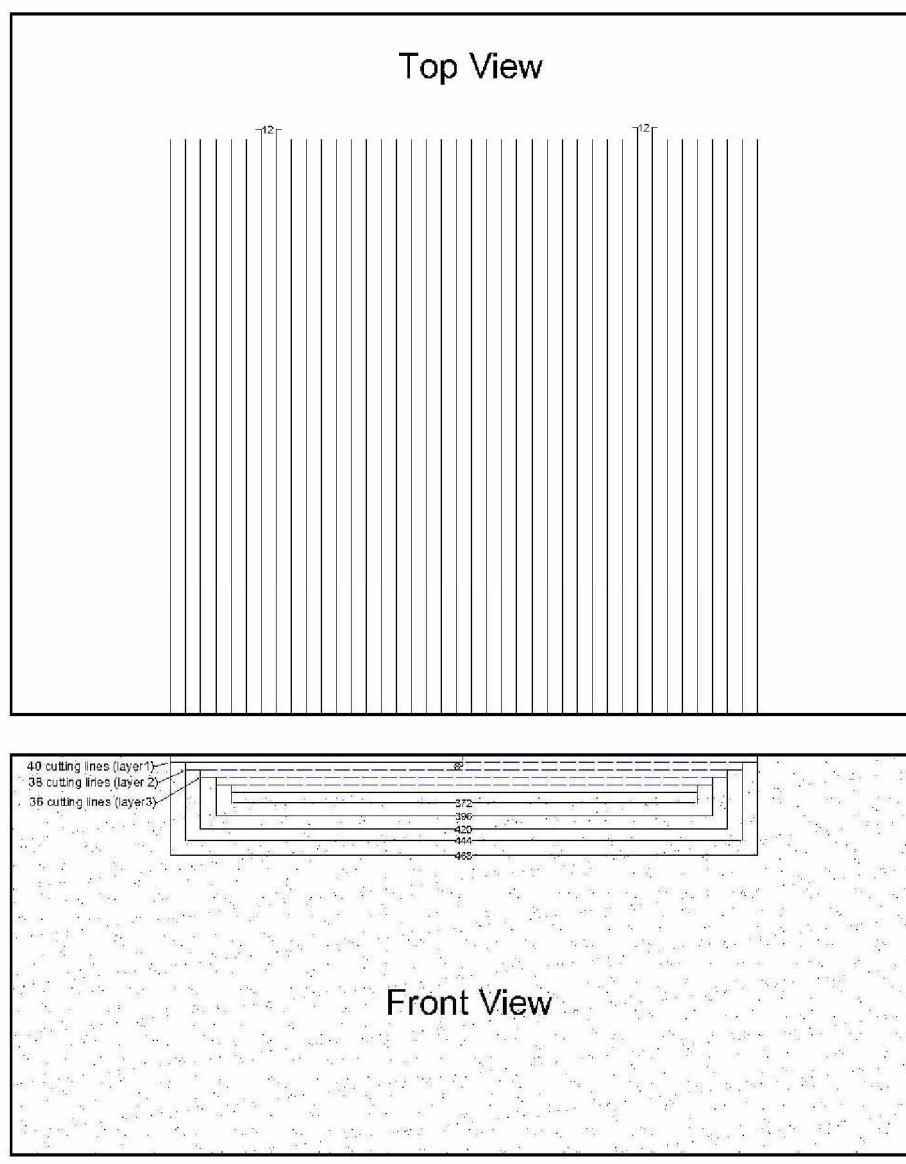


Figure 2-14: Cutting Lines

Cutting depth

The depth of cut in the perpendicular tests were divided into 2 different value. It summarized in Table 2-2.

Table 2-2: Depth of cut

Parameters	Block 1	Block 2
Cutting depth (mm)	4	6
	6	8

The consideration of the set up was referred to the previous research, in accordance with the rig capabilities.

Spacing

The line spacing is adjusted according to the cutting depth, which is commonly known as a ratio. For current experiment, the ratio was used by 2. Table 2-3 shows the spacing are used throughout the test.

Table 2-3: Spacing

Block	Layer	Spacing
1	Layer 1 - 7	8mm
	Layer 8 - 12	12mm
2	Layer 1 - 5	12mm
	Layer 6 - 9	16mm

Chapter 3 Method

As a result of the experimental study, cutting force and element distribution maps are obtained. The generated force maps are conducted to extensive analysis. In addition, the element distribution maps are also subjected to identify the influence of its presence regarding the cutting resistance of the rock. This chapter are presented the method for processing the measured data.

3.1 Cutting Force

During the cutting test, three forces act in the cutting direction (Figure 3-1) for rock destruction. These forces are cutting force, normal force and side force. As description cutting force acts in the direction of the cutting line, while perpendicular of this force is normal force. The side force acts perpendicular to the cutting path. For those, the pressure force acts on the rock, it is mainly responsible for the actual rock fragmentation.

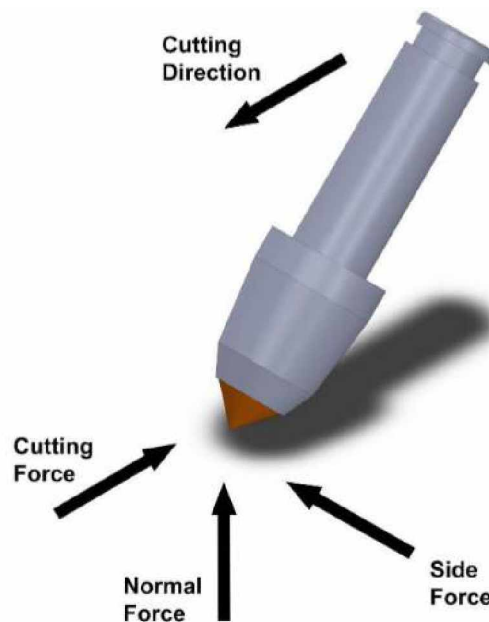


Figure 3-1: Forces acting on the cutting tool

To represent the influence of the cutting forces in rock breaking. Force distribution maps was chosen as a visualization of forces act on the rock. For creating force maps, measured data was collected by DEWE 5000, afterwards it was computed by additional *Surfer* software. The method was implemented by moving averaging gridding. This function is used to estimate the value of a surface at a specific grid note. It works as calculation of an average

of the known values nearby control point. After that, a complex approximation is calculated by averaging the value within the grid node's radius. To enhance understanding of moving average calculation, next chapter will explain the fundamental of moving average approximate.

3.1.1 Moving average

Current experiment is generated a huge number of cutting force data to be processed. For data processing one of the most common method to calculate data with variation of the noise is moving average. The main formula for this calculation is averaging of some sequential values of the series. In general, the procedure is computed by dropping the oldest observation and including the next observation [37]. For example, the three-point moving average at point x_1, x_2 and x_3 . These are averaged and plotted at the middle of the data values. Advancing one data calculation, it takes the next three points (x_2, x_3 and x_4) and the repeat the process. This is repeated until the end of the data series is reached. The illustration is then given by:

$$x_{mi} = \frac{x_i + x_{i+1} + x_{i-1}}{3} \quad (3-1)$$

Resulted curve of moving average depends on the data points in each averaging step, High of the data point, it is generated smoother appearance of moving average curve and that is caused losing some important detail in the data. Example of real data smoothed by simple moving averages are given in Figure 3-2 [38].

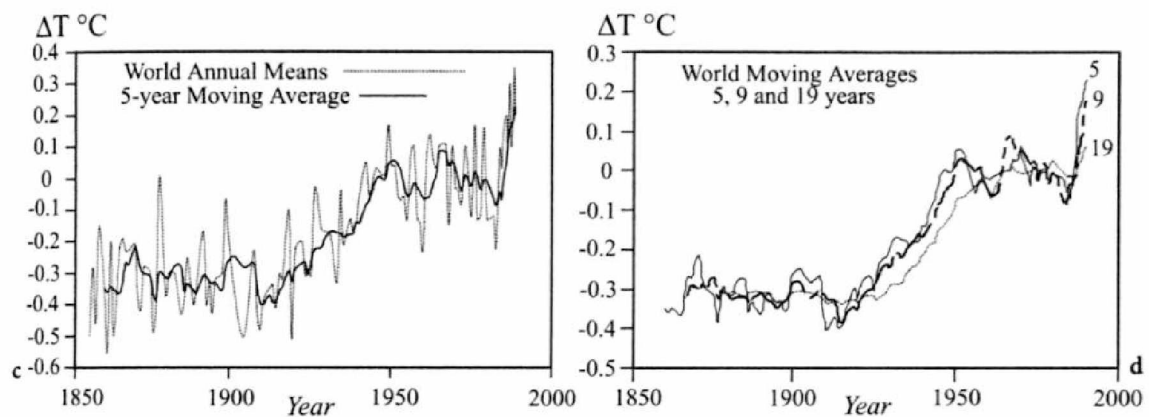


Figure 3-2: Global mean annual temperatures, smoothed by moving average [38]

For this study, the generate force maps were made by surfer software. By introducing gridding methods to create the maps, surfer has some gridding methods to control the

interpolation procedures. Some example gridding methods are available in surfer: Inverse Distance to a power, kriging, Natural neighbor, nearest neighbor, Polynomial Regression, etc.

For current study, Due to the huge number of data was generated and that is the moving average method is applicable to analyze the gathered data. Moving average is also known as smoothing interpolators instead of exact interpolators [39].

3.1.2 Investigated parameter

During the cutting process, cutting force magnitude are changing along the cutting direction. Different strength of the rock is mainly caused the cutting force has fluctuate trend. To identify different materials, cutting force maps are used to examine the accuracy of the maps.

Deviation of model

For this study, the deviation of the cutting force map will be evaluated. The deviation is determined by comparing the ration between ore recovery and ore contents within the rock. As this case, it is important to consider a dilution factor as well. This information is useful for further purposes in consideration of boundary limit adjustment.

In addition, for determination of the zone were divided into 3 categories (see in Figure 3-3): Zone 1 is determined as an ore recover zone, this zone is identified as an indicator for determining the limit boundary. Additionally, high percentage of ore recovery zone, it is indicated low deviation of the model. In zone 2 is called ore loss zone, this zone is formulated as the rest area of the ore recovery zone. The last zone is called dilution zone, this zone is the area not separated from the ore recovery zone, thus dilution area is also important to decide the minimum boundary limit. The Figure 3-3 shows the illustration of zones.

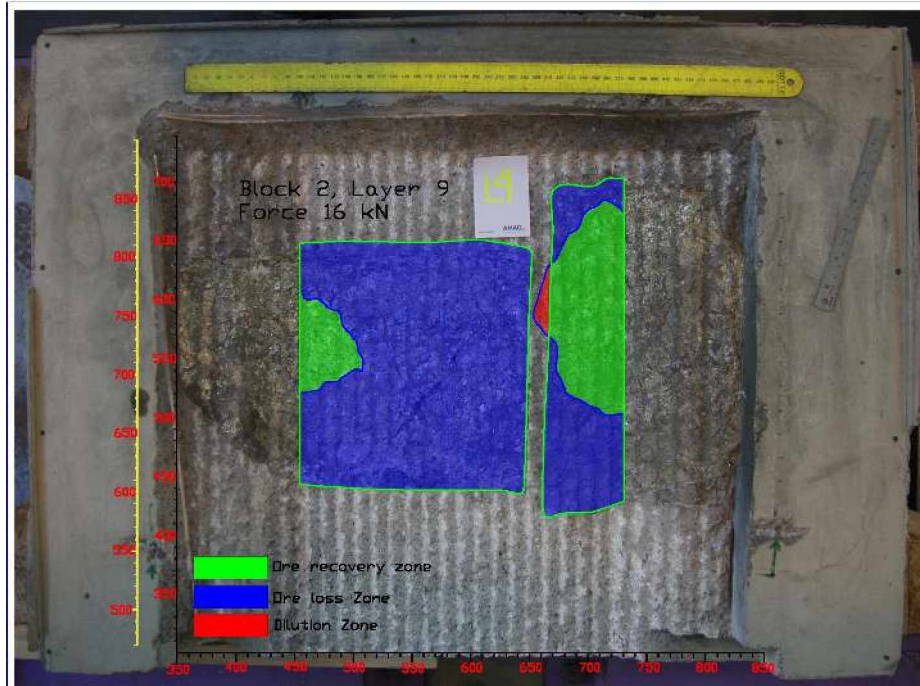


Figure 3-3: Scheme of mineral zones

To determine the accuracy of the cutting force maps, the following equation can be used:

$$\text{Accuracy of the force line} = \frac{\text{Area of ore recovery}}{\text{Area of Ore}} \quad (3-2)$$

Where:

Ore recovery zone	:	
Dilution zone	:	
Ore loss zone	:	

3.1.3 Description of the cutting force process

The cutting test was conducted as procedures of cutting process in Chapter 2.3.3. During the cutting process, sparkling of the fire are occurred in random time. These events were not given any influence in consideration of the peak force. Even more, heat of the pick was considerably low, still possible to hold with the hand. Furthermore, dust was increasingly formed when pick was cut the vein. On the other side, scattering of particles was directed sideways with respect to cutting direction while cutting the concrete.

Cutting test was divided into two different depth of cut in each block. Block 1 was stopped after cut 7 layers and the depth of cut for these layers were 4 mm. The next cut, the cutting depth was increased by 6 mm and was cut the next 5 layers. While changing the cutting depth, the block sides were trimmed to obtained wide opening space for cutting area (see in Figure 3-4). The same procedures were also implemented for block 2, but the condition of the cutting depth was 6 mm from layer 1 to layer 5 and it was changed by 8 mm from layer 6 to 9 layer.

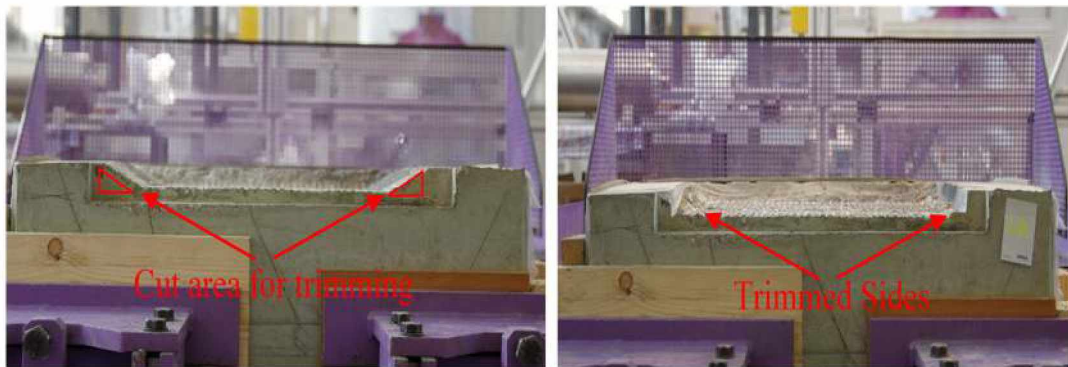


Figure 3-4: Untrimmed block (left) and trimmed block (right)

3.2 Element measurement process

In addition, resulted element maps are indented to represent as a visualization of element deployment on the rock. Interpolation of gathered data was conducted using the software surfer with kriging algorithm gridding. This method is suitable, because of the limited data from measurement. This function is used to estimate the value of the irregularly spaced data. The interpolation weight, the algorithm considers the spacing between the point to be interpolated and the data locations.

Even though the calculation was conducted by software, basic knowledge of kriging algorithm is necessary. In addition, this knowledge is also useful to interpret the element distribution map. As one of geostatistical method, kriging is widely used for linear regression method to estimate point values (or spatial averages) at any location of a region by computing a weighted average of the known values of the function in the neighbor of the point. There several common types of kriging, but the basic forms differ mostly on the assumptions regarding local or stationary domain mean [40].

3.2.1 Kriging estimator

In mining, geostatistics is widely used in the field of mineral resources and reserve valuation. This application is suited for mapping of surfaces from limited sample data and the estimation of the values at un-sampled location. Estimating values at those locations which have not been sample. This process is known as kriging. Kriging is a geostatistical gridding method that has proven useful and popular in many fields. This method produces visually maps from irregularly spaced data. Kriging attempts to express trends suggested in data, so that, for example, high points might be connected along a ridge rather than isolated by bull's-eye type contours.

All kriging estimators are but variants off the basic linear regression estimator $Z^*(u)$ defined as:

$$\begin{aligned} Z^*(u) &= \sum_{i=1}^n \lambda_i \cdot [z(u_i) - m] + m && \text{(3-3)} \\ &= \sum_{i=1}^n \lambda_i \cdot z(u_i) + \left[1 - \sum_{i=1}^n \lambda_i(u_i) \right] \cdot m \end{aligned}$$

where $Z(u_i)$ are data values and $Z^*(u)$ is the estimate. m is constant mean and assumed known and stationary (location independent), λ_i is kriging weight assigned to datum for estimation location [40]. Simple kriging can use either semivariograms or covariance, which are the mathematical forms to express autocorrelation.

For this study, the generate maps were made by surfer software. Surfer divided into two types of kriging: point kriging and block kriging. In general, both point kriging and block kriging generates an interpolated grid in surfer. Differences of this types is estimation of a certain point value. Point kriging estimates the value of the points at the grid nodes, while the block kriging estimates the average value of the rectangular blocks centered in the grid node and thus block kriging generates smoother contours. Furthermore, since Block Kriging is not estimating the value at a point, Block Kriging is not a perfect interpolator [39].

3.2.2 Hardness of the mineral

Hardness is measure the resistance to rock or minerals against an attacking tool. Some methods to determine of hardness are rebound test Hardness is determined using rebound tests (Schmidt hammer), indentation tests, (Brinell, Rockwell) or scratch tests (Mohs). The

common test to measure the hardness is Mohs scale. The last test is based on the fact that a mineral higher in the scale can scratch a mineral lower in the scale. Although this scale was established in the early of the 19th century it appeared that the increment of Mohs scale corresponded with a 60% increase in indentation hardness. Mohs designated ten minerals in the scale from softest to hardest and that is 1 to 10 respectively (see in Table 3-1). The following is listed the equivalent hardness [41]:

Table 3-1: Mohs Hardness Scale [41]

Mohs Scale	Mineral
1	Talc
2	Gypsum
3	Calcite
4	Fluorite
5	Apatite
6	Orthoclase
7	Quartz
8	Topaz
9	Corundum
10	Diamond

In terms of the mineral presence on the sample, the hardness of minerals is varying on the rock (Table 3-2). The following is listed some of minerals with its hardness:

Table 3-2: Mineral properties [42]

Mineral	Chemical Formula	Hardness
Galena	PbS	2.5
Sphalerite	(Zn,Fe)S	3.5
Pyrite	FeS ₂	6-6.5
Chalcopyrite	CuFeS ₂	3.5-4
Quartz	SiO ₄	7

3.2.3 Mineralogy

Pyrite

Pyrite is a sulfide mineral containing iron (Fe) and sulfur (S) as structural elements. It has a chemical composition of iron disulfide (FeS_2) and is the most common sulfide mineral. In general, finely crystallized pyrite minerals are relatively stable, and those are formed from sedimentary concentrations decomposes quickly. Pyrite is hard enough that it cannot be scratched with a nail [42].

Chalcopyrite

Chalcopyrite is a copper iron sulfide mineral, and its chemical formula is CuFeS_2 . It forms under a variety of conditions. Some is primary, crystallizing from melts as accessory minerals igneous. This mineral is naturally presented in a variety of ores, from huge masses to irregular veins and it is considered as the most important copper ore. Associated ore minerals include pyrite, sphalerite, bornite, galena, and chalcocite. Chalcopyrite serves as the copper source for many secondary mineral deposits. Different like pyrite, chalcopyrite is easily scratched with a nail [42].

Galena

Galena is a lead sulfide mineral with a chemical composition of PbS . In sedimentary rocks, it occurs as veins, breccia cements, isolated grains and as replacements of limestone and dolostone. It has a distinct silver color and a bright metallic luster and that is immediately noticed when pick up even small pieces. Galena is a very important mineral because it serves as an ore for most of the world's lead production. It is also a significant ore of silver.

Sphalerite

Sphalerite is a zinc sulfide mineral with a chemical composition of $(\text{Zn,Fe})\text{S}$. It is found in metamorphic, igneous, and sedimentary rocks. Sphalerite contains variable amounts of iron that substitutes for zinc in the mineral lattice. The iron content is normally less than 25% by weight. The amount of iron substitution that occurs depends upon iron availability and temperature, with higher temperatures favoring higher iron content. Sphalerite is a difficult stone to cut and polish. It is soft and it has cleavage.

3.2.4 Description of the element measurement

To illustrate the influence of the element presence within the rock, maps of the elements distribution are required. For this study, a hXRF Niton XL3t980 analyzer was used, the device is equipped with an Ag-Anode 50 kV X-ray tube and Silicon-Drift-Detector 8 mm spot. This The measurement was taken 40 s every point measurement by mining mode. The decision was used mining mode because the it was suited for higher density material, complex composition and also mining mode is suitable for metal or mineral analysis with concentration > 1%. Measured data are displayed as a spectrum, which is then calibrated to determine the content of element in the rock [43]. The error in the output file (Excel file) describe the range (+/- measured value) of the reproducibility of the measurement on the same sample under the same measurement.

Chapter 4 Result

The object of this study is to investigate the dependencies of material changes on measured cutting forces F_c , F_s and F_N . The parameters were involved the cutting depth and spacing between the cuts towards the accuracy of the model. Furthermore, this experiment is also investigated mineral presence to define its influence to cutting resistance. The description of the results is explained in this chapter.

4.1 Cutting force

The resulted force maps, the force diagrams are generated for the X, Y and Z direction. The resulted force maps have the X and Y coordinates from the data as an X-axis and Y-axis respectively. While Z -axis is represented of cutting force (F_c), side force (F_s) and normal force (F_N).

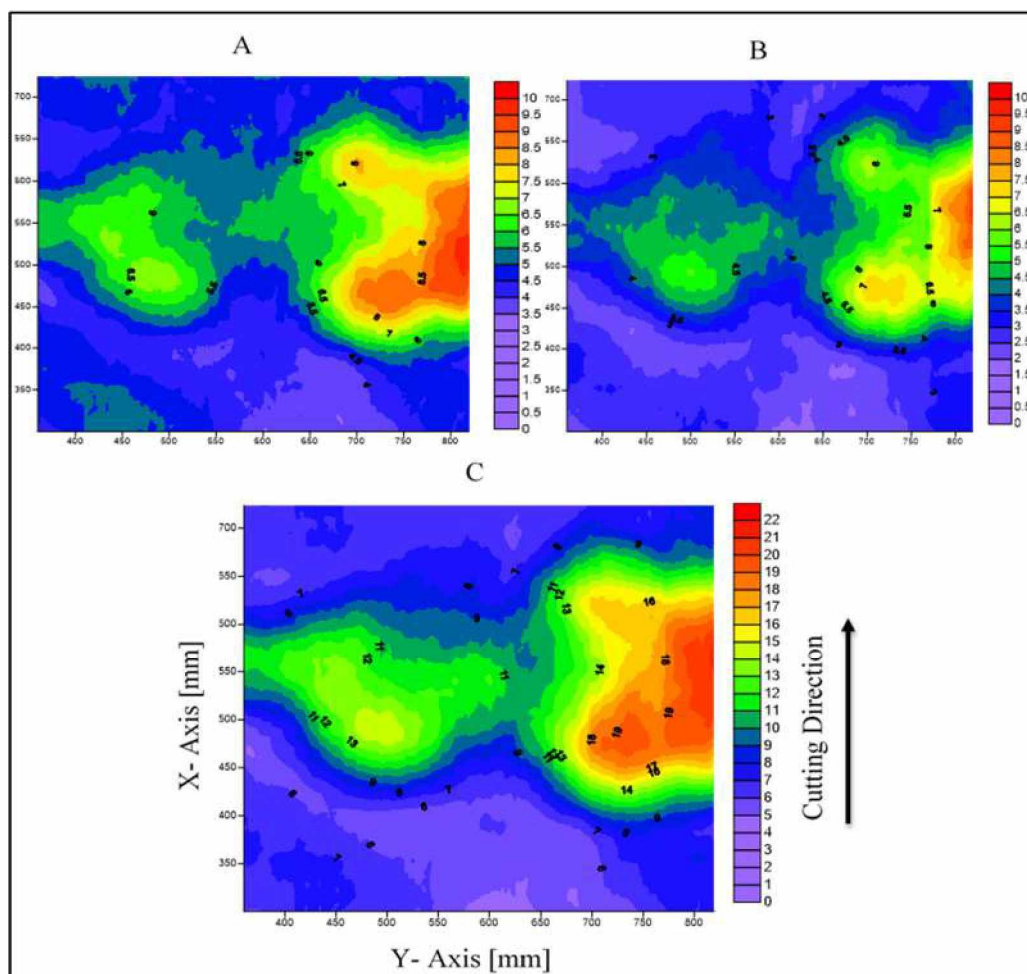


Figure 4-1: Set of force mapping: average cutting force (A), side force (B) and normal force (C) of block 2 layer 1 with depth of cut 6mm

Force maps in Figure 4-1 showed one set force value within the rock (F_C , F_S , and F_N). It can be seen the blue color indicates low forces, while red color indicates high forces. Three force maps have different scale of magnitude: cutting force map (A) has a higher force rather than the side force map (B) and the normal force map (C) has the highest force among three force maps. All sets of force mapping's scale have consistence pattern ($F_N > F_C > F_S$), this result is occurred for the whole force maps. Throughout this thesis, the term V1 and V2 is relatively name for vein 1 and vein 2 respectively (see in Figure 4-2).

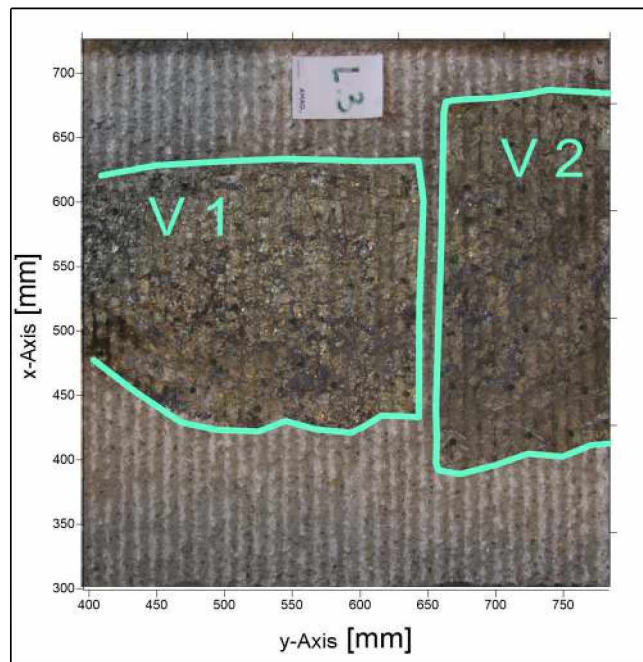


Figure 4-2: Block 2 layer 3

With regard to the cutting force value (see in Figure 4-3), block 1 showed that the force in vein 1 is higher than vein 2. It can be seen that the vein 1 showed cutting forces up to 13 kN and vein 2 showed range up to 6 kN. On the other side, block 2 showed vein 1 has a lower cutting force than vein 2, the results showed range of cutting force up to 6.5 kN and 9.5 kN respectively. The results throughout the thesis are shown consistency in consideration of the hardness in each vein. A possible explanation for this might be that the rocks are compounded from different mineral composition and mineral phases. For further investigation concerning of rock contains, it will be explained in the next section. Result of all force mapping are shown in Annex F.

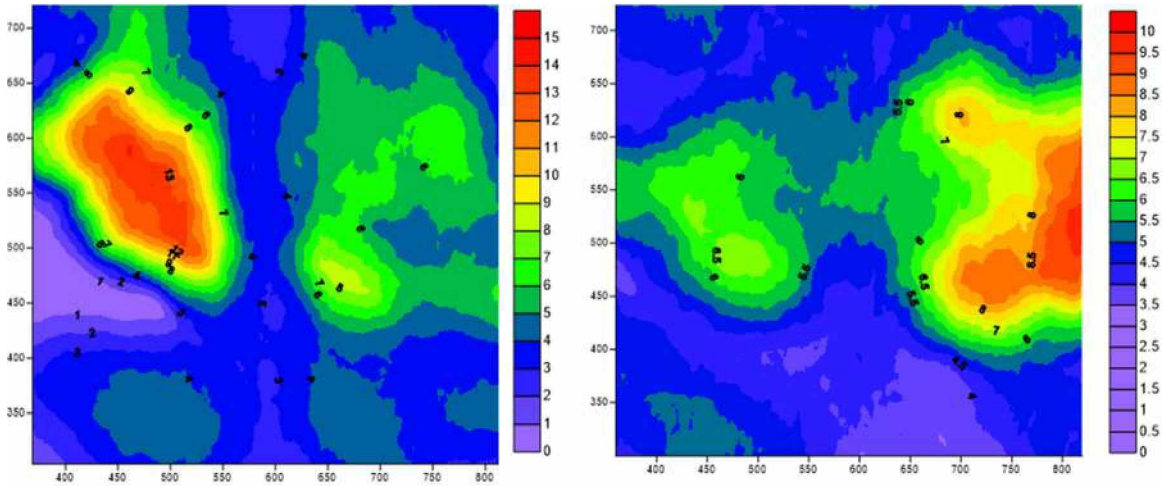


Figure 4-3: Average cutting force (F_c) block 1 (left) and block 2 (right)

4.1.1 Influence of cutting depth

Cutting force

Figure 4-4 show the mean cutting force block 1 with different cutting depth 4 mm and 6 mm. The forces of cutting process with depth 4 mm are 26 % lower than 6 mm. For block 2 by increasing the depth 2 mm likewise block 1, the mean cutting force 6 mm are 22% lower than cutting depth 8 mm.

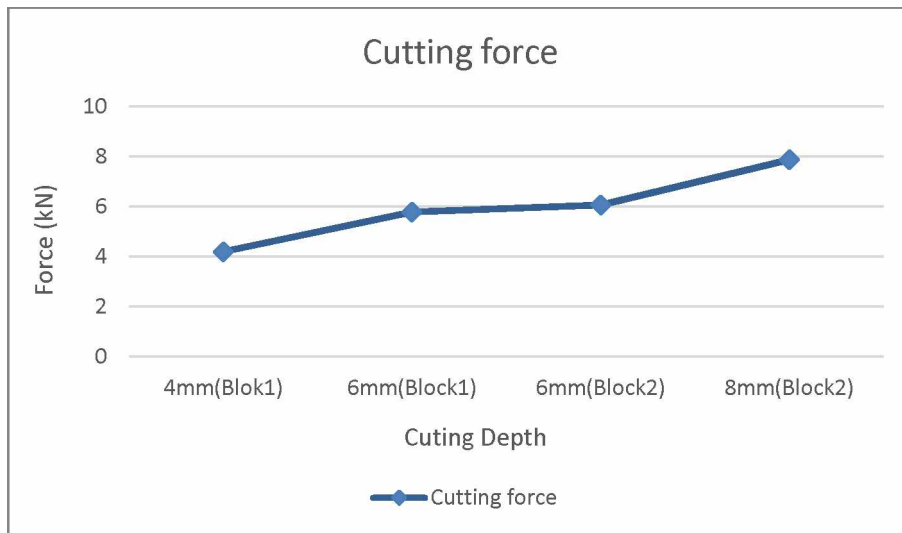


Figure 4-4: Cutting force force compared with cutting depth

Side force

As can be seen in Figure 4-5, the value of average side forces is lower than cutting and normal force. The result showed less the average force less than 6 kN. This means, with such condition and for current study, side force has less influence on the cutting resistance.

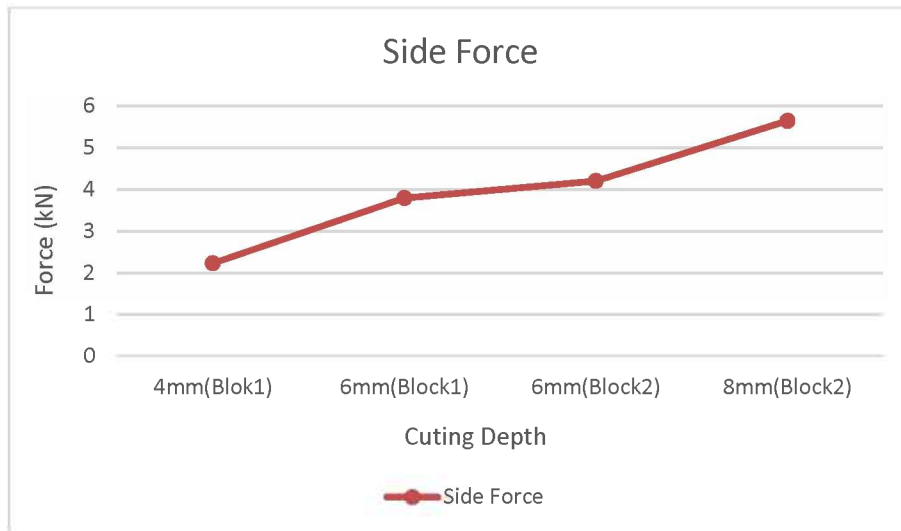


Figure 4-5: Average side force compared with cutting depth

Normal force

The according diagram can be seen in Figure 4-6. Average normal force in average repeat the behavior of cutting force. But overall, the value of mean normal force operates in the range 7.3 kN up to 12.4 kN. Average normal force Block 1 and block 2 was increased by around 21.7% and 23.5 % respectively.



Figure 4-6: Average normal force compared with cutting depth

The analysis of experiment based on the three components of the cutting forces F_C , F_S and F_N where evaluated. As a result, F_N showed the best potential utilization different rock types, while determining the mineral boundary of the rock. Therefore, normal force maps were chosen for determining the accuracy of the model.

4.1.2 Accuracy of the model

Since the three components of the cutting forces F_C , F_S and F_N were evaluated. As a result, F_N showed the best potential utilization different rock types. In addition, while determining the boundary of the rock, a correlation was found between ore and the concrete. The method can be implemented by overlaying between normal force map and actual picture. Figure 4-7 was represented the method to identify the accuracy of extracted-normal-force line related to actual block.

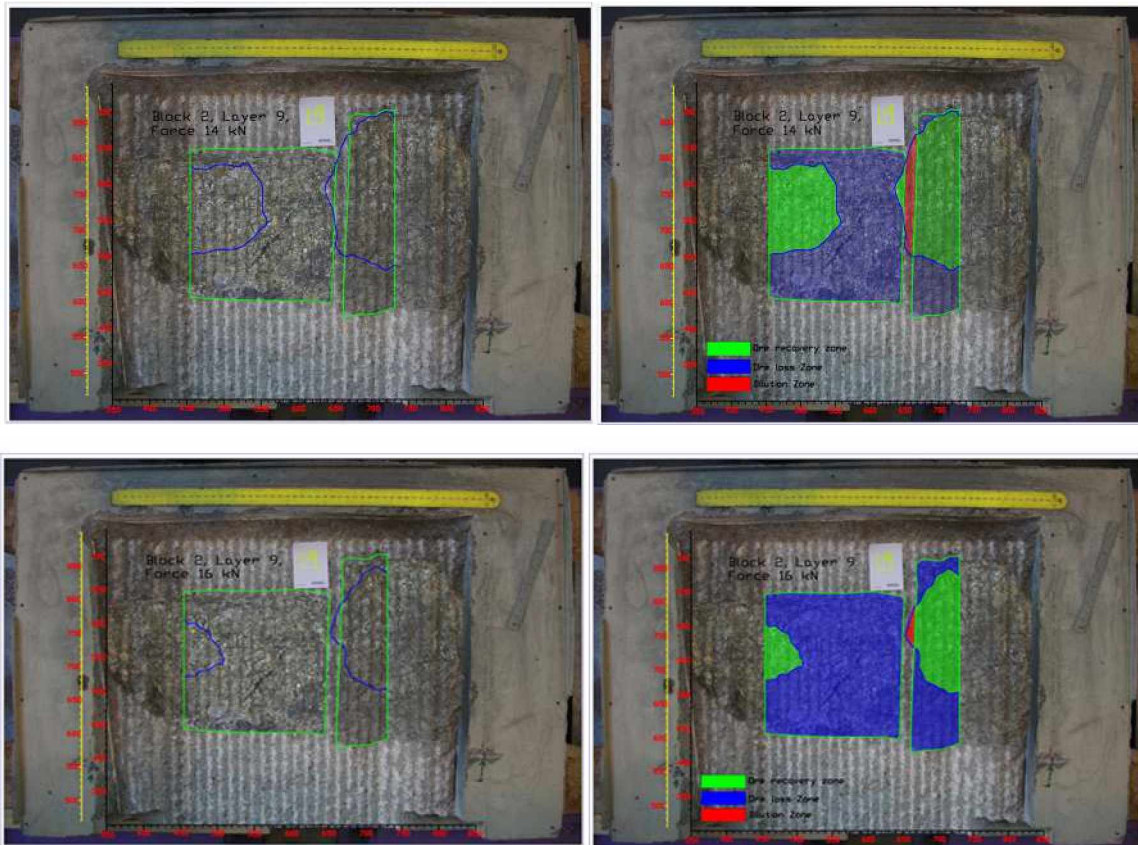


Figure 4-7: Overlaid method, Block 2 layer 9 with extracted-normal-force lines 14 kN (above) and 16 kN (under)

In Figure 4-7 shows three difference zones (see in chapter 3.1.2, page 35 ff) to identify the accuracy of the boundary, they are ore-recovery zone, ore-loss zone and dilution zone. These three zones will be affected to the accuracy of the boundary. For instance, it can be seen from Figure 4-7, the comparison of three zones between normal force 14 kN and 16 kN. It is shown that the three zones are automatically developed, as normal force line was changed. For example, normal force 14 kN was applied as a boundary between concrete and ore and it generated an extensive area of the ore-recovery zone compared with force line 16 kN. On

the other side, when the force value was set in a lower value, ore-recovery zone was increased, but sometimes a dilution zone was (red area). Therefore, these three zones are practical to determine a minimum value of force as a boundary limit.

Block 1

From the results, different minimum normal forces were obtained to apply as a boundary (see in Table 4-1 and Table 4-2). As discussed about determination of limit boundary (see in chapter 3.1.2, page 35 ff), block 1 layer 6 (see in Table 4-1) is shown ore recovery and dilution percentages in different cutting force values. This information can be used as a consideration to choose a boundary limit for separating the materials. In addition, consideration of adjustment depends on the situation (technical and non-technical).

Table 4-1: Ore recovery in consideration of the force value, Layer 6

Forces	Block 1 Layer 6 (Depth of cut, 4 mm)			
	Vein 1		Vein 2	
	Ore recovery (%)	Dilution (%)	Ore recovery (%)	Dilution (%)
6 kN	80.98	9.32	72.85	6.83
8 kN	70.28	1.72	74.92	0
10 kN	59.39	0	0	0
12 kN	47.81	0	0	0
14kN	17.66	0	0	0
16 kN	0	0	0	0
18 kN	0	0	0	0

Table 4-2: Ore recovery in consideration of the force value, Layer 8

Forces	Block 1 Layer 8 (Depth of cut, 6 mm)			
	Vein 1		Vein 2	
	Ore recovery	Dilution	Ore recovery	Dilution
7 kN	98.18	10.31	89.87	17.56
8 kN	94.44	5.60	77.99	14.60
10 kN	79.35	3.56	22.78	0
12 kN	68.04	3.27	0	0
14kN	58.21	1.87	0	0
16 kN	44.36	0	0	0
18 kN	28.50	0	0	0
20 kN	9.12	0	0	0

With regard to the cutting depth influences, it is shown significant results of range value of ore-recovery zone. the sample with cutting depth 4 mm showed the range of ore recovery between 44% - 84%. This result is represented wide range of the accuracy. A possible explanation for this might be that the cutting depth was quite narrow and therefore the cutting tool was inaccurately operated. On the other side, range for cutting depth 6 mm showed in the range 72%-98%. The range showed a greater result with respect to the previous outcome. In comparison of the results, it was assumed that the cutting depth might be also influence for obtaining the accuracy of the model. This distinction reveals the need for further investigation to apply greater cutting depth. The table of results of the ore recovery are presented Annex I.

Block 2

In the same way, block 2 is also shown the significant results in consideration of increasing the cutting depth. With regards to results (Table 4-3 and Table 4-4), Depth of cut 8 mm is shown a greater number of ore recovery zone, most of them are above 92%. On the other hand, layer with spacing 6 mm is shown range of the ore recovery in the range 85% - 93%, this number is lower compared with spacing 8 mm.

With regards to the previous result, the results of this study confirm that the cutting depth has influence in consideration of boundary determination. It is proven that cutting depth 8 mm has a significant result compared to the layer with cutting depth 6 mm.

Table 4-3: Ore recovery in consideration of the force value, Block 2 Layer 1

Forces	Block 2 Layer 1 (Depth of cut, 6 mm)			
	Vein 1		Vein 2	
	Ore recovery (%)	Dilution (%)	Ore recovery (%)	Dilution (%)
8 kN	85.07	5.77	97.92	59.16
10 kN	58.17	0.94	87.71	10.55
12 kN	20.45	0	78.47	3.15
14 kN	2.47	0	63.51	0
16 kN	0	0	46.10	0
18 kN	0	0	25.45	0
20 kN	0	0	4.95	0

Table 4-4: Ore recovery in consideration of the force value, Block 2 Layer 6

Forces	Block 2 Layer 6 (Depth of cut, 8 mm)			
	Vein 1		Vein 2	
	Ore recovery (%)	Dilution (%)	Ore recovery (%)	Dilution (%)
10 kN	93.79	11.11	99.13	0.86
12 kN	79.35	2.30	92.49	0.00
14 kN	51.14	0	79.96	3.77
16 kN	0	0	43.09	0
18 kN	0	0	0	0
20 kN	0	0	0	0

4.2 Element Presence

The following part moves on to describe results and analysis of the element presence influence towards the cutting resistance of the rock. Investigation between cutting resistance and element distribution was implemented to identify its correlation.

4.2.1 Element presence analysis

This section has attempted to provide elements distribution of the rock. As discussed about the geology of the rock (see in chapter 2.2, page 24 ff.), the samples are indicated containing Quartz (SiO_2), Arsenopyrite (FeAsS), Pyrite (FeS_2), Galena (PbS), Sphalerite (Zn,FeS) and Chalcopyrite (CuFeS_2). This information may useful as a basic knowledge to identify the single element affected the cutting resistance.

In this study, some definitions of veins are proposed in previous part (see in chapter 4.1, page 42 ff). Despite two zones, A-zone also was used to describe as an additional zone. It can be seen Figure 4-8.

To examine the influence of the elements, seven elements was chosen to identify the cutting resistance. They are calcium, iron, silicon, lead, sulfur, copper and zinc. The decision was made because of the initial assumption that the rock contains abundant of those elements which might have influences towards the cutting resistance. Furthermore, to obtain the quality of the measurement, one layer in every different cutting depth was examined to represent the measurement. As the experiment are applied four different cutting depths, thus four layers was chosen to investigate the element distribution within the rock.

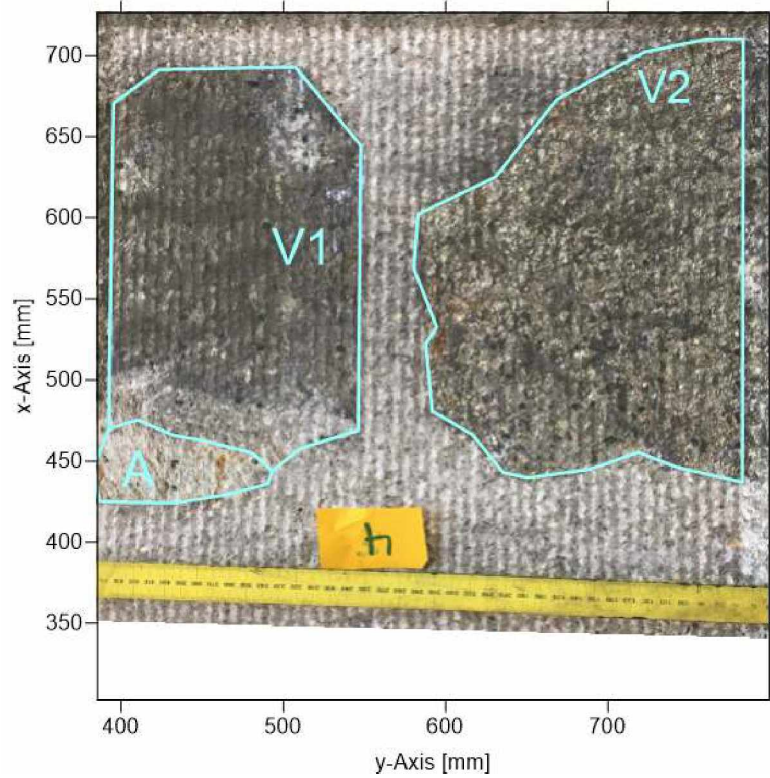


Figure 4-8: Sample Measurement (Block 1, Layer 4)

In addition, Figure 4-9 is shown the element distribution to identify the distribution in comparison of the normal force map. This figure might be useful for determining the element influences.

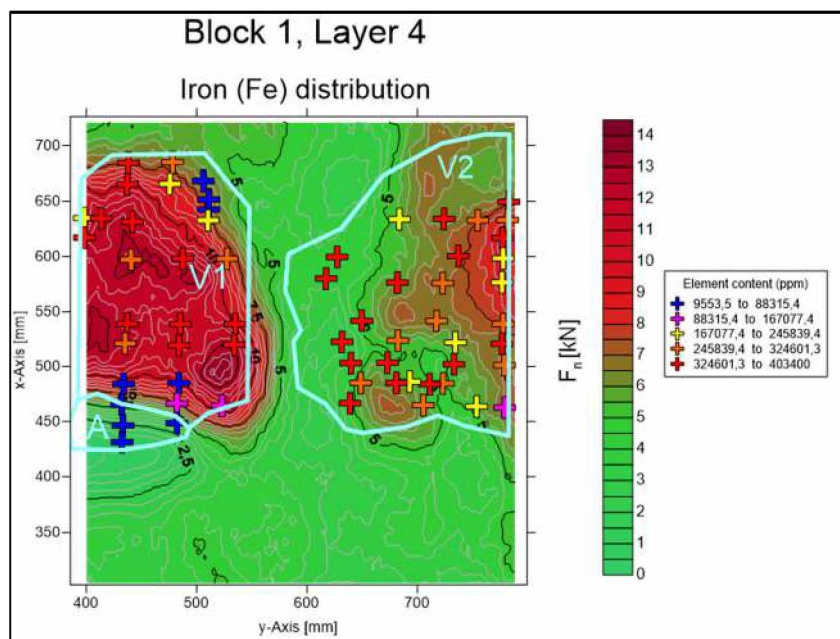


Figure 4-9: Element distribution (iron distribution) in comparison normal force

It is shown the quantity of the element in each point of measurement and the normal force value. Scale of the normal force is shown in the different colors. It was presented from light green into dark red color with respect to indicate the lower into high force respectively.

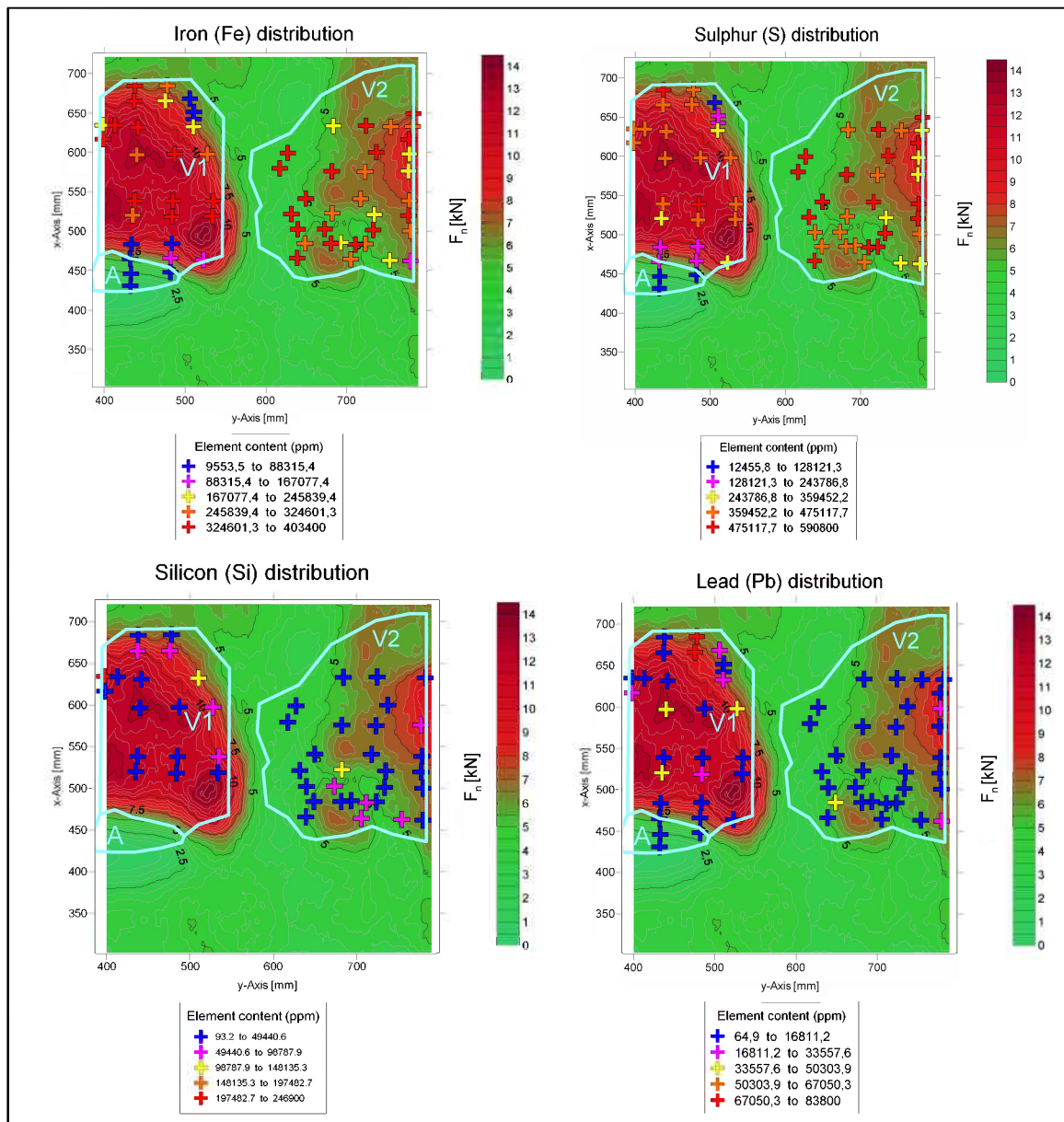


Figure 4-10: Element distribution (Iron, sulfur, Silicon and Lead) in block 1 layer 4

Before proceeding to examine the correlation, it is important to show all the element distributions to identify its deployment. A previously chapter stated that seven elements were evaluated to identify its presence toward the cutting resistance. In Figure 4-10 showed some samples of element distribution included the element's deployment of block 1 layer 4. These

analytical procedures and the results obtained from them are described in the next section. The results for all distribution maps are shown in Annex G.

4.2.2 Correlation element presence and cutting resistance

This section describes the evaluation of the current investigation related to element presence. According to the previous section, it showed some elements have significant distribution in the rock in comparison of the normal force, this information will be useful to identify the mineral presence by involving the cutting resistance information.

BLOCK 1

In block 1, two layers were chosen for further investigation of the element presence, they were layer 4 and layer 10. Turning now to the experimental evidence on layer 4, the result showed that vein 1 has higher normal force compared Vein 2. Additionally, it was also found an additional zone in vein 1, known as A-zone. This zone showed a lower normal force (see in Figure 4-10). This result might be happened because of some reasons, it can cause of the mineral condition or geological setting of the rock. In this case, A-zone is occurred because of mineral alteration. This can be seen form the physical condition of the rock which is easily destroyed, even by hand. Therefore, the normal force in A-zone is low.

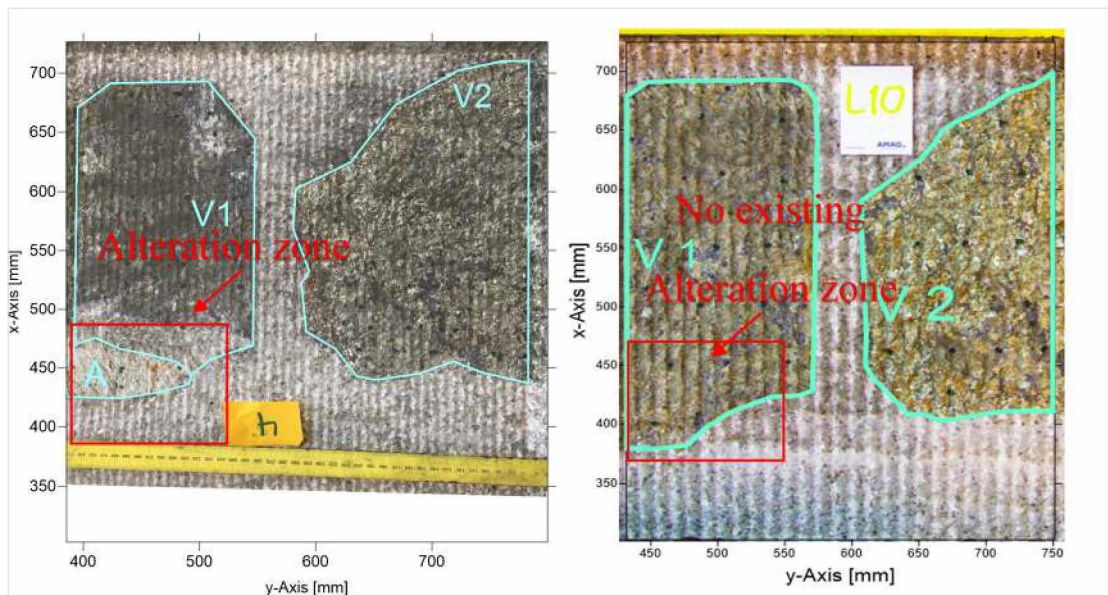


Figure 4-11: alteration zone in layer 4 (left) and layer 10 (right)

Furthermore, with regards to the element contain of A-zone, silicon was found in a high quantity (see in Figure 4-12) and it was altered (see in Figure 4-11). As a characteristics

silicon alteration is commonly very texture and destructive and there are major difficulties in recognizing the original rock [44]. This assumption is suited with actual condition related to the lower normal force. Following the next subsequent (see in Figure 4-11), the altered zone was gradually decreased and that was not found silicon presence in layer 10. Consequently, the normal force is increased again and the A-zone was not existing (see in Figure 4-12).

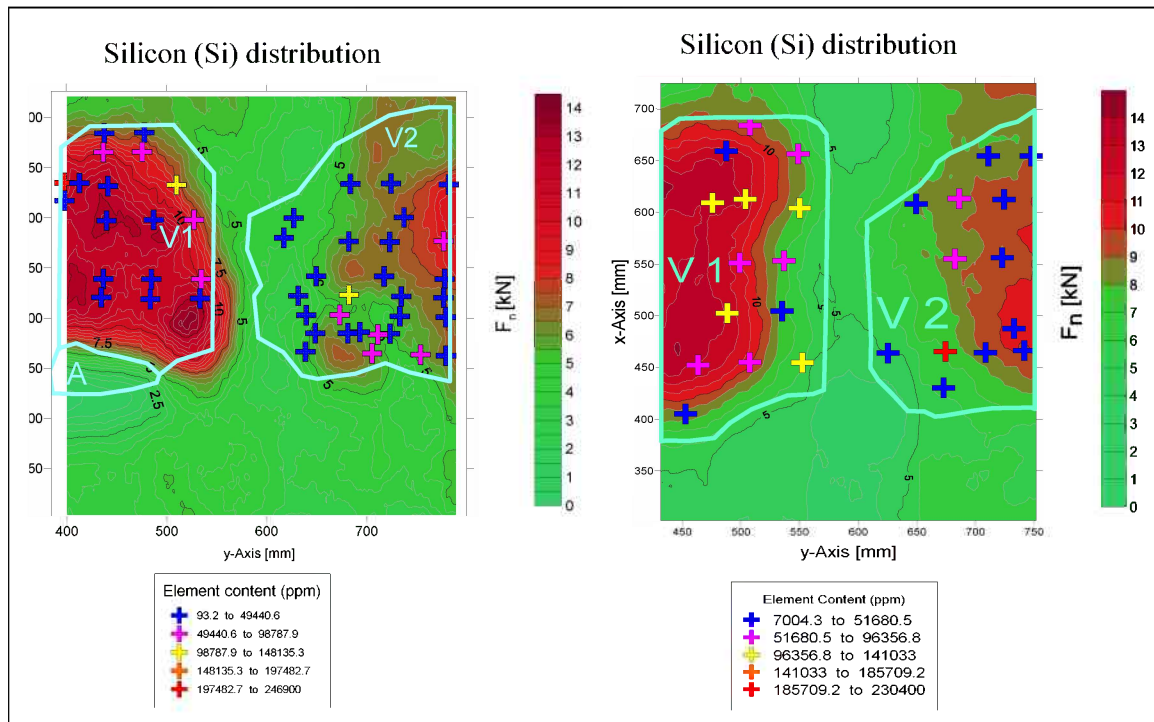


Figure 4-12: Silicon distribution with alteration zone, layer 4 (left) and no existing alteration zone, layer 10 (right)

Another significant element presence in layer 4 is iron (Fe) content. They were evenly distributed in both veins. In contrast to silicon presence, its presence was not influenced to the cutting resistance on the rock. It is shown that the normal force vein 1 is higher than vein 2, even they have same iron distribution content. After having personal discussed with Max Hesse, Bruno Grafe and Maria Ussath (22nd of Augustus 2017), this can be happened because several reasons:

- Grain of the rock can be influenced to the cutting resistance. In vein 2 showed a less solid interlocking grain and thus coarse-grained material of vein 2 is distinguishable entities. Consequently, the normal force vein 2 was lower than vein 1 (see in Figure

4-13). Different properties of vein 2, fine-grained and denser material was found in vein 1.

- Different mineral composition of iron (pyrite or chalcopyrite) might be caused a difference result.
- Mineral phases of the rock were randomly mixed and that is make the rock have different properties in consideration of the hardness.

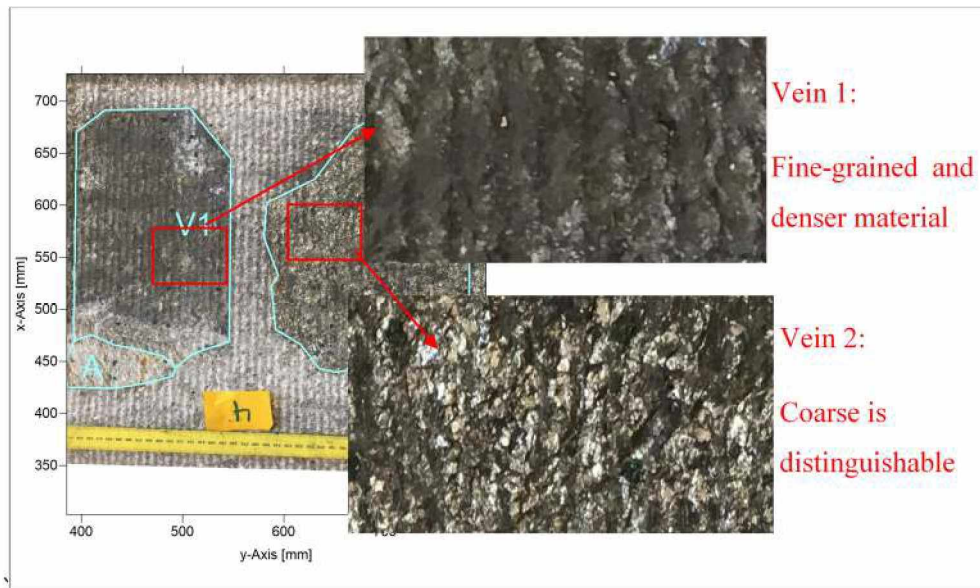


Figure 4-13: surface condition in layer 4 block 1

In the same way, sulfur contents are also distributed in high quantity and its presence were not shown strong influence to the cutting resistance (see in Figure 4-10). It can be seen that the normal force vein 1 and vein 2 is shown different values despite the sulfur distribution was evenly distributed in both veins. Thus far, the thesis has argued that both veins contain different mineral composition of sulfur. As mentioned in previous chapter about the mineralogy of the rock (see in chapter 3.2.3, page 40 ff).

However, in the calcium distribution, it is found different trend of distribution in comparison to normal force (see in Figure 4-14). They are shown strong correlation between quantity and the force value, it can be seen that layer 4 and layer 10 have high force with respect to calcium distribution. This finding is assumed that calcium generated high normal forces. Because of this, further analysis is necessary to evaluate the consistency of the result.

Turning now to describe the rest element contents in block 1, like lead, sulfur, copper and zinc. These elements were not shown in high quantity, it is only detected in some spots and

thus to identify the correlation between forces and the element presence needs further examination in consideration mineral composition, instead of element identification.

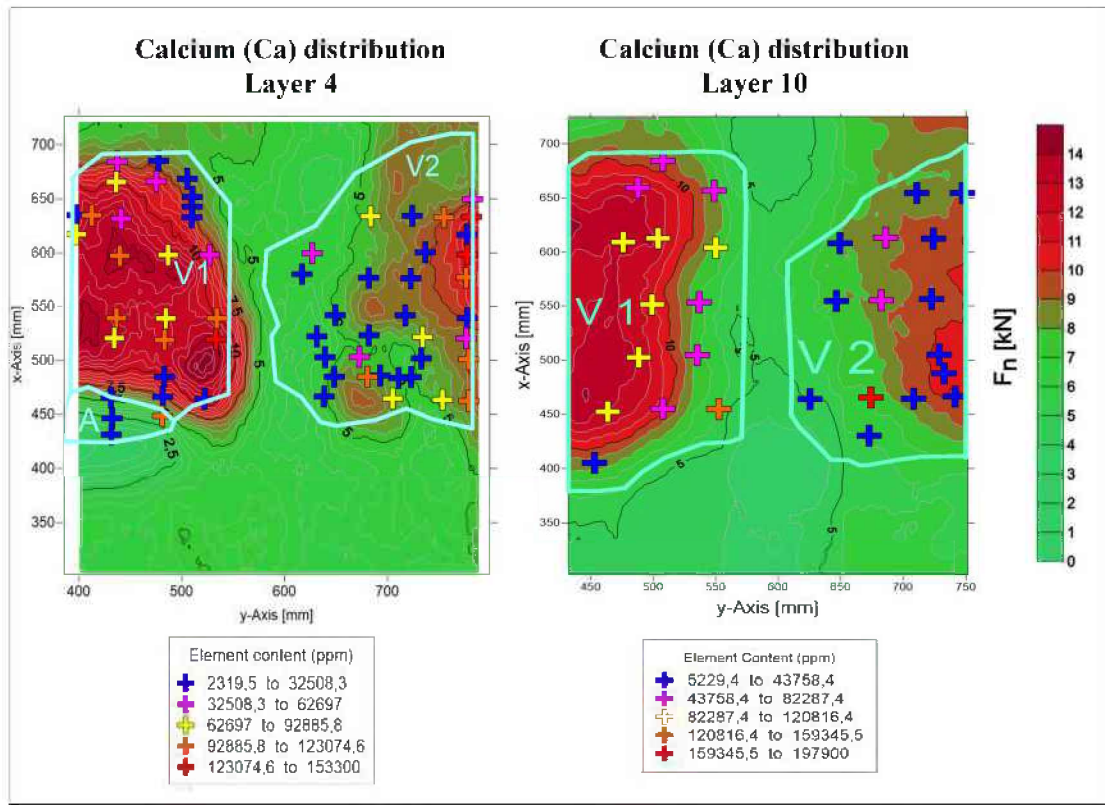


Figure 4-14: Ca distribution in layer 4 (left) and layer 10 (right)

BLOCK 2

Moving on now to consider the element contains in block 2, the observed elements are the same with block 1. They are silicon, calcium, iron, lead, sulfur, copper and zinc.

As mentioned in previous section that iron and sulfur was not shown strong consistency with respect to cutting resistance. The result for these two elements are shown same behavior, the quantity of these elements was not shown a good correlation (see in Figure 4-15).

Turning now to the calcium distribution, initial observation suggests that there may be a link between calcium and cutting resistance. With regard to the result of block 2, the argue was declined because the result is contradicted with the initial observation. It can be seen that layer 3 (vein 1) has low normal force in spite of having more calcium quantities. Therefore, the calcium presence was not appropriately used as an indicator to predict the cutting resistance.

Due to the lack of silicon, thus block 2 was not shown distinguish zone like block 1. In addition, the behavior of the rest element repeats the behavior of rest elements in block 1.

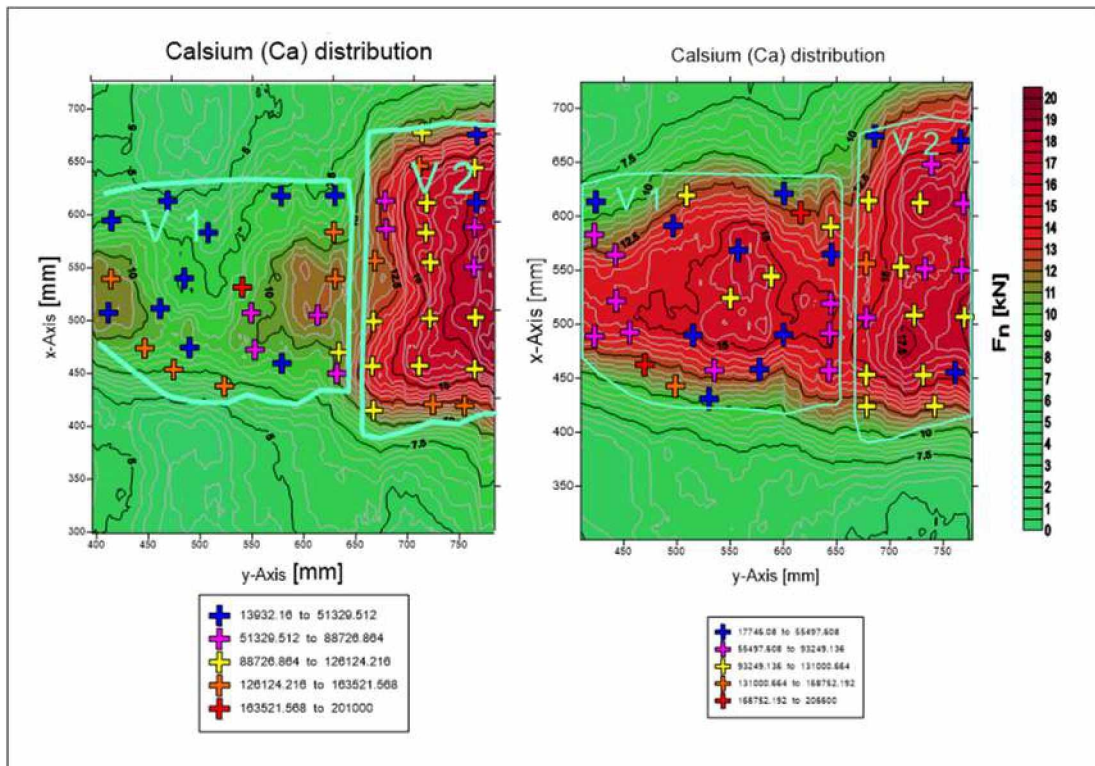


Figure 4-15: Calcium distribution block 2 layer 3 (left) and layer 6 (right)

As regards the results, a summary of the main findings the correlation between element presence and cutting resistance was not showed a strong correlation. As it might be happened that the element can form in different mineral composition and mineral phases, thus investigation of cutting force with respect to element presence was not suited with hXRF or efforts are necessary to develop a new method to apply hXRF with additional mineral examination to identify mineral contains within the rock.

Chapter 5 Conclusion and Outlook

This thesis has a basic idea to switch conventional method drill-and-blast into mechanical excavation. Even more, increasing the quality of materials are also another aim by reducing the dilution of excavated-materials. An appropriate method for this application is selective mining technique. In this case, utilization of cutting force are used as a parameter to determine the mineral boundaries. Once, this technique is successfully applied, the dilution of the material will decrease gradually and the system can be applied as a continue system as well.

This work shows an approach to examine the influence of cutting forces in consideration of mineral identification. In this case, the moving average method was implemented for creating force maps to identify mineralization boundaries. The three components of the cutting forces F_C , F_S and F_N where evaluated. As a result, F_N showed the best potential utilization different rock types. Nevertheless, while determining the mineral boundary of the rock, a correlation was found between rock and concrete. The finding of this study found that the correlation showed a significant result when the cutting depth was increased to identify the boundary between rock and concrete. It can be seen from the results that cutting depth 8 mm has a higher accuracy more than 82.9%, while the cutting depth 6 mm showed range of the accuracy above 50% - 93% and for cutting depth 4 mm showed small influence to determine the boundary, it is around 44% - 84%.

Furthermore, this study included analysis of influence element contents towards the cutting resistance. The study shows that the correlation between element presence and cutting resistance was not found a strong relation. As one element are possibly compounded in different kind of minerals and thus one element could be generated different cutting force maps. For example, iron can presence as a pyrite or chalcopyrite in the rock and therefore distribution of iron generates different cutting resistance. In addition, these two minerals have different characteristic in the nature. Because of this finding, efforts are necessary to develop a new method to apply hXRF with additional mineral examination to identify mineral contains within the rock. The further investigation to be carried out are suggested.

Future Work

To obtain good results for the next experiment, some procedures and methods should be added or developed to achieve results that are more reliable. For reliable results, some suggestions are required as follows:

- Modify design of cutting area, especially for the length of cutting should be decreased every layer.
- Test different kinds of ore types to generalize results.
- Test same parameters of rock to define the consistency of the results
- Apply methods to simplify and automate the researched workflow.
- Research the influence of steadily wearing picks to the applicability of the mentioned method.
- And as a future step, consider an in-situ prototype assembly, possibly utilizing strain gauges instead of piezo sensors because of the price difference.

Bibliography

- [1] N. Bilgin, H. Copur and C. Balci, Mechanical Excavation in Mining and Civil Industries, Florida: CRC Press, 2013.
- [2] H. Huber, "Sensor technology for intelligent mining roadheaders," Fraunhofer IML, Munich, 2010.
- [3] H. L. Hartman and J. M. Mutmansky, Introductory Mining Engineering, New Jersey: John Willey & Sons, Inc., 2002.
- [4] A. Ramezanzadeh and M. Hood, "A state-of-the-art review of mechanical rock excavation technologies," International Journal of Mining and Enviromental Issues, vol. 1, pp. 29-39, 2010.
- [5] P. N. W. Verhoef, Wear of Rock Cutting Tools, Rotterdam: A.A. Balkema, 1997.
- [6] J. Hudson and J. Harrison, "Engineering Rock Mechanics," in An Introduction to the Principles, Elsevier Science, 2000.
- [7] B. Grafe, "Potential des Hinterschneidens mit Rundschafftmeißeln zur Steigerung der Schneideffizienz," TU-Freiberg, Freiberg, 2014.
- [8] A. Malovyk, "Investigating the reduction od cutting resistance of granite speciment induced by microwave irradiation with varying irradiation times," TU Bergakademie Freiberg, Freiberg, 2017.
- [9] E. Hoek and E. T. Brown, "Practical estimates of rock mass strength," International Journal Rock Mechanic and Mining Science , vol. 34, no. 1997, pp. 1165-1186, 1997.
- [10] H. Käsling and K. Thuro, "Determining rock abrasivity in the laboratory," Munich, 2010.
- [11] J. A. Hudson and J. P. Harrison, Engineering rock mechanics, London: Pergamon, 1997.

Bibliography

- [12] N. Bilgin, C. Baclci, H. Copur and H. Tucedemir, "Dominant rock properties affecting the performance of conical picks and the comparasion of some experimental and theoretical results," *Rock Mechanics and mining Sciences*, vol. 43, 2006.
- [13] E. T. Brown, C. Fairhurst and E. Hoek, *Comprehensive rock engineering*, London: Pergamon press.
- [14] R. Göktan, "Effect of cutter pick rake angle on the failure pattern of high-strength rocks," *Mining Science and Technology*, vol. 11, no. 1990, pp. 281-285, 1990.
- [15] R. J. Fowell, O. Z. HEKİMOĞLU and S. Altinoluk, "Drag tools employed on shearer drums and roadheaders," *Reseacrhgate*, 2016.
- [16] A. W. Khair, "Research and Innovations for Continuous Miner's Cutting Head, for Efficient Cutting Process of Rock/Coal," *International Mining Congress and Exhibition of Turkey*, vol. 17, no. 2001, pp. 45-55, 2001.
- [17] H. Copur, L. Ozdemir and J. Rostami, "Roadheader applications in mining and tunneling industries," [Online].
- [18] I. GLobalSpec, "Roadheader Infromation," *GlobalSpec*, [Online]. Available: http://www.globalspec.com/learnmore/specialized_industrial_products/mining_equipment/roadheaders. [Accessed June 2017].
- [19] H. S, "Criteria for Selecting a Boom-Type Roadheader," *Mining Magazine. The Mining Journal, Ltd*, no. 1998, p. 183, 1988.
- [20] P. Darling, *SME Mining Engineering Handbook*, United States of America: Society for mining, Metallurgy, and exploration, Inc., 2011.
- [21] WHAYNE, "Wahyne.com," [Online]. Available: <https://whayne.com/new-equipment/machines/continuous-miners/>. [Accessed July 2017].

Bibliography

- [22] Caterpillar, "Caterpillar," [Online]. Available: http://www.cat.com/en_US/products/new/equipment/underground-longwall/shearers/18346615.html#. [Accessed July 2017].
- [23] J. L. W. S and J. Huo, "Study of TBM Cutterhead Fatigue Crack Propagation Life Based on Multi-Degree of Freedom Coupling System Dynamics," Reseacr gate, Dalian, 2015.
- [24] W. Sun, J. Ling, J. Huo, L. Guo and X. Song, "Study of TBM Cutterhead Fatigue Damage Mechanisms Based on a Segmented Comprehensive Failure Criterion," Engineering Failure Analysis, vol. 58, no. 2015, pp. 64-82, 2015.
- [25] WERMAC, "Wermac.org," [Online]. Available: http://www.wermac.org/civil_eng/eurotunnel.html. [Accessed June 2017].
- [26] M. Z. Naghadehi and R. Mikaeil, "Optimization of Tunnel Boring Machine (TBM) Disc Cutter Spacing in Jointed Hard Rock Using a Distinct Element Numerical Simulation," Periodica Polytechnica Civil Engineering, pp. 56-65, 03 07 2016.
- [27] J. Fuentes-Cantillana, J. Catalina, A. Rodriguez, J. Orteu and D. Dumahu, "Use of Computer vision for Automation of a Roadheader in Selective Cutting Operation," International Symposium on Mine Mechanization and Automation, vol. Golden, no. HAL, pp. 15.1 - 15.10, 1991.
- [28] R. Galler, T. Stoxreiter and R. Wenighofer, Writers, Disc cutter load monitoring and face monitoring in TBM-tunnelling - developments for detailed analysis of the cutting process. [Performance]. Montanuniversität Leoben, 2016.
- [29] A. Copco, "Atlascopco.com," Atlas Copco UK Holdings Ltd, 2017. [Online]. Available: https://www.atlascopco.com/en-uk/mrba/customer-stories/stories---ads/Enabling_automation. [Accessed May 2016].
- [30] Analyticon, "Anwendungen - Portable RF-Analysatoren," Freiberg.
- [31] U. Sebastian, Die Geologie des Erzgebirges, Berlin: Springer Spektrum, 2013.

Bibliography

- [32] L. Baumann, E. Kuschka and T. Seifert, Lagerstaetten des Erzgebirges, 2000.
- [33] S. F. GmbH, "Silber bergwerk Freiberg," Saxonia Freiberg GmbH, [Online]. Available: <http://www.besucherbergwerk-freiberg.de/fuehrungen/#erlebnistour>. [Accessed June].
- [34] R. J. H, "Moving Average," june 2009. [Online]. Available: www.robjhyndman.com. [Accessed June 2017].
- [35] G. Borradaile, Statistics of earth science data, Thunder Bay, Canada: Springer, 2003.
- [36] Surfer, Surfer Guidelines, Colorado: Golden Software, Inc. .
- [37] M. E. Rossi and C. V. Deutsch, Mineral Resource Estimation, Dordrecht: Springer , 2014.
- [38] Mineral.net, "Minerals.net," 2017. [Online]. Available: www.minerals.net/mineral/sphalerite.aspx. [Accessed June].
- [39] M. Grimmer and Z. Haque, "Development of a method for element content determination in soil and minerals by means of hand-held X-ray fluorescence," Geoscience, Geo-engineering and Mining, TU Bergakademie Freiberg, Freiberg, 2014.
- [40] M. Ussath and M. Grimmer, "Application and Recalibration of A Handheld X-Ray Fluorescence (HXRF) Device.," TU Bergakademie Freiberg, Freiberg, 2017.
- [41] M. Ussath, N. Hoth, M. Grimmer and A. Alcalde, "Hand-held X-ray fluorescence (hXRF) measurements as a useful tool in the environmental and mining sector - Comparative measurements and effects of water content.," TU Bergakademie Freiberg, Freiberg, 2017.
- [42] R. Taylor, Ore textures: Recognition and Interpretation, Queensland: Springer, 2010.
- [43] F. R. J, H. O. Z and A. S, "www.maden.org.tr," [Online]. [Accessed 10 6 2017].

Bibliography

- [44] A.W.Khair, "Research and Innovations for continuous Miner's Cutting Head, for Efficient Cutting Process of Rock/Coal," International Mining Congress and Exhibition of Turkey, vol. 17, no. 2001, 2001.
- [45] H. W, Writer, Basics in Geostatistics 2 Geostatistical interpolation/estimation: Kriging methods. [Performance]. MINES ParisTech , 2013.
- [46] ASW-GmbH, Technische Dokumentation zur Sonderhobelmaschine fuer Gesteinproben, Naumburg: ASW-GmbH, 2007.
- [47] M. Vorona and W. G. a. C. Drebenstedt, Scientific Reports on Resource Issues, Freiberg, Germany: Medienzentrum der TU Bergakademie Freiberg, 2010.
- [48] O. Leuangthong, C. Nuefeld and C. Deutsch, "Optimal Selection of Selection Mining (SMU) Size," Alberta.
- [49] Y. Sun and X. S. Li, "Influence of Cutting Interactions on Cutting Force of a Pick," Conference on Modeling, Identification and Control, vol. 3, no. AASRI Procedia, pp. 692-699, 2012.
- [50] T. simonite, "MIT Technology Review," 28 December 2016. [Online]. Available: www.technologyreview.com. [Accessed June 2017].
- [51] Q. Cheng, "Interpolation by Kriging, Moving Averaging and Multifractal Modeling," Toront.
- [52] P. Caughill, "Futurism," Futurism, 6 January 2017. [Online]. Available: https://futurism.com/?p=66160&post_type=post. [Accessed June 2017].
- [53] J. Parreira and J. Meech, "Autonomous vs manual haulage trucks - how mine simulation contributes to future haulage system developments," Vancouver, 2004.
- [54] J. Parreira, Writer, Automation in Mining Industry. [Performance]. University of British Columbia, 2008.

Bibliography

- [55] J. Rostami, L. Ozdemir, D. M. Neil and R. Gertsch, "Production Estimating Techniques for Underground Mining Using Roadheaders," Colorado.
- [56] M. Poirier, "Mining Group," The future of mining is automated, November 2015. [Online]. Available: <http://www.mining.com/web/the-future-of-mining-is-automated/>. [Accessed June 2017].
- [57] A. Lislerud, Principle of Mechanical Excavation, Helsinki: POSIVA OY, 1997.
- [58] W. Sun, J. Ling, J. Huo and X. Song, "Study of TBM Cutterhead Fatigue Crack Propagation Life Based on Multi-Degree of Freedom Coupling System Dynamics," ResearchGate, Dalian, 2015.
- [59] G. Bohling, "Kriging," Kansas Geological Survey, October 2005. [Online]. Available: <http://people.ke.edu/~gbohling/cpe940>. [Accessed May 2017].
- [60] E. Uhlmann and F. Kaulfersch, "Process behaviour of super-hard cutting materials for machining mineral cast," Procedia CIRP, vol. 48, no. 2016, p. 892 – 897, 2015.
- [61] B. S. Fisher and S. Schnittger, "Autonomous and Remote Operation Technologies in the Mining Industry: Benefits and costs," Kingston, 2012.
- [62] C. Balci, M. Demircin, H. Copur and H. Tuncdemir, "Estimation of optimum specific energy based on rock properties for assessment of roadheader performance," The Journal of The South African Institute of Mining and Metallurgy, no. 2004, pp. 633-642, 2004.
- [63] N. Bilgin, M. Demircin, H. Copur, C. Balci, H. Tuncdemir and N. Akcin, "Dominant rock properties affecting the performance of conical picks and the comparison of some experimental and theoretical results," International Journal of Rock Mechanics and Mining Sciences, vol. 43, no. 2005, pp. 139-156, 2005.
- [64] C. Deutsch and J. Deutsch, "Introduction to Choosing a Kriging Plan," Edmonton, 2015.

Bibliography

- [65] D. J. J. Walvoort, Writer, Exploring the World of Ordinary Kriging. [Performance]. Wageningen University and Research Center, 2004.
- [66] S. J. Anderson, R. J. Morrell and D. A. Larson, "A Laboratory Comparison of Drag Cutting Methods in Hard Rock," United States Department of The Interior, Minneapolis, 1987.
- [67] J. L. Williams and P. Hagan, "An assessment of the correlation between the strength and cuttability of rock," Coal operator's conference, pp. 186-192, 12 February 2014.
- [68] O. Instrument, "the-experts," Oxford Instrument, [Online]. Available: www.the-experts.com/x-ray-flourescence-xrf-explained. [Accessed June].
- [69] M. Inc, "Mektunnel.com," Mektunnel Inc., [Online]. Available: <http://www.mektunnel.com/product/new-bbm-roadheaders/>. [Accessed June 2017].
- [70] S. E. Kesler, "Mineral Supply and Demand into the 21st Century," USGS, 2007.
- [71] R. J. Fowell, O. Z. HEKİMOĞLU and S. Altinoluk, "Drag tools employed on sherarer drums and roadheaders," Researchgate, 2016.
- [72] M. Z.N and R. M, "Optimization of Tunnel Boring Machine (TBM) Disc Cutter Spacing in Jointed Hard Rock Using a Distinct Element Numerical Simulation," Periodica Polytechnica Civil Engineering, pp. 56-65, 03 07 2016.
- [73] H. Schneider, "Criteria for selecting a boom-type roadheader," Mining Magazine. The Mining Journal, Ltd, no. 1998, p. 183, 1988.
- [74] J. E. Friant, "Disc cutter technology applied to drill bits," Excavation Engineering Associates, Inc., Seattle, 1997.
- [75] L. B, E. K and T. S, Lagerstaetten des Erzgebirges, 2000.
- [76] R. J. Hyndman, "Moving Average," H, Rob J, 2009.

Bibliography

- [77] M. Ussath and M. Grimmer, "APPLICATION AND RECALIBRATION OF A HANDHELD X-RAY FLUORESCENCE (HXRF) DEVICE," Technische Universität Bergakademie Freiberg, Freiberg.

List of Figures

FIGURE 1-1: FAILURE MODE DURING CUTTING [5]	3
FIGURE 1-2: SCHEME OF CHIP FORMED IN CUTTING FORCE GRAPH [7]	3
FIGURE 1-3: PICK FORCE COMPONENTS [8]	4
FIGURE 1-4: RELIEVED CUTTING MODE (INTERACTION BETWEEN GROOVES) [12]	7
FIGURE 1-5: GENERAL EFFECT OF CUTTER SPACING ON SPECIFIC ENERGY [4]	8
FIGURE 1-6: CUTTING GEOMETRY OF POINT-ATTACK PICKS [8]	9
FIGURE 1-7: ROADHEADERS [18]	12
FIGURE 1-8: CONTINUOUS MINERS [21]	13
FIGURE 1-9: LONGWALL SHEARERS [22]	13
FIGURE 1-10: TBM CUTTER HEAD (LEFT) [24] AND BORING MACHINE (RIGHT) [25]	14
FIGURE 1-11: CONTROL SYSTEM STRUCTURE [27]	15
FIGURE 1-12: DISC CUTTER (LEFT) AND DISCS POSITION IN TBM (RIGHT) [28]	16
FIGURE 1-13: GEOLOGICAL MAPPING – SCHIEFERGNEISS (LEFT) AND RESULTS OF MEASURED NORMAL FORCE (RIGHT) [28]	17
FIGURE 1-14: AUTOMATED DRILLING (LEFT) AND CONTROLLING INTERFACE (RIGHT) [29] ..	18
FIGURE 2-1: CUTTING MACHINE HXS 1000-50 (LEFT) AND 3D MODEL (RIGHT) [7, 8]	19
FIGURE 2-2: FORCE COMPONENTS OF THE HSX-1000-50 [8]	20
FIGURE 2-3: DATA ACQUISITION CHANNEL (LEFT) AND DEWESOFT COMPUTER (RIGHT)	21
FIGURE 2-4: HAND-HELD X-RAY FLUORESCENCE ANALYZER, NITON XL3	21
FIGURE 2-5: SCHEME OF HXRF STRUCTURE AND FUNCTIONAL PRINCIPLE [31]	22
FIGURE 2-6: CONGRUENCY OF THE HXRF MEASURED (IRON) ON MILLED, CUP-FILLED ORE- SAMPLES AND CHEMICAL-ANALYTICAL VALUES FROM LABORATORY ANALYSIS [32, 33][PERSONAL INTERVIEW WITH M. USSATH, SCIENTIFIC ASSISTANT, TUBAF, FREIBERG 25.08.17]	23
FIGURE 2-7: ROCKS BEFORE PREPARATION	24
FIGURE 2-8: SAMPLE LOCATION, REICHE ZECH, FREIBERG, GERMANY [34] ,[RALF SCHLÜTER, REICHE ZECH STAFF]	25
FIGURE 2-9: VERTICAL PROFILE OF FREIBERG (ABOVE) AND MAP OF MAIN METAL RAW MATERIAL IN FREIBERG (UNDER) [36]	26
FIGURE 2-10: DIMENSION OF PREPARED BLOCK	27
FIGURE 2-11: REFERENCE POINT	28

List of Figures

FIGURE 2-12: SCHEME OF ADDITIONAL POINTS AS REFERENCES	29
FIGURE 2-13: MEASUREMENT POINTS.....	30
FIGURE 2-14: CUTTING LINES.....	31
FIGURE 3-1: FORCES ACTING ON THE CUTTING TOOL	33
FIGURE 3-2: GLOBAL MEAN ANNUAL TEMPERATURES, SMOOTHED BY MOVING AVERAGE [38]	34
FIGURE 3-3: SCHEME OF MINERAL ZONES.....	36
FIGURE 3-4: UNTRIMMED BLOCK (LEFT) AND TRIMMED BLOCK (RIGHT).....	37
FIGURE 4-1: SET OF FORCE MAPPING: AVERAGE CUTTING FORCE (A), SIDE FORCE (B) AND NORMAL FORCE (C) OF BLOCK 2 LAYER 1 WITH DEPTH OF CUT 6MM.....	42
FIGURE 4-2: BLOCK 2 LAYER 3	43
FIGURE 4-3: AVERAGE CUTTING FORCE (F_c) BLOCK 1 (LEFT) AND BLOCK 2 (RIGHT).....	44
FIGURE 4-4: CUTTING FORCE FORCE COMPARED WITH CUTTING DEPTH.....	44
FIGURE 4-5: AVERAGE SIDE FORCE COMPARED WITH CUTTING DEPTH.....	45
FIGURE 4-6: AVERAGE NORMAL FORCE COMPARED WITH CUTTING DEPTH.....	45
FIGURE 4-7: OVERLAID METHOD, BLOCK 2 LAYER 9 WITH EXTRACTED-NORMAL-FORCE LINES 14 kN (ABOVE) AND 16 kN (UNDER)	46
FIGURE 4-8: SAMPLE MEASUREMENT (BLOCK 1, LAYER 4)	50
FIGURE 4-9: ELEMENT DISTRIBUTION (IRON DISTRIBUTION) IN COMPARISON NORMAL FORCE	50
FIGURE 4-10: ELEMENT DISTRIBUTION (IRON, SULFUR, SILICON AND LEAD) IN BLOCK 1 LAYER 4.....	51
FIGURE 4-11: ALTERATION ZONE IN LAYER 4 (LEFT) AND LAYER 10 (RIGHT).....	52
FIGURE 4-12: SILICON DISTRIBUTION WITH ALTERATION ZONE, LAYER 4 (LEFT) AND NO EXISTING ALTERATION ZONE, LAYER 10 (RIGHT)	53
FIGURE 4-13: SURFACE CONDITION IN LAYER 4 BLOCK 1	54
FIGURE 4-14: CA DISTRIBUTION IN LAYER 4 (LEFT) AND LAYER 10 (RIGHT).....	55
FIGURE 4-15: CALCIUM DISTRIBUTION BLOCK 2 LAYER 3 (LEFT) AND LAYER 6 (RIGHT).....	56

List of Tables

TABLE 1-1: SIMPLE WAYS OF ESTIMATING UCS [9].....	5
TABLE 1-2: CLASSIFICATION THE CERCHAR-ABRASIVITY-INDEX [10].....	6
TABLE 1-3: WEAR EFFECT ON CONICAL CUTTING TOOL [7]	10
TABLE 2-1: OFFSET PICK AND LASER COORDINATES	28
TABLE 2-2: DEPTH OF CUT.....	31
TABLE 2-3: SPACING	32
TABLE 3-1: MOHS HARDNESS SCALE [41].....	39
TABLE 3-2: MINERAL PROPERTIES [42]	39
TABLE 4-1: ORE RECOVERY IN CONSIDERATION OF THE FORCE VALUE, LAYER 6	47
TABLE 4-2: ORE RECOVERY IN CONSIDERATION OF THE FORCE VALUE, LAYER 8	47
TABLE 4-3: ORE RECOVERY IN CONSIDERATION OF THE FORCE VALUE, BLOCK 2 LAYER 1 ..	48
TABLE 4-4: ORE RECOVERY IN CONSIDERATION OF THE FORCE VALUE, BLOCK 2 LAYER 6 ..	49

List of Abbreviations

UCS	Uniaxial compressive strength [<i>MPa</i>];
F_{\max}	Maximum force on the sample before failure [<i>N</i>];
σ_c	Uniaxial compressive strength [<i>MPa</i>]
A	Cross section area of the sample [mm^2]
σ_t	Brazilian tensile strength [<i>MPa</i>];
L	Length of the sample
D	Diameter of the sample [<i>mm</i>]
CAI	Cerchar Abrasivity Index;
TBM	Tunnel Boring Machine;
<i>c</i>	Unit correction factor;
RMR	Rock Mass Rating;
RQD	Rock Quality Designation;
θ	pick angle;
γ_a	attack angle;
γ_r	rotation angle;
β_c	clearance angle;
β_r	rake angle;
IML	Institute for Material Flow and Logistics;
3D	3 Dimension;
AITEMIN	Asociation Para La Investigacion Y Desarrollo de Los Recursos Naturales;
LAAS	Laboratory for Analysis and Architecture of System
CCD	charge-couple device;
RCS	Rig Control System;
F_C	cutting force [<i>kN</i>];
F_S	side force [<i>kN</i>];
F_N	normal force [<i>kN</i>];
hXRF	Hand-held X-Ray Fluorescence Analyzer;
kb-formation	Kiesieg-blendige Bleierz-formation;
eb-formation	Edle Braunspat-formation;

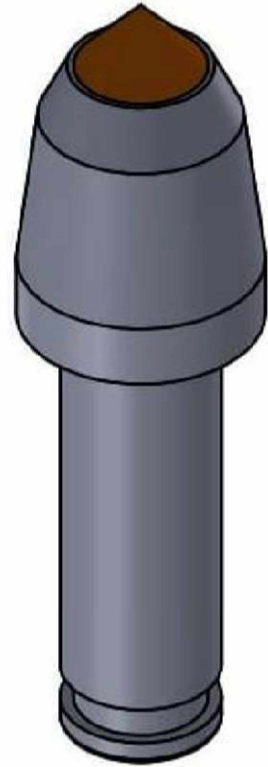
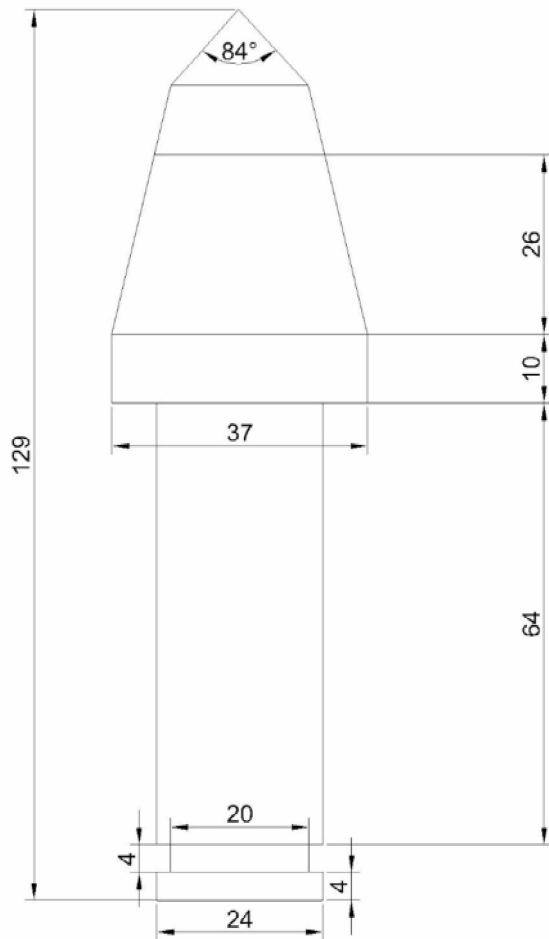
List of Abbreviations

fba-formation	Flourbarytische Bleierz-formation;
x_{mi}	average value;
$Z(u_i)$	data values;
$Z^*(u)$	estimate value;
λ_i	kriging weight;
m	constant mean;
V_1	Vein 1;
V_2	Vein 2;

Annex Table of Contents

Annex A.	Cutting tool dimension	i
Annex B.	Technical data performance of rig	ii
Annex C.	RMR classification system	iii
Annex D.	Freiberg Map	iv
Annex E.	Surface condition of the sample	v
Annex F.	Force mapping	vi
Annex G.	Element distribution maps	xviii
Annex H.	h-XRF Results	xxvi
Annex I.	Recalibration h-XRF	xxxv
Annex J.	Ore recovery	xxxvii
Annex K.	Technical data of concrete	xlii

Annex A. Cutting tool dimension



Annex B. Technical data performance of rig

Year of manufacture		2008
Nominal capacity [kW]		60 kW
Cutting speed	x-axis	1750 mm/s
	y-axis	7 mm/s
	z-axis	16 mm/s
Permissible force	x-axis	50 kN
	y-axis	30 kN
	z-axis	50 kN
Max. dimensions of a sample	x-axis	600 mm
	y-axis	1,000 mm
	z-axis	500 mm
Cutting depth (max)		50 mm
Acceleration (max)		10 m/s ²
Weight of the sample (max)		1,300 kg
Angle of attack		15° ... 90°
Angle of rotation		-90° ... 90°

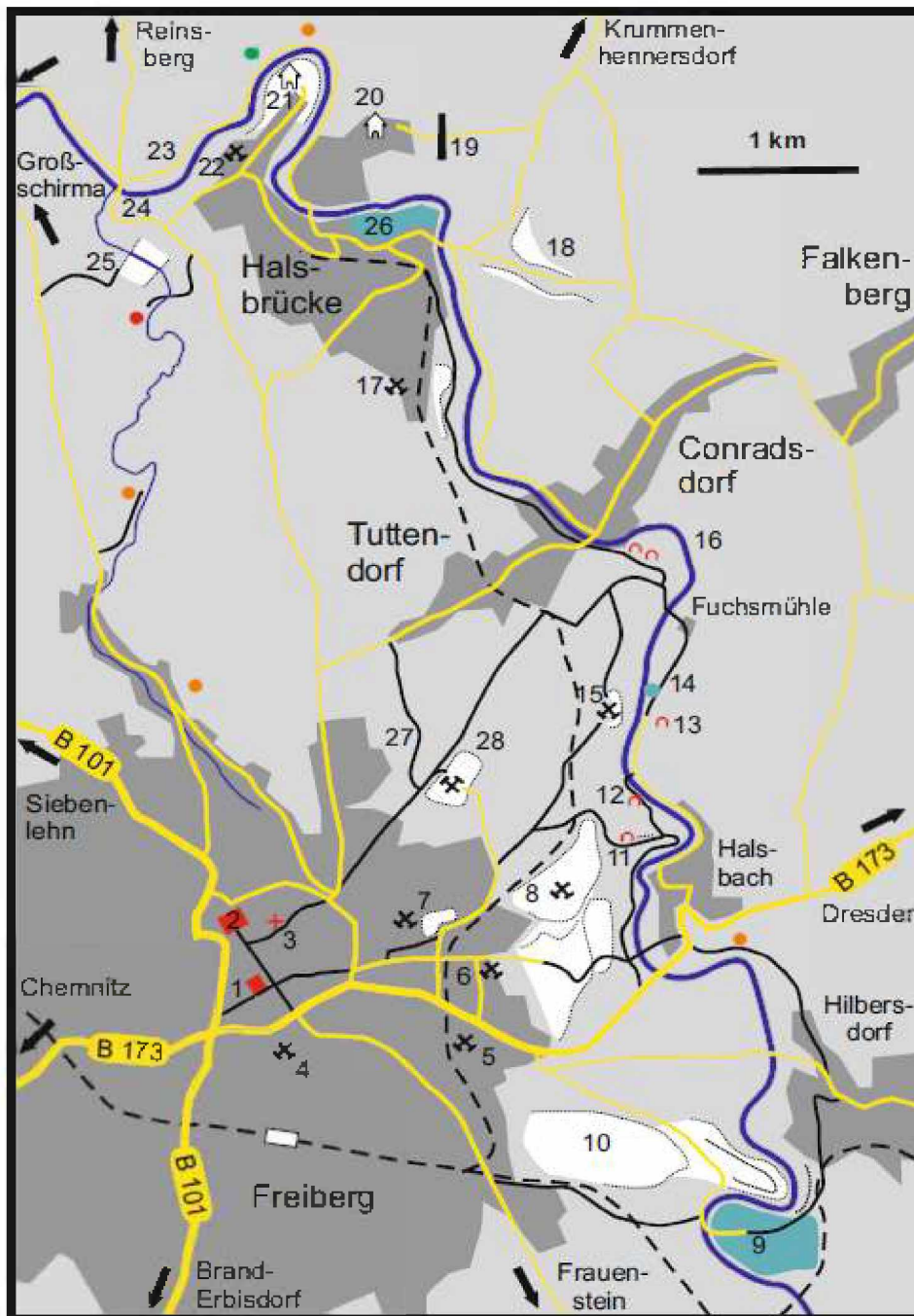
Annex C. RMR classification system

A. Classification Parameters and Their Ratings						
Parameter		Range of Values				
1 Strength of intact rock material	Point-load strength index	>10 MPa	4–10 MPa	2–4 MPa	1–2 MPa	For this low range, uniaxial compressive tests are preferred
	Uniaxial compressive strength	>250 MPa	100–250 MPa	50–100 MPa	25–50 MPa	5–25 MPa 1–5 MPa <1 MPa
Rating		15	12	7	4	2 1 0
2 Drill core quality RQD		90%–100%	75%–90%	50%–75%	25%–50%	<25%
	Rating	20	17	13	8	3
3 Spacing of discontinuities		>2 m	0.6–2 m	200–600 mm	60–200 mm	<60 mm
	Rating	20	15	10	8	5
4 Condition of discontinuities [see E]		Very rough surfaces; not continuous; no separation; unweathered wall rock	Slightly rough surfaces; separation <1 mm; slightly weathered walls	Slightly rough surfaces; separation <1 mm; highly weathered walls	Slickensided surfaces or gouge <5 mm, thick or separation 1–5 mm; continuous	Soft gouge >5 mm thick or separation >5 mm; continuous
	Rating	30	25	20	10	0
5 Groundwater	Inflow per 10-m tunnel length, L/min	None	<10	10–25	25–125	>125
	[joint water press]/[major principle σ]	0	<0.1	0.1–0.2	0.2–0.5	>0.5
	General conditions	Completely dry	Damp	Wet	Dripping	Flowing
Rating		15	10	7	4	0
B. Rating Adjustment for Discontinuity Orientations [See F]						
Strike and dip orientations		Very favorable	Favorable	Fair	Unfavorable	Very unfavorable
Ratings	Tunnels and mines	0	-2	-5	-10	-12
	Foundations	0	-2	-7	-15	-25
	Slopes	0	-5	-25	-50	-
C. Rock Mass Classes Determined from Total Ratings						
Rating		100 – 81	80 – 61	60 – 41	40 – 21	<21
Class number		I	II	III	IV	V
Description		Very good rock	Good rock	Fair rock	Poor rock	Very poor rock
D. Meaning of Rock Classes						
Class number		I	II	III	IV	V
Average stand-up time		20 years for 15-m span	1 year for 10-m span	1 week for 5-m span	10 hours for 2.5-m span	30 minutes for 1-m span
Cohesion of rock mass, kPa		>400	300–400	200–300	100–200	<100
Friction angle of rock mass, degrees		>45	35–45	25–35	15–25	<15
E. Guidelines for Classification of Discontinuity Conditions						
Discontinuity length (persistence)		<1 m	1–3 m	3–10 m	10–20 m	>20 m
Rating		6	4	2	1	0
Separation (aperture)		None	<0.1 mm	0.1–1.0 mm	1–5 mm	>5 mm
Rating		6	5	4	1	0
Roughness		Very rough	Rough	Slightly rough	Smooth	Slickensided
Rating		6	5	3	1	0
Infilling (gouge)		None	Hard filling <5 mm	Hard filling >5 mm	Soft filling <5 mm	Soft filling >5 mm
Rating		6	4	2	2	0
Weathering		Unweathered	Slightly weathered	Moderately weathered	Highly weathered	Decomposed
Rating		6	5	3	1	0
F. Effect of Discontinuity Strike and Dip Orientation in Tunneling						
Strike Perpendicular to Tunnel Axis			Strike Parallel to Tunnel Axis			
Drive with dip: Dip 45°–90°	Drive with dip: Dip 20°–45°		Dip 45°–90°		Dip 20°–45°	
Very favorable	Favorable		Very favorable		Fair	
Drive against dip: Dip 45°–90°	Drive against dip: Dip 20°–45°		Dip 0°–20°, irrespective of strike			
Fair	Unfavorable		Fair			

Source: Hoek et al. 1998.

* Some conditions are mutually exclusive. For example, if infilling is present, the roughness of the surface will be overshadowed by the influence of the gouge. In such cases, use A.4 directly.

Annex D. Freiberg Map



- | | | |
|------------------------|---|---------------------|
| 1 Freiburger Obermarkt | 11 Erzbahntunnel und Erzbahndamm | 21 7. Lichtloch |
| 2 Schloss Freudenstein | 12 Verträgliche Gesellschaft-Stolln | 22 Grube Beihilfe |
| 3 Dom | 13 Reicher Trost Stolln | 23 Kahnhebewerk |
| 4 Rote Grube | 14 Hilligersche Hütte | 24 Altväterbrücke |
| 5 Thurmhofschacht | 15 Ludwigschacht | 25 Spülhalde |
| 6 Abrahamschacht | 16 Alter und Tiefer Fürstenstolln und Umbruch | 26 Hütte Halsbrücke |
| 7 Grube Alte Elisabeth | 17 Oberes Neues Geschrei | 27 Herders Ruhe |
| 8 Davidschacht | 18 Lorenz Gegentrum | 28 Davidschacht |
| 9 Muldenhütten | 19 Halsbrücker Esse | |
| 10 Hütte Freiberg | 20 8. Lichtloch | |

Annex E. Surface condition of the sample

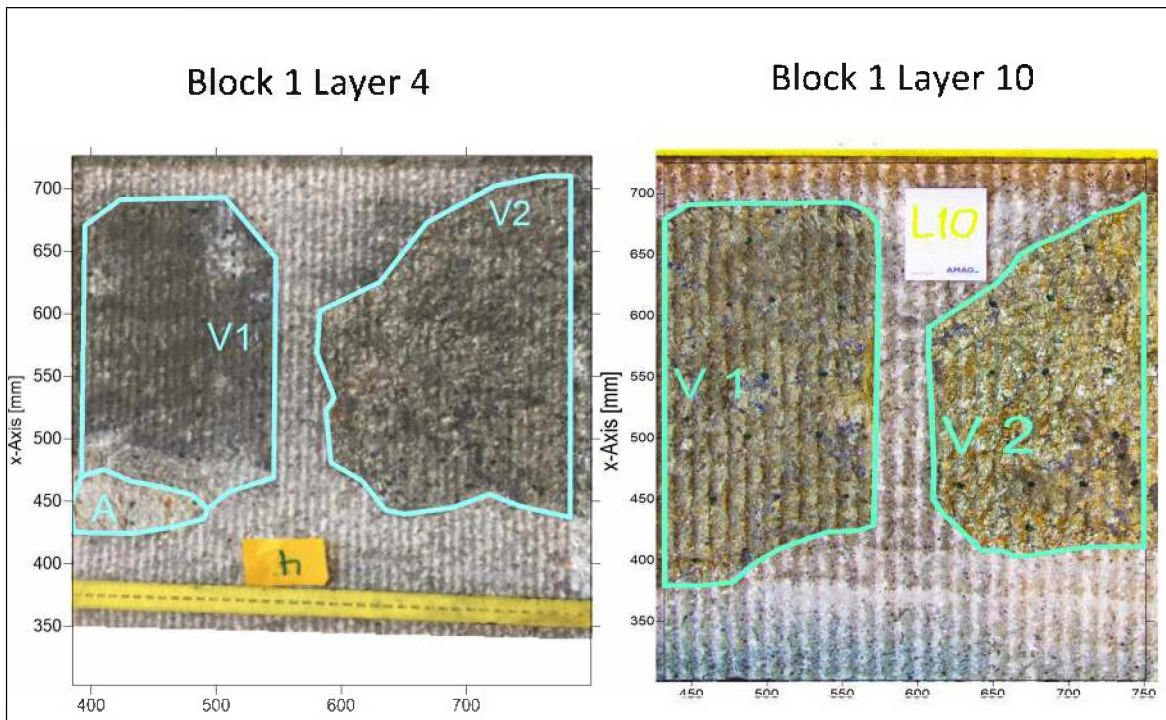


Figure Annex E-1: Surface condition block 1

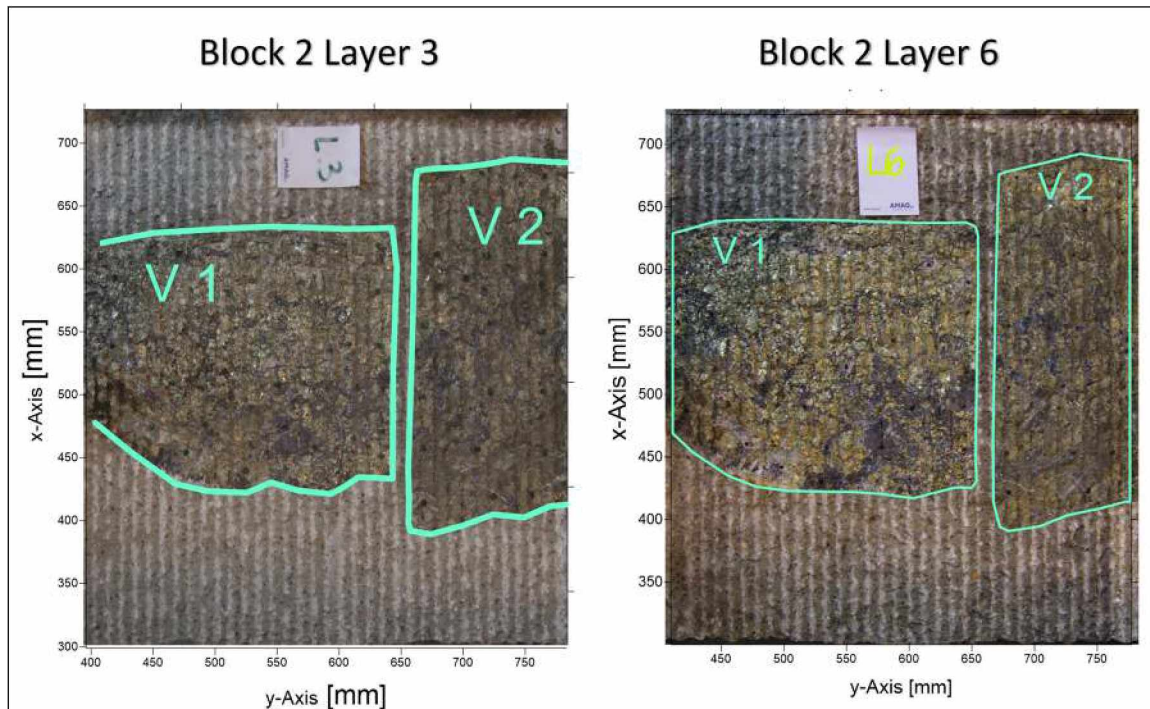


Figure Annex E-2: Surface condition block 2

Annex F. Force mapping

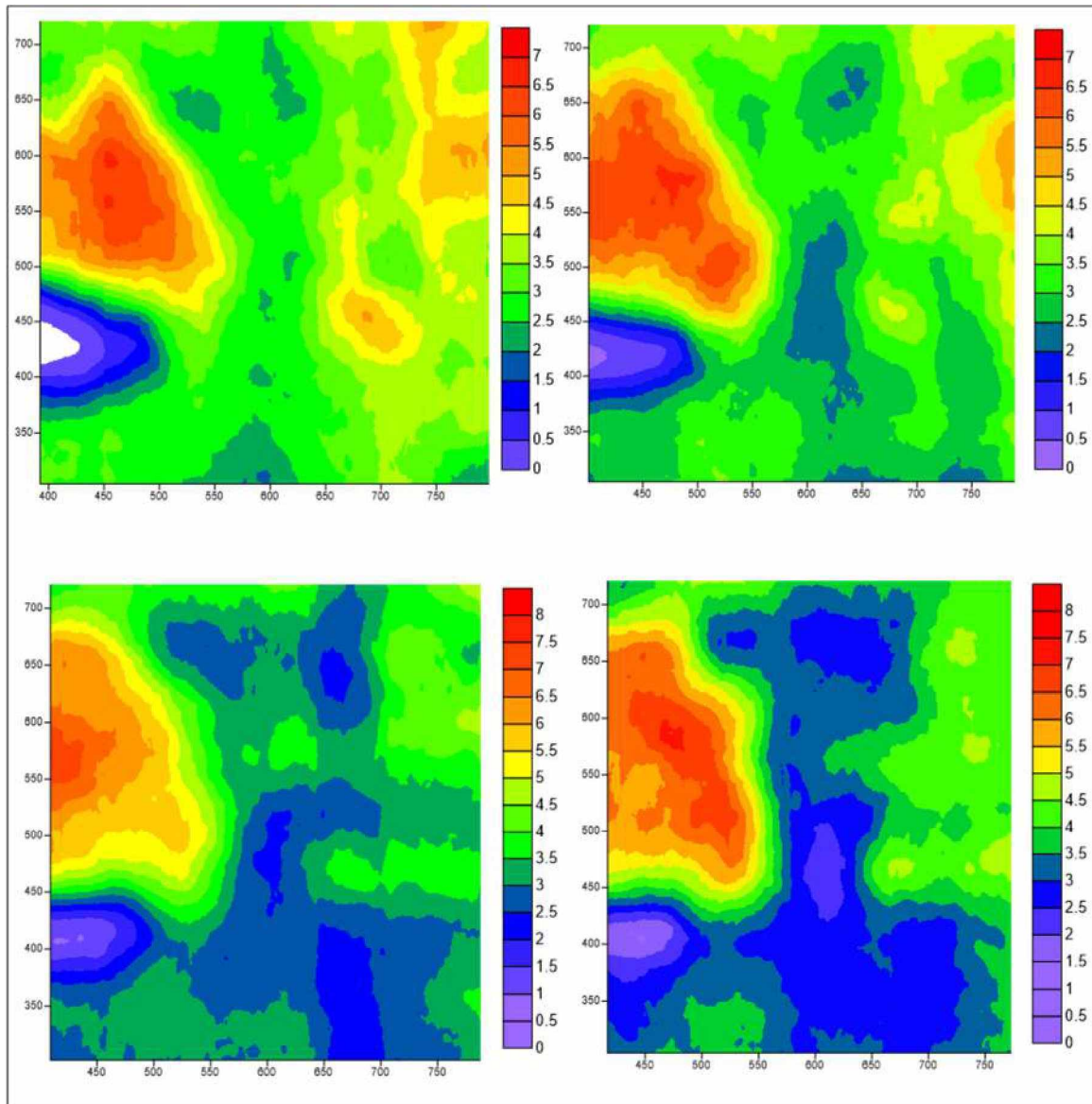


Figure Annex F-1: Force mapping of average cutting force F_C of block 1 (layers 3-6)

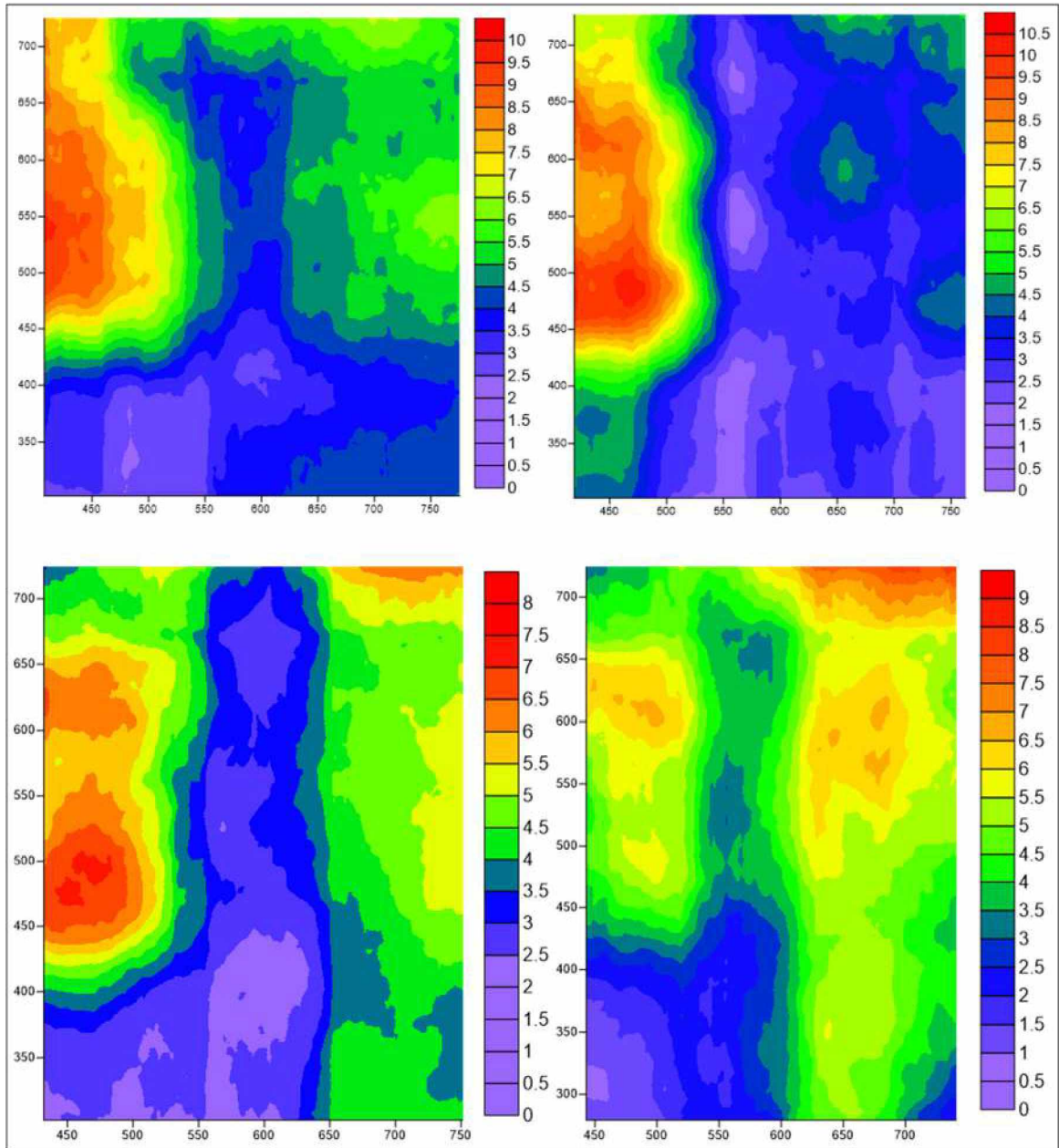


Figure Annex F-2: Force mapping of average cutting force F_C of block 1 (layers 8-12)

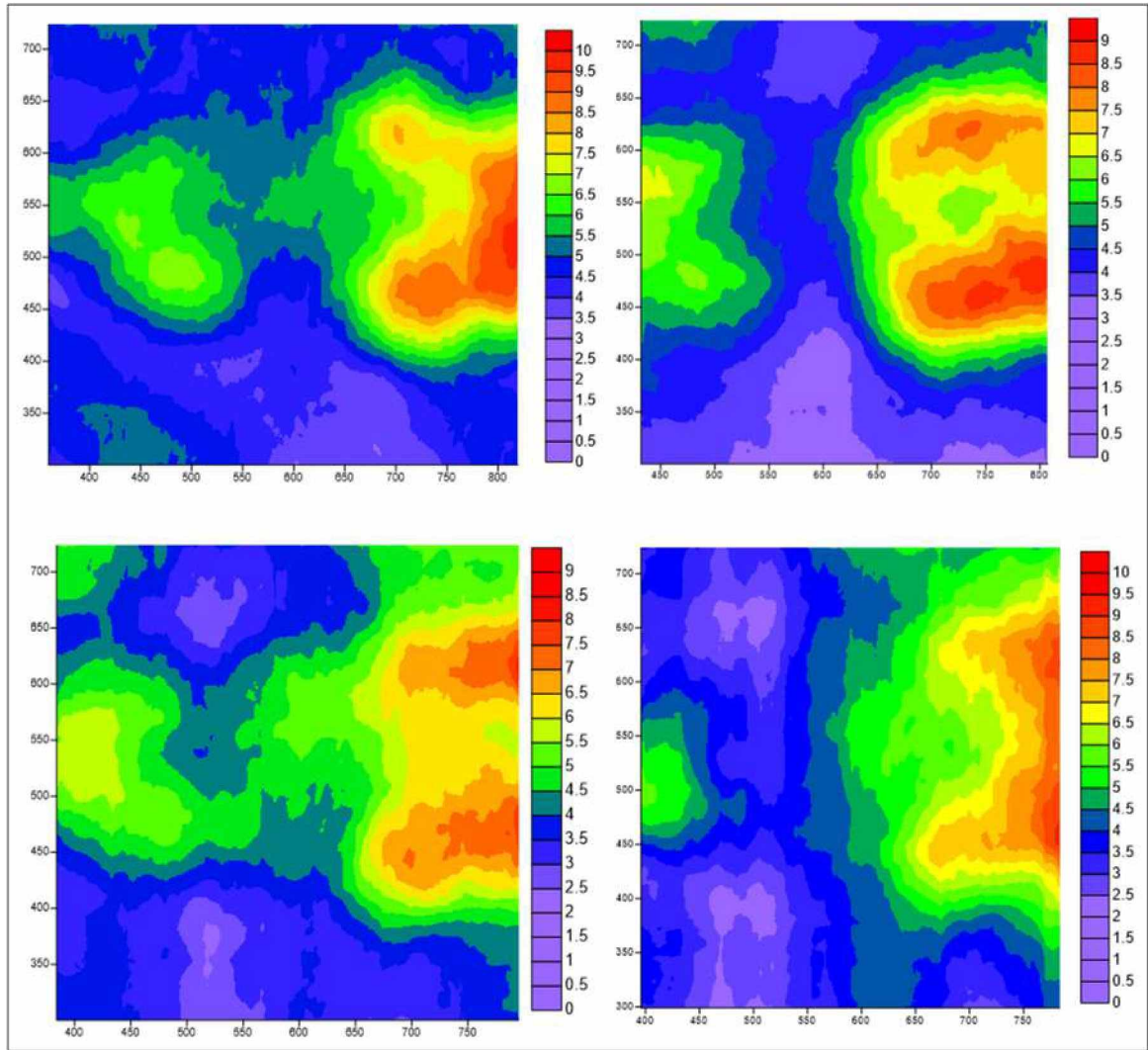


Figure Annex F-3: Force mapping of average cutting force F_C of block 2 (layers 1-4)

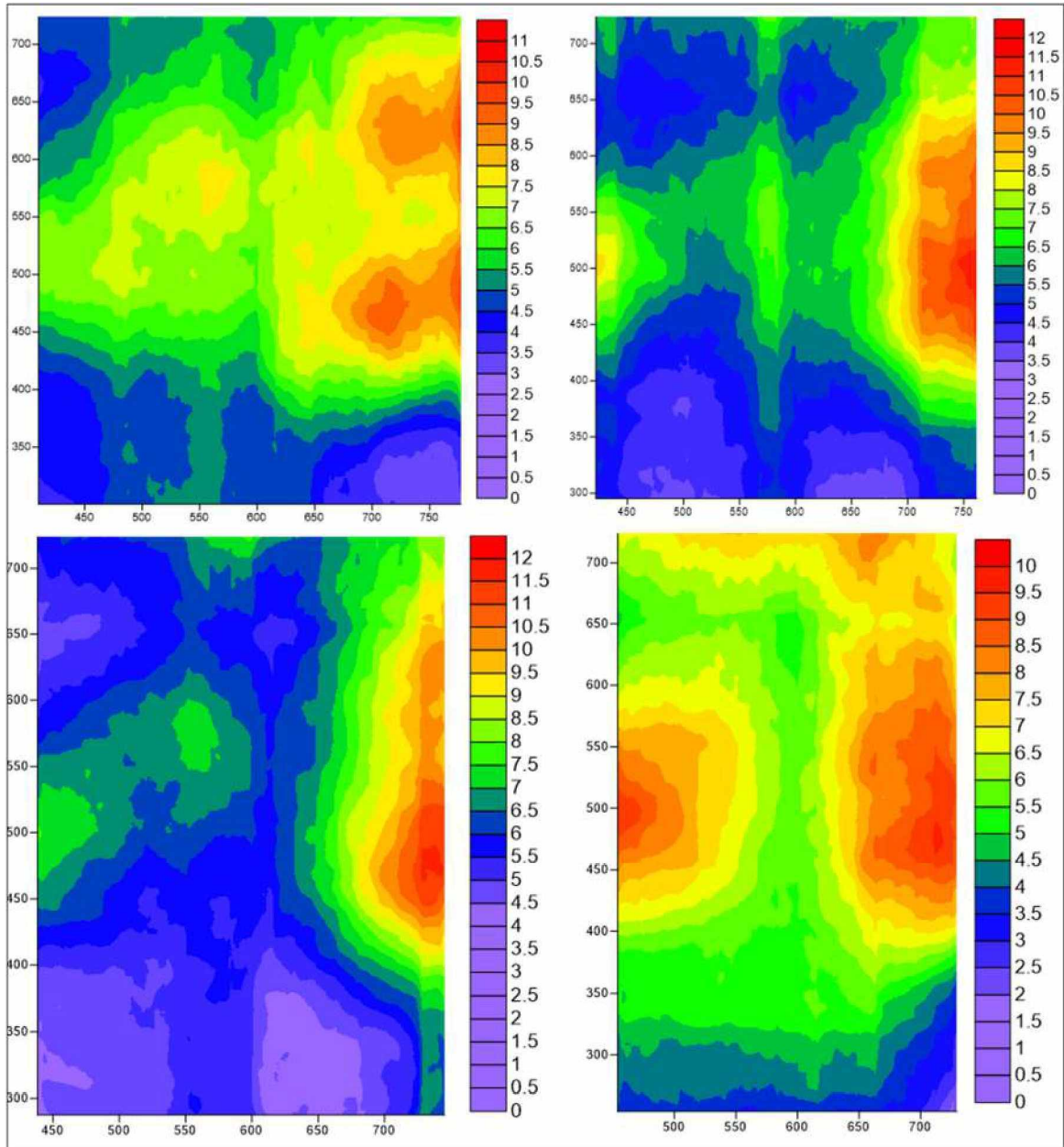


Figure Annex F-4: Force mapping of average cutting force F_C of block 2 (layers 6-9)

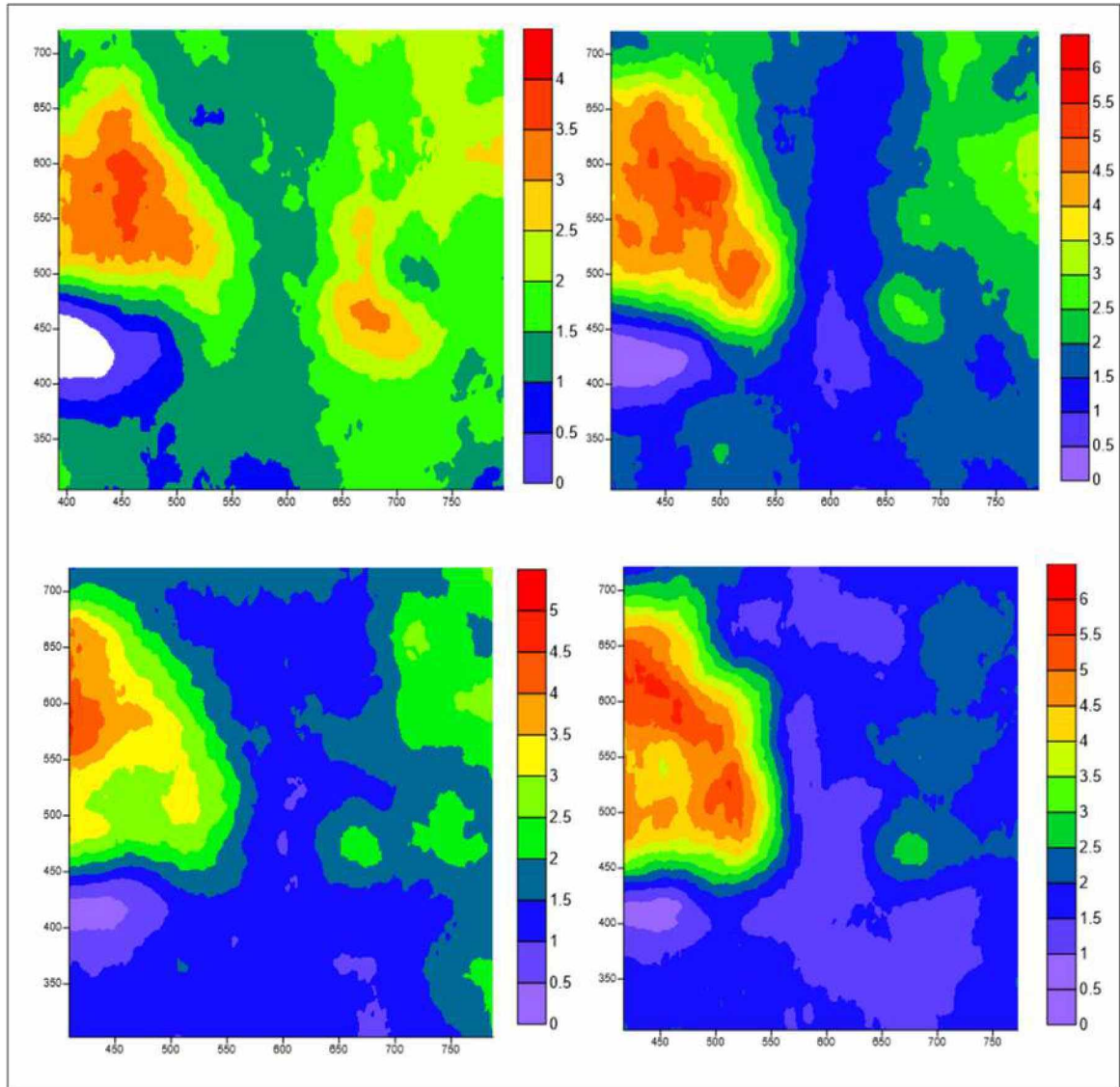


Figure Annex F-5: Force mapping of average side force F_s of block 1 (layers 3-6)

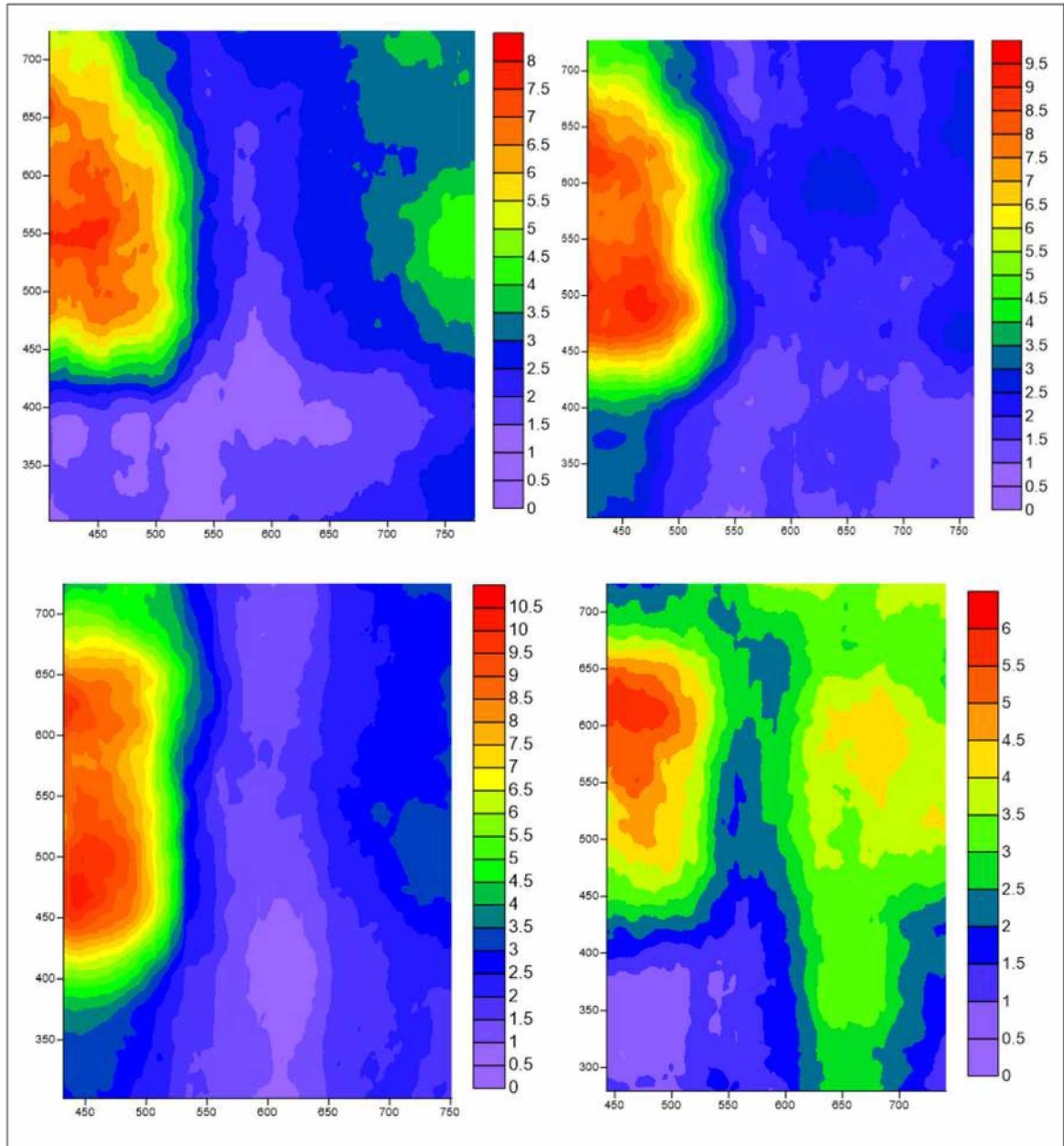


Figure Annex F-6: Force mapping of average side force F_S of block 1 (layers 8-11)

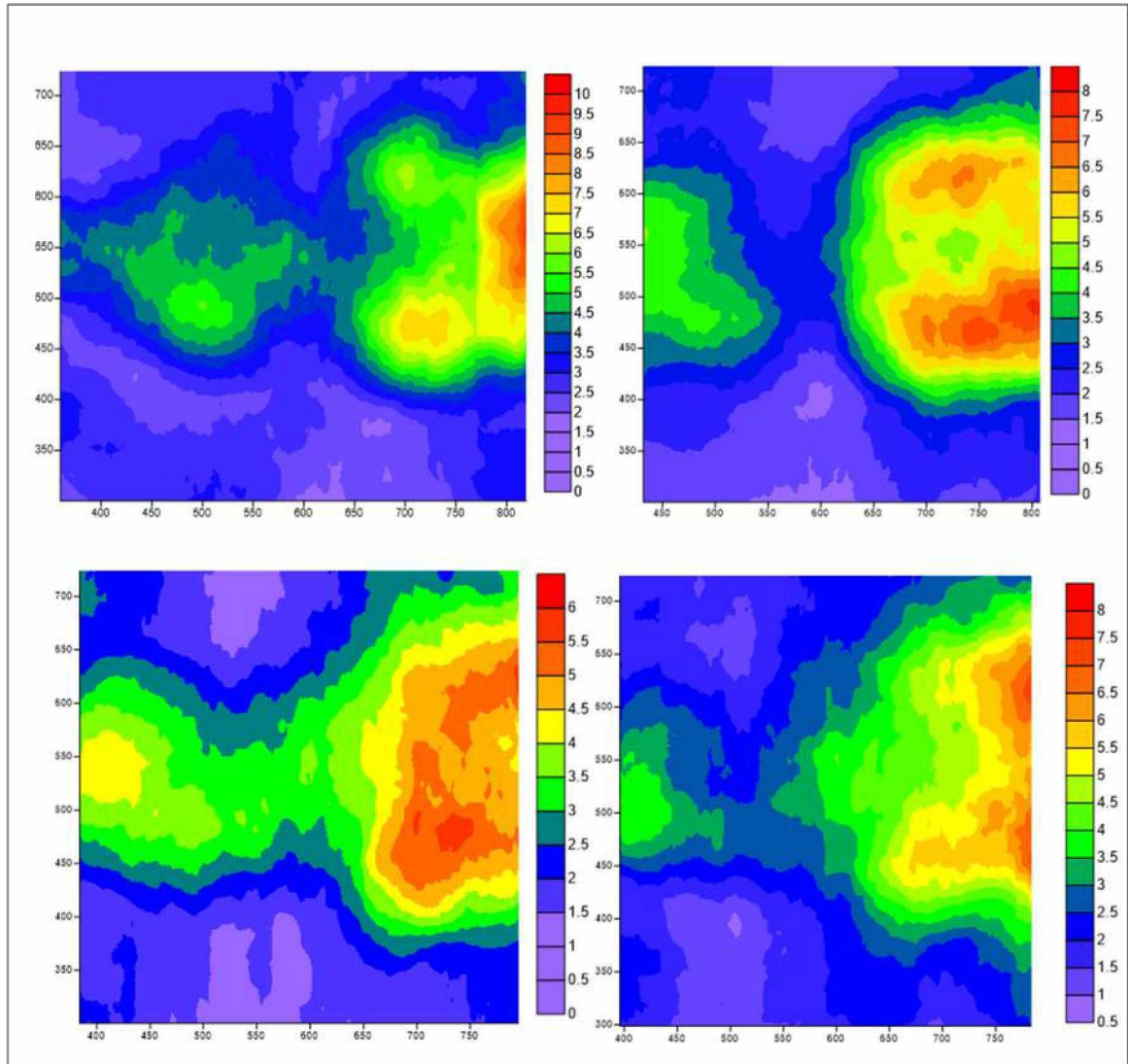


Figure Annex F-7: Force mapping of average side force F_s of block 2 (layers 1-4)

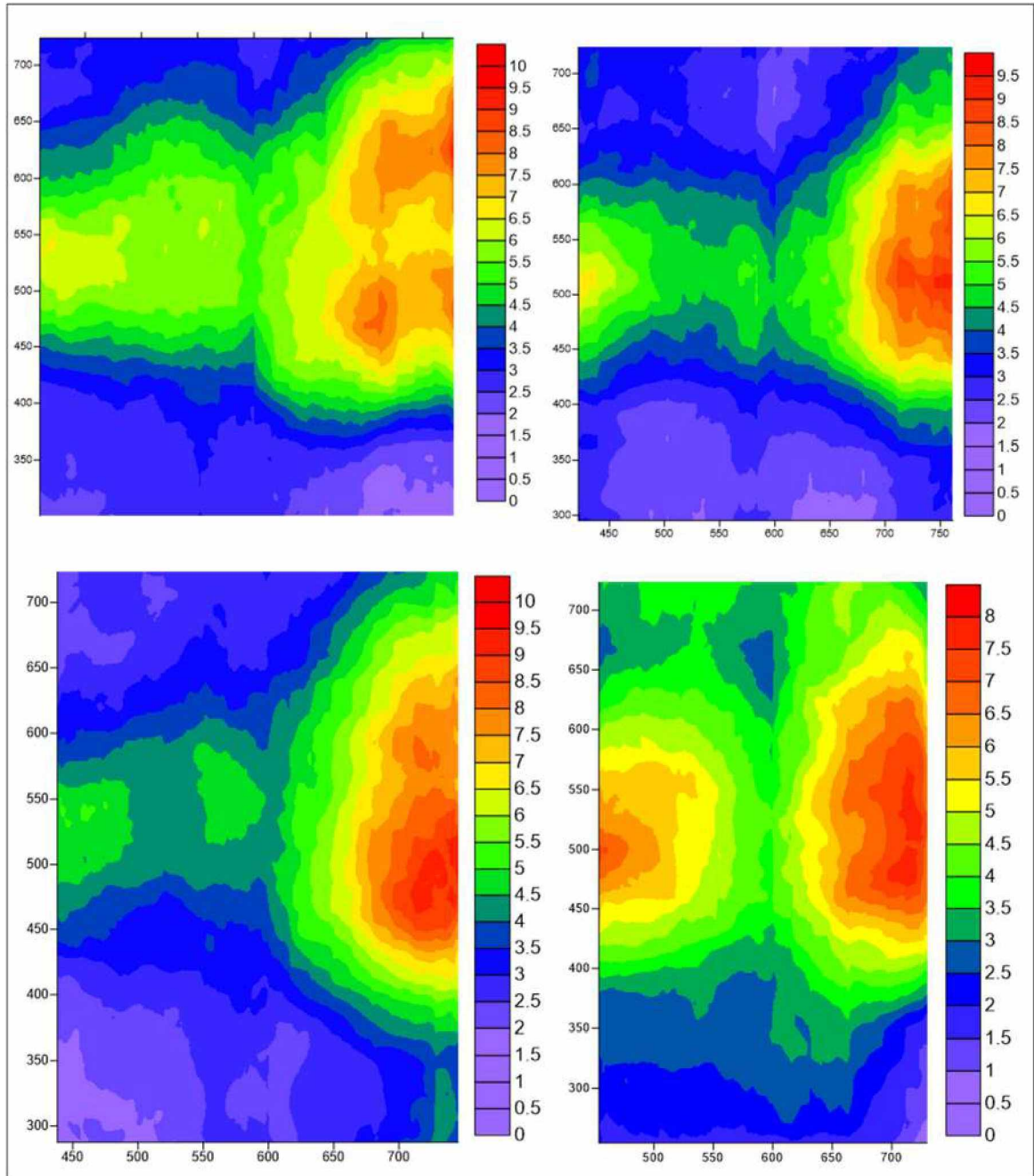


Figure Annex F-8: Force mapping of average side force F_S of block 2 (layers 6-9)

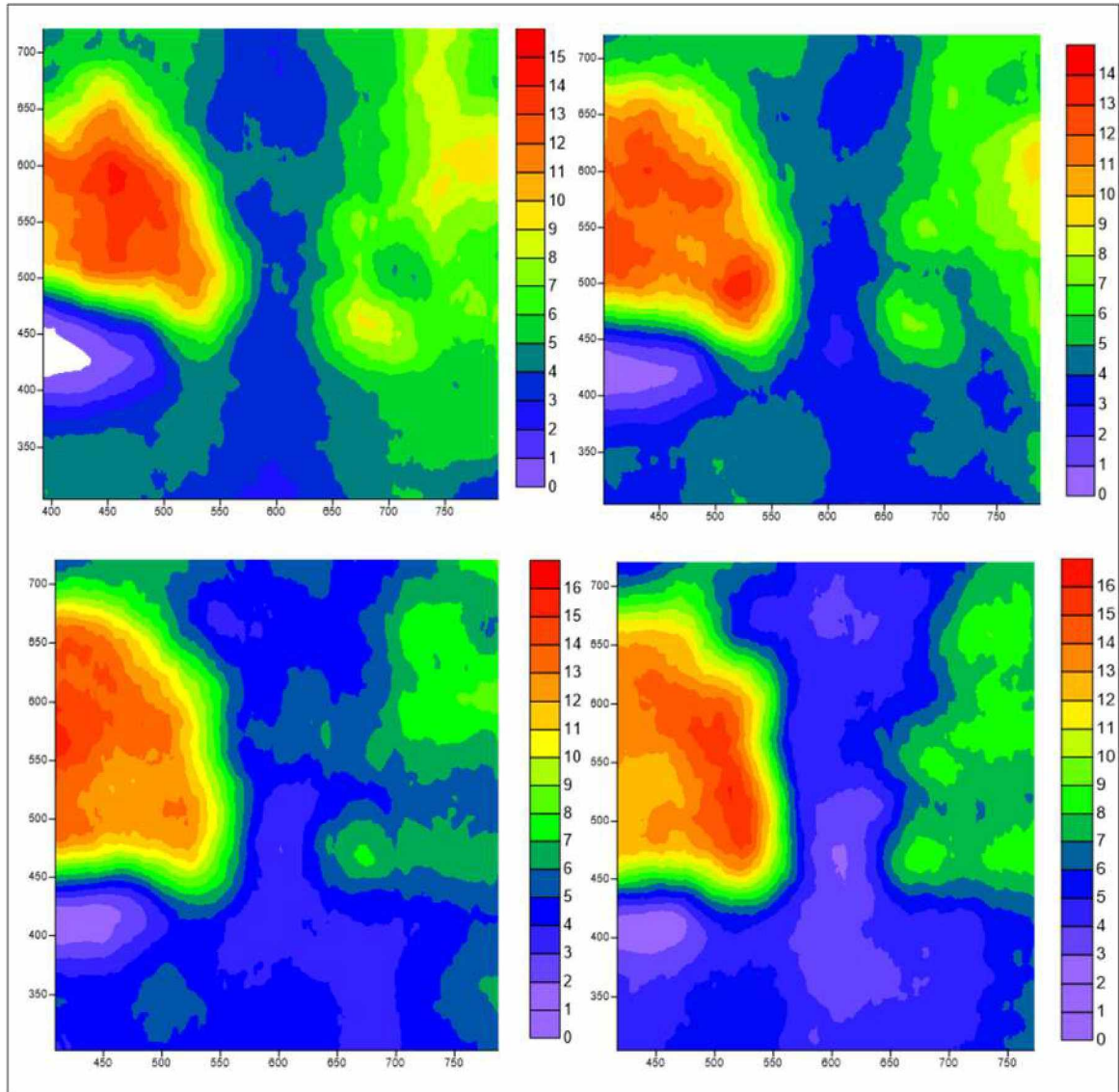


Figure Annex F-9: Force mapping of average normal force F_N of block 1 (layers 3-6)

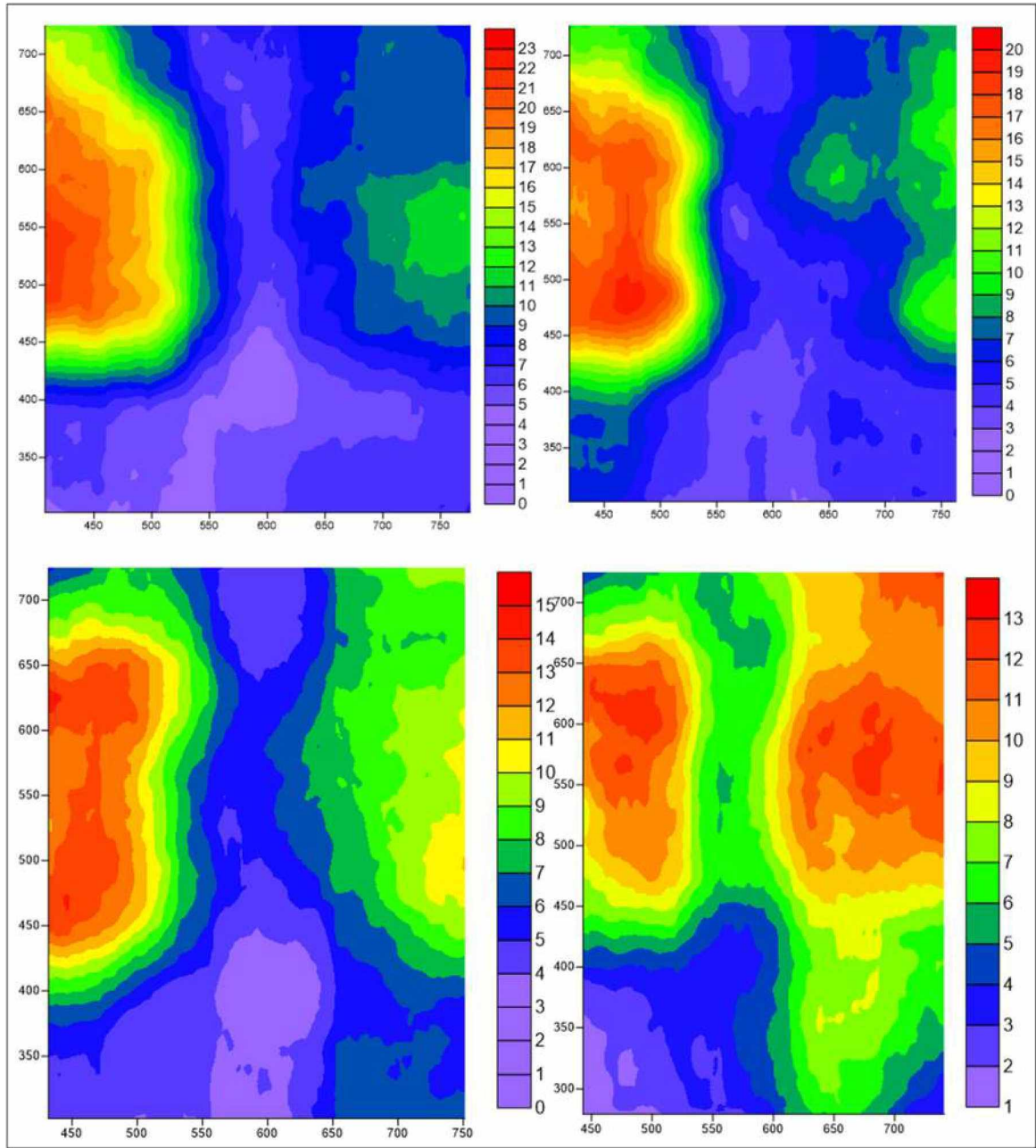


Figure Annex F-10: Force mapping of average normal force F_N of block 1 (layers 8-11)

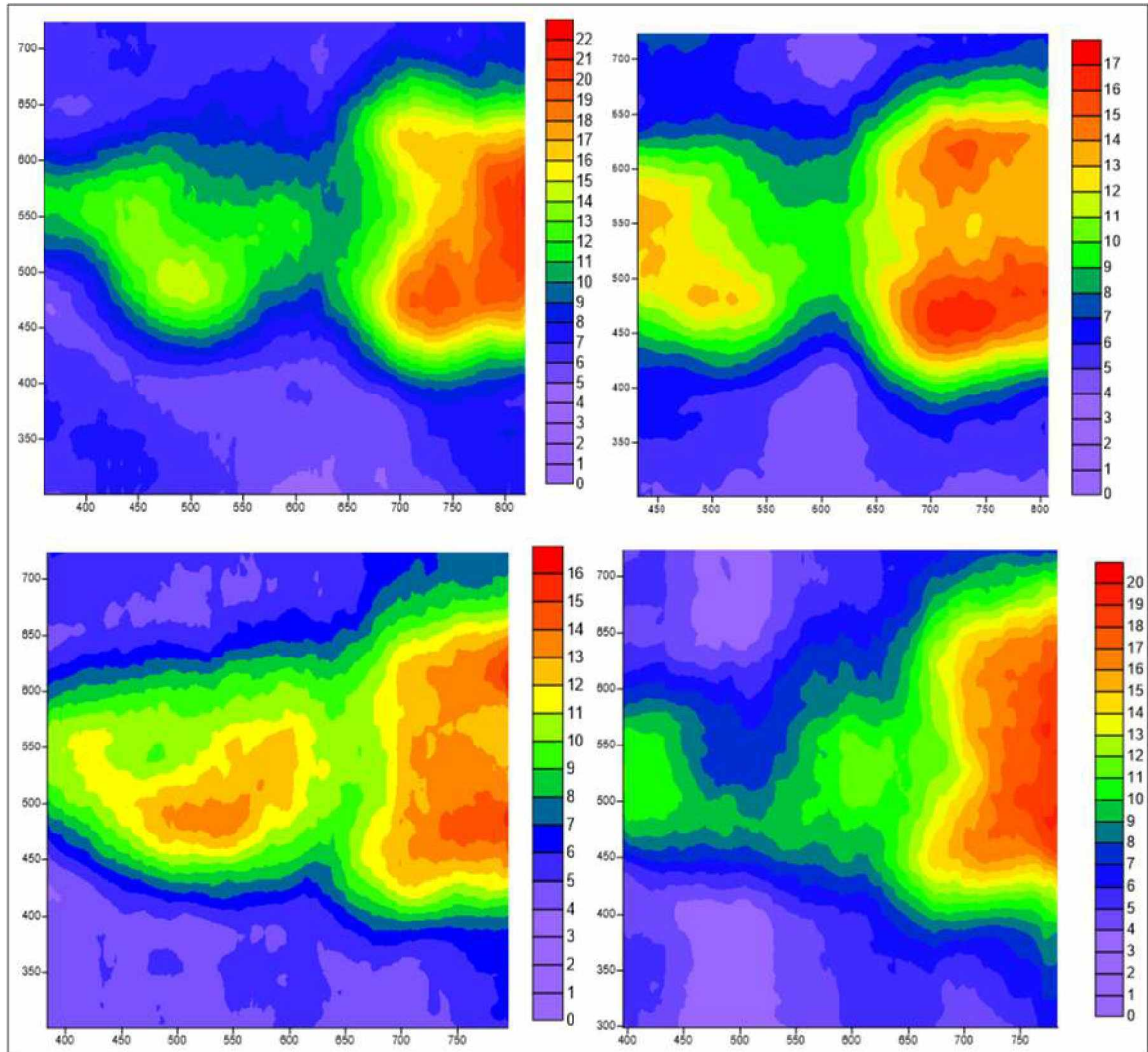


Figure Annex F-11: Force mapping of average normal force F_N of block 2 (layers 1-4)

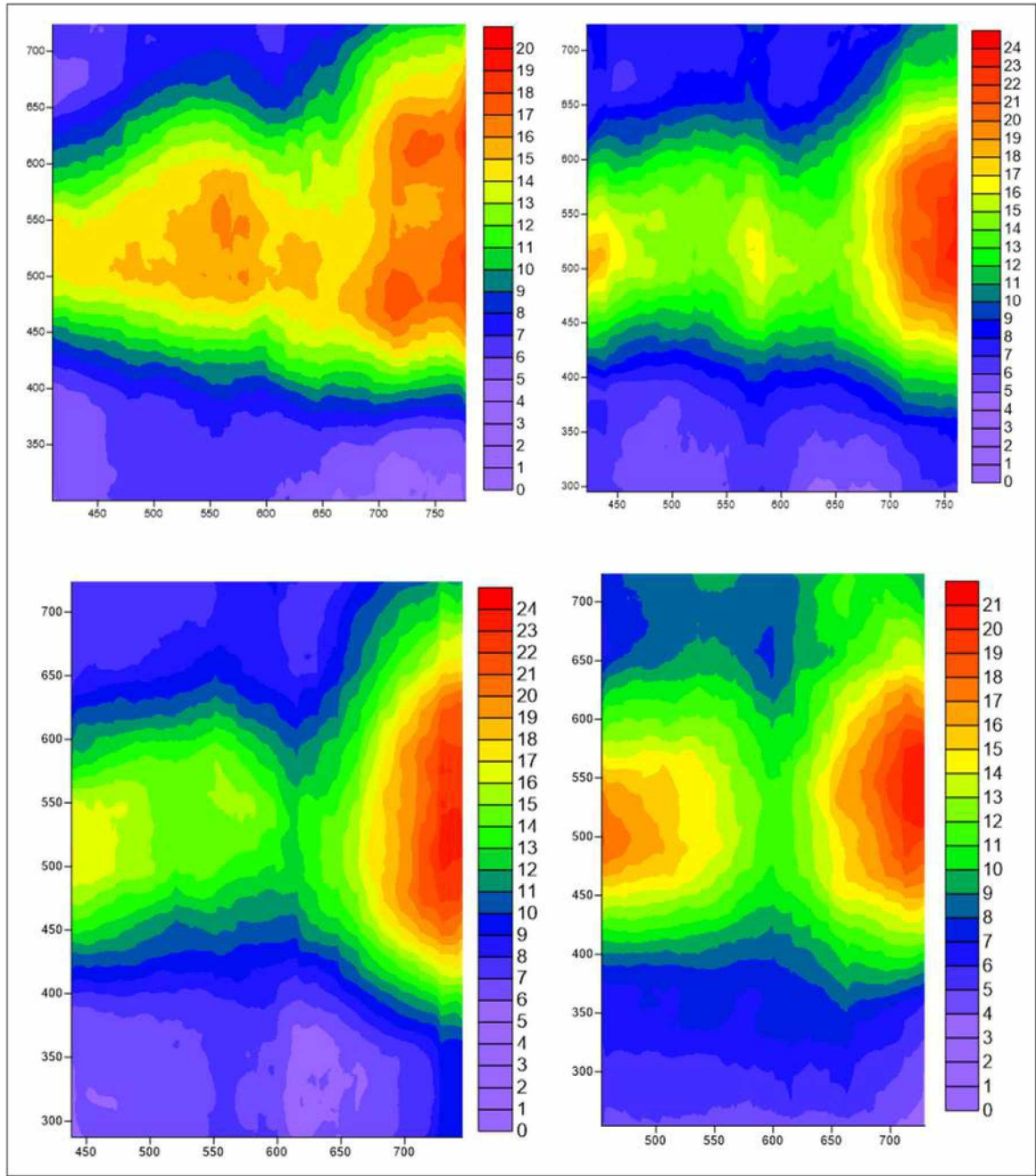


Figure Annex F-12: Force mapping of average normal force F_N of block 2 (layers 6-9)

Annex G. Element distribution maps

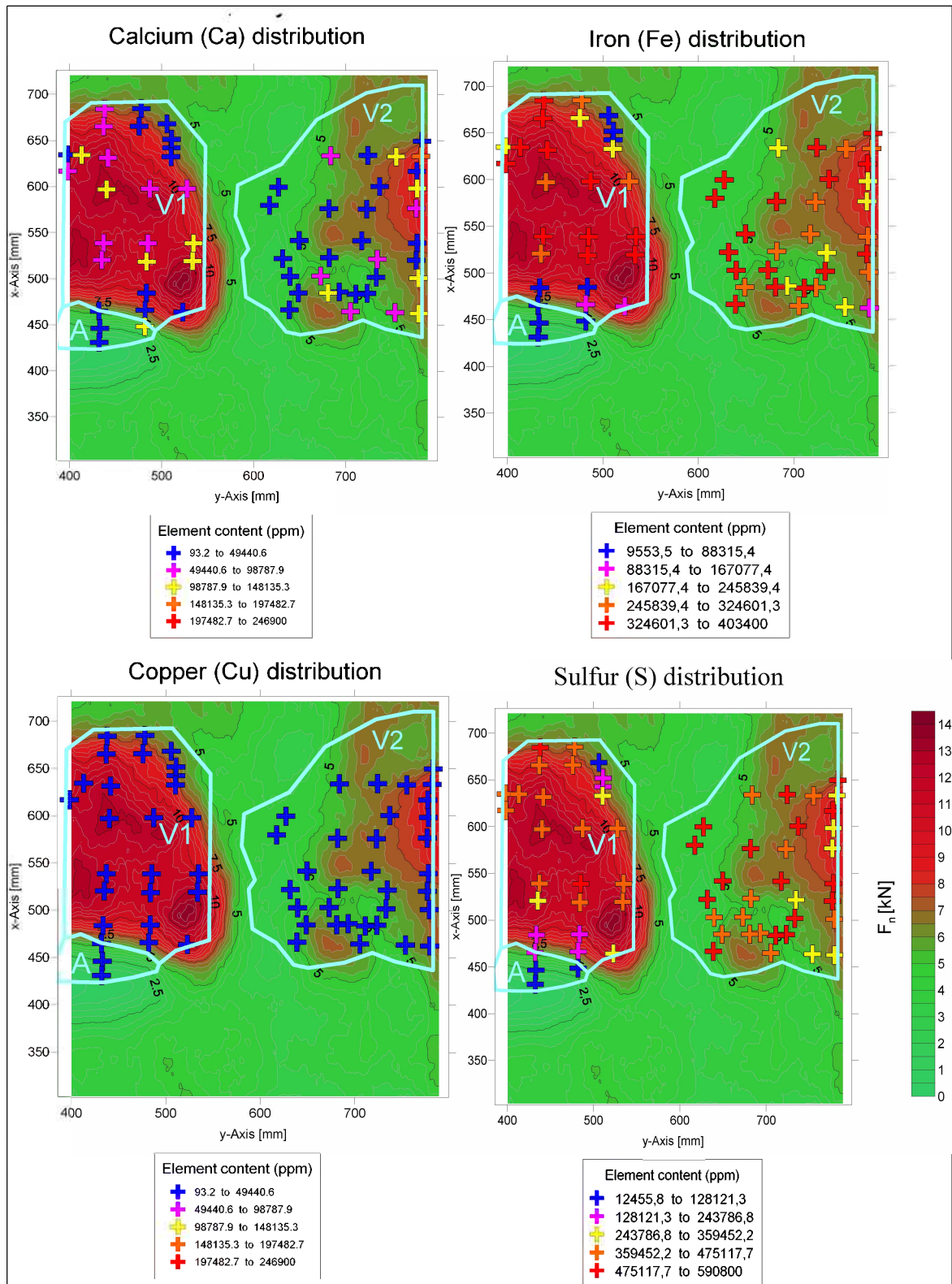


Figure Annex G-1: Element distribution block 1, layer 4: Calcium, Iron, Copper and Sulfur

Annex G Element distribution maps

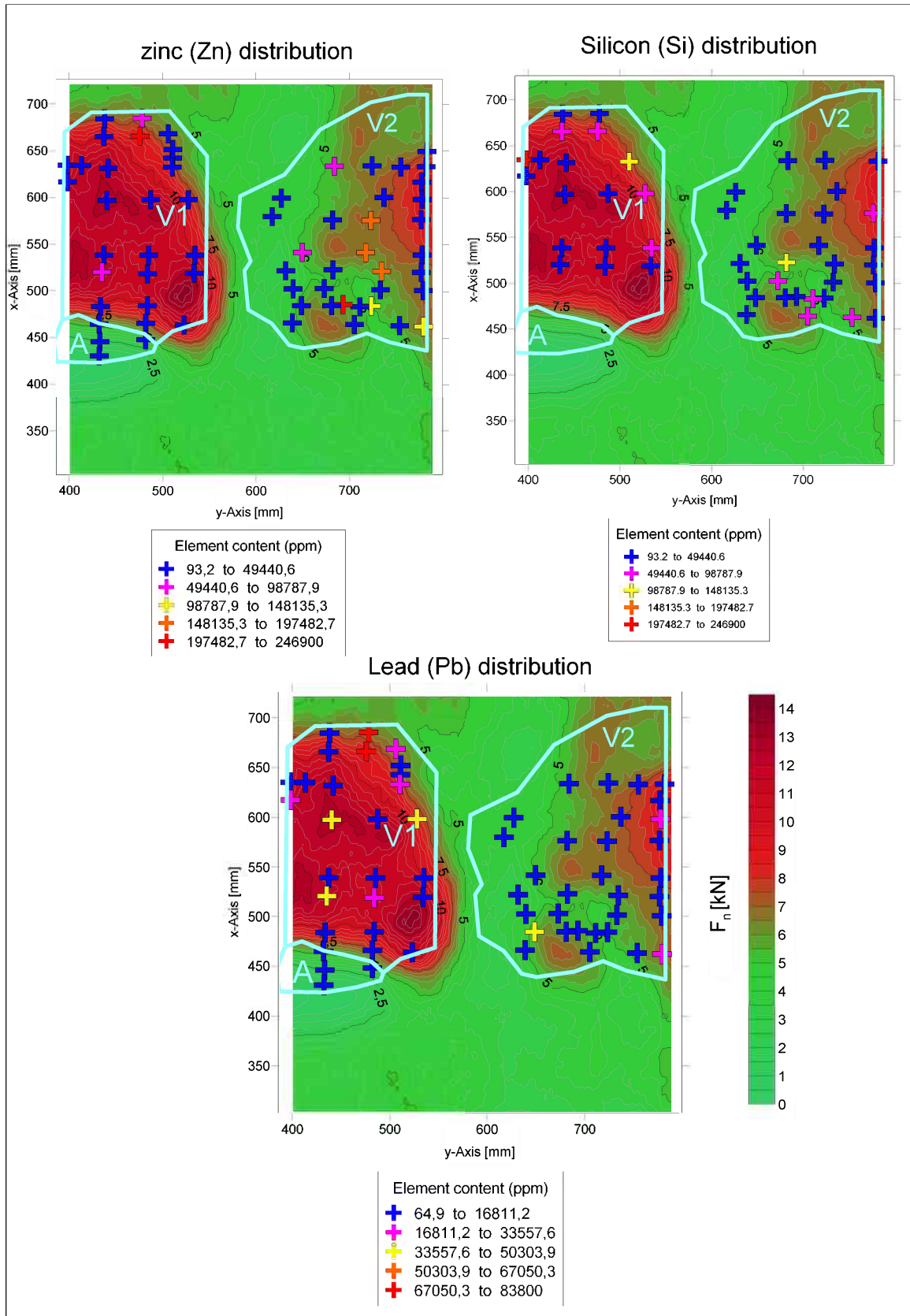


Figure Annex G-2: Element distribution block 1, layer 4: Zinc, Silicon and Lead

Annex G Element distribution maps

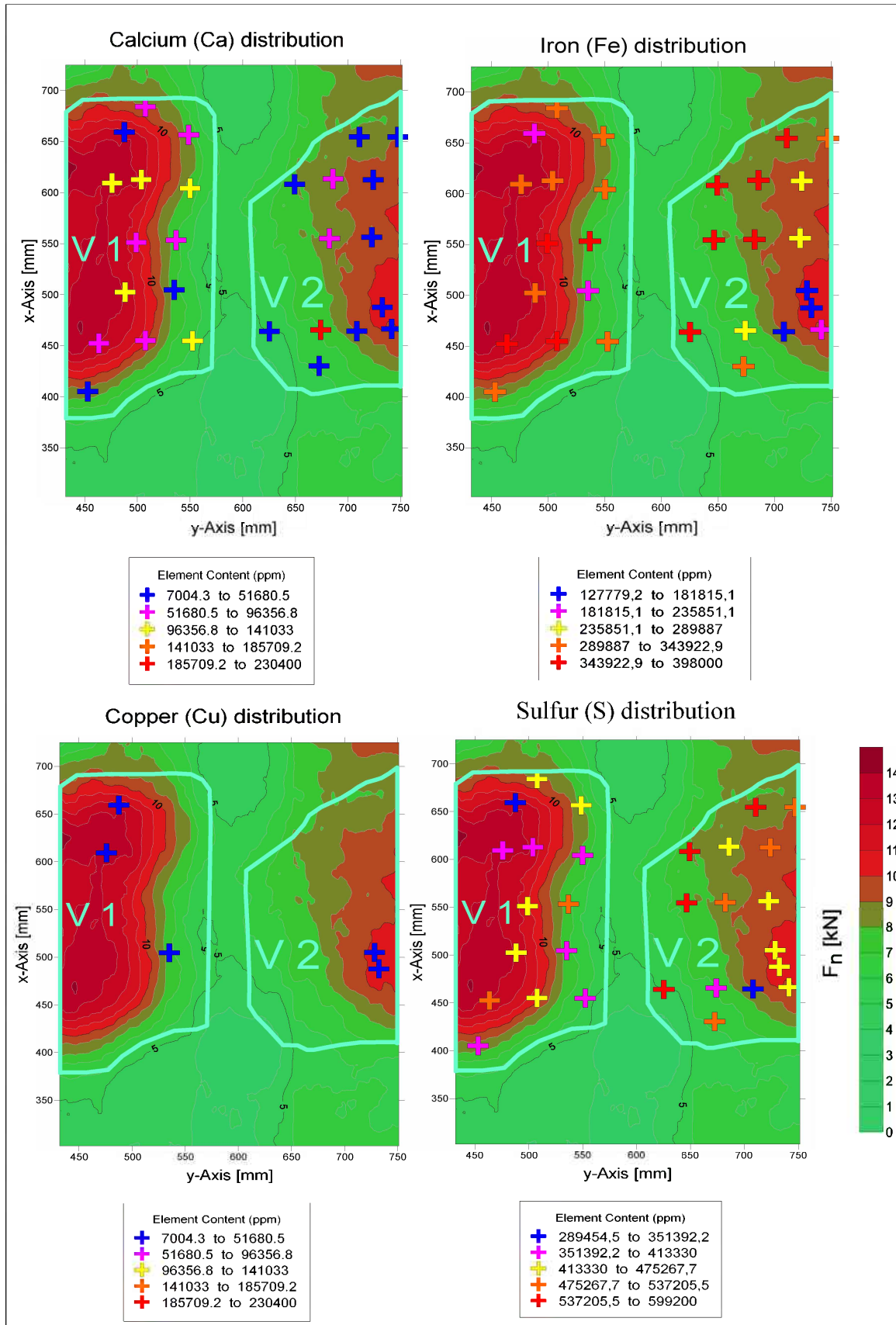


Figure Annex G-3: Element distribution block 1, layer 10: Calcium, Iron, Copper and Sulfur

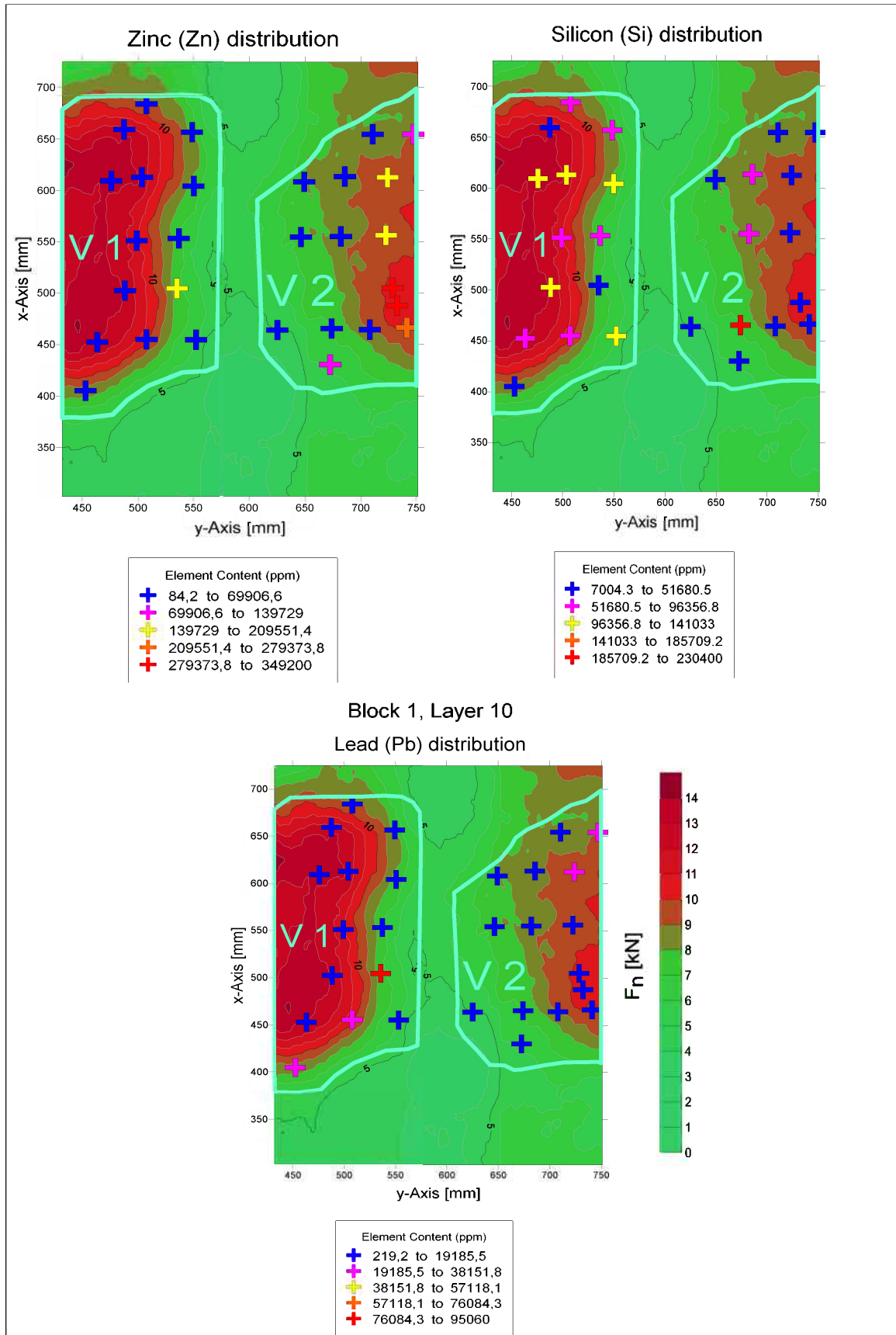


Figure Annex G-4: Element distribution block 1, layer 10: Zinc, Silicon and Lead

Annex G Element distribution maps

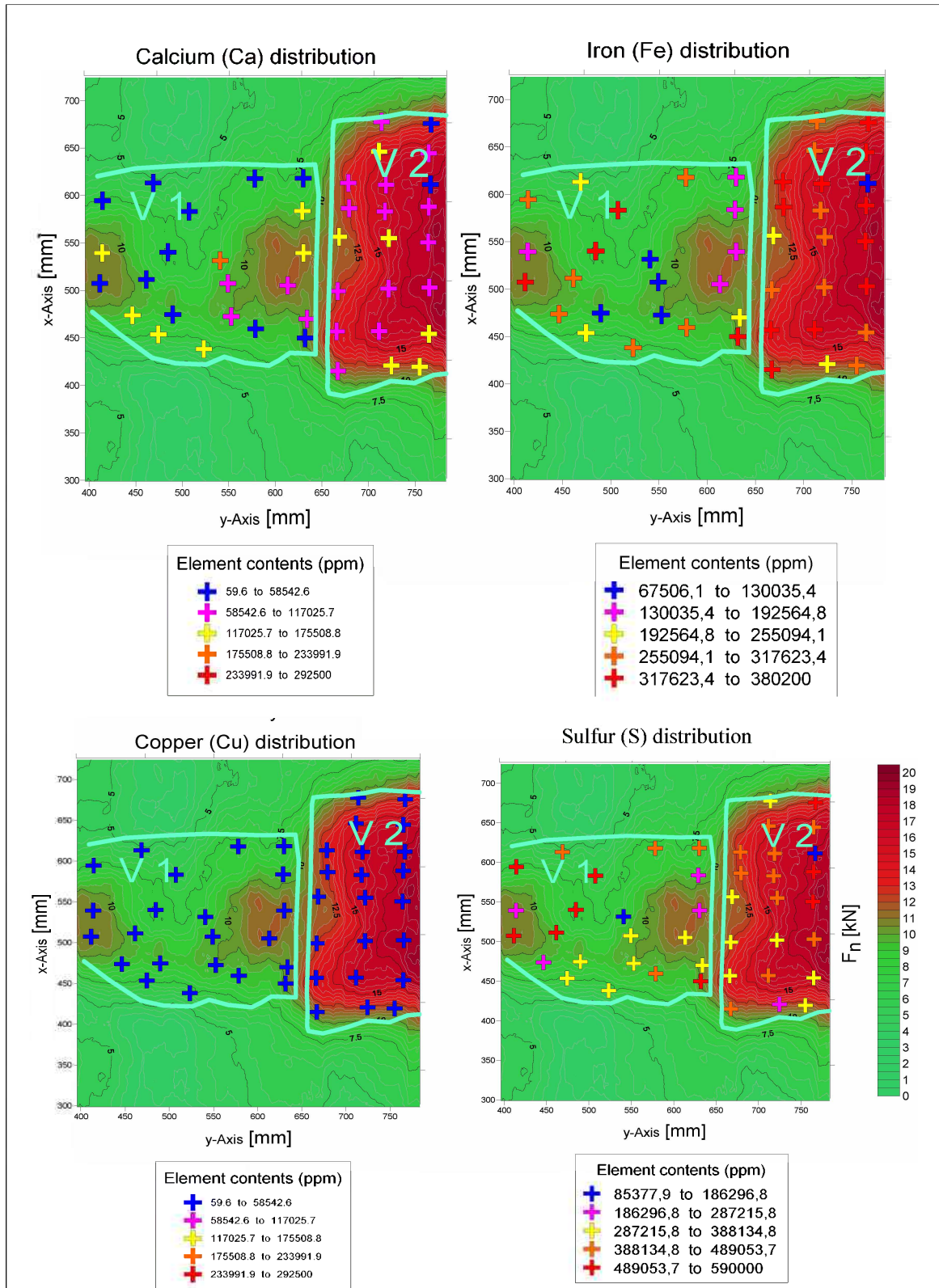


Figure Annex G-5: Element distribution block 2, layer 3: Calcium, Iron, Copper and Sulfur

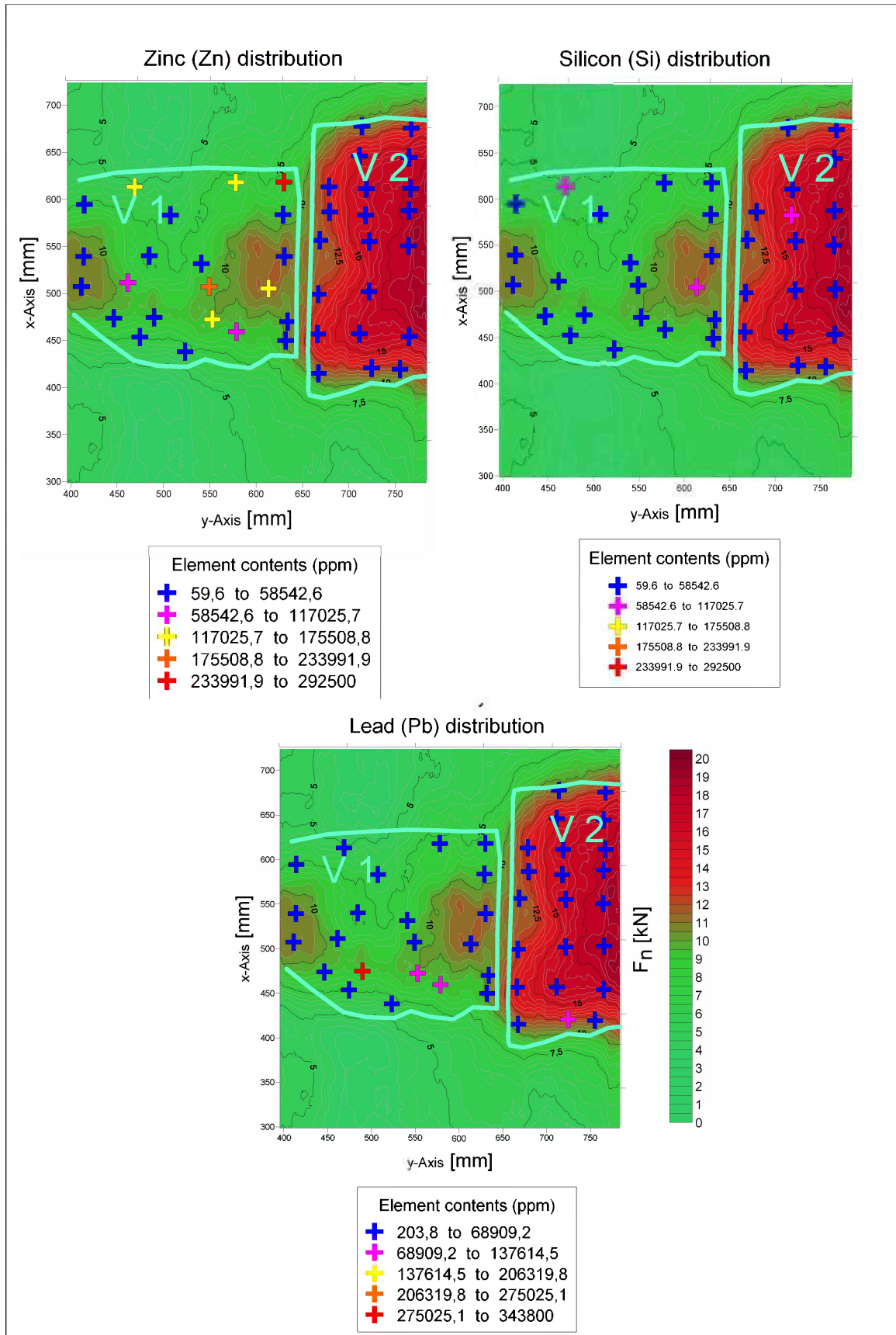


Figure Annex G-6: Element distribution block 2, layer 3: Zinc, Silicon and Lead

Annex G Element distribution maps

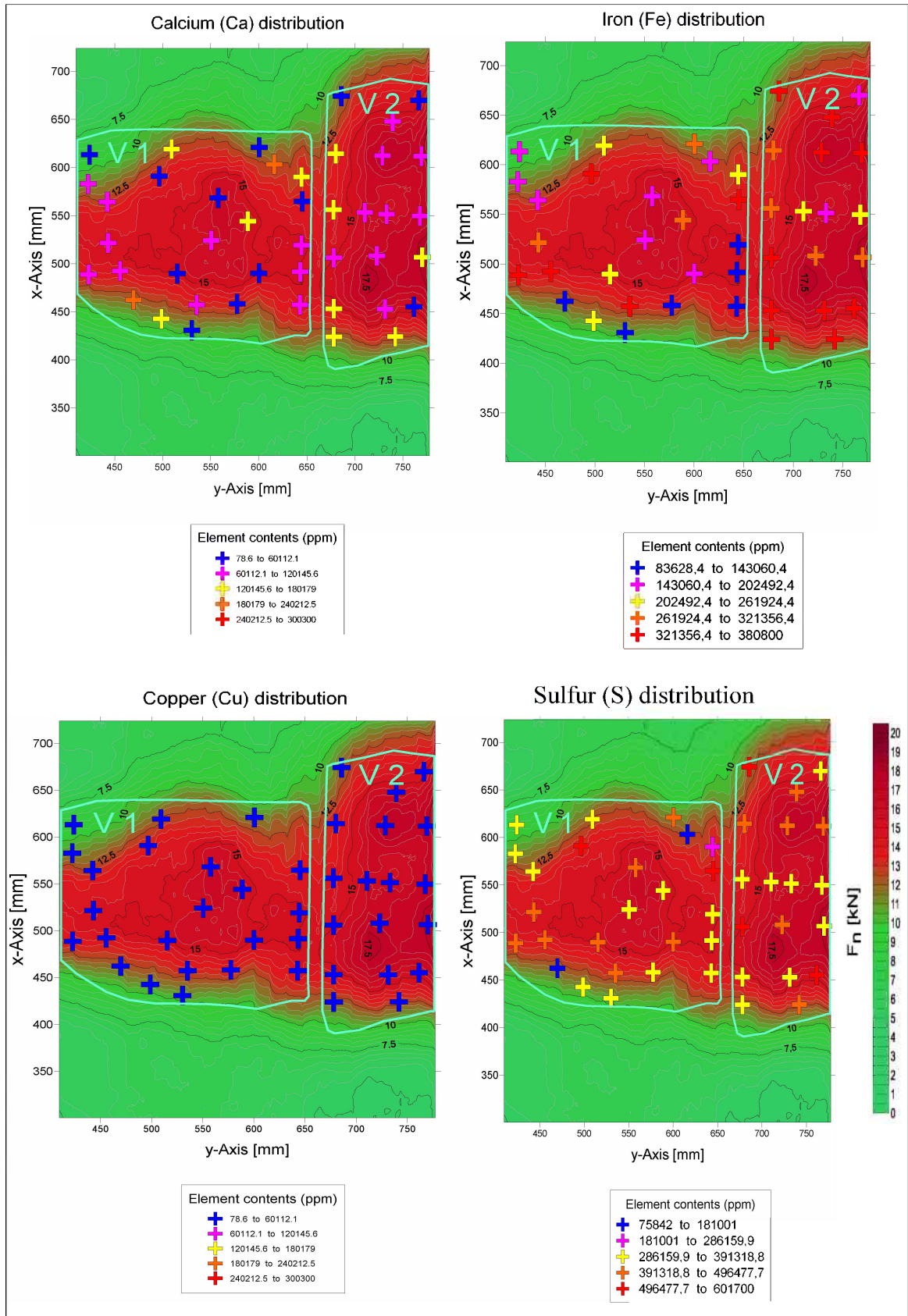


Figure Annex G-7: Element distribution block 2, layer 6: Calcium, Iron, Copper and Sulfur

Annex G Element distribution maps

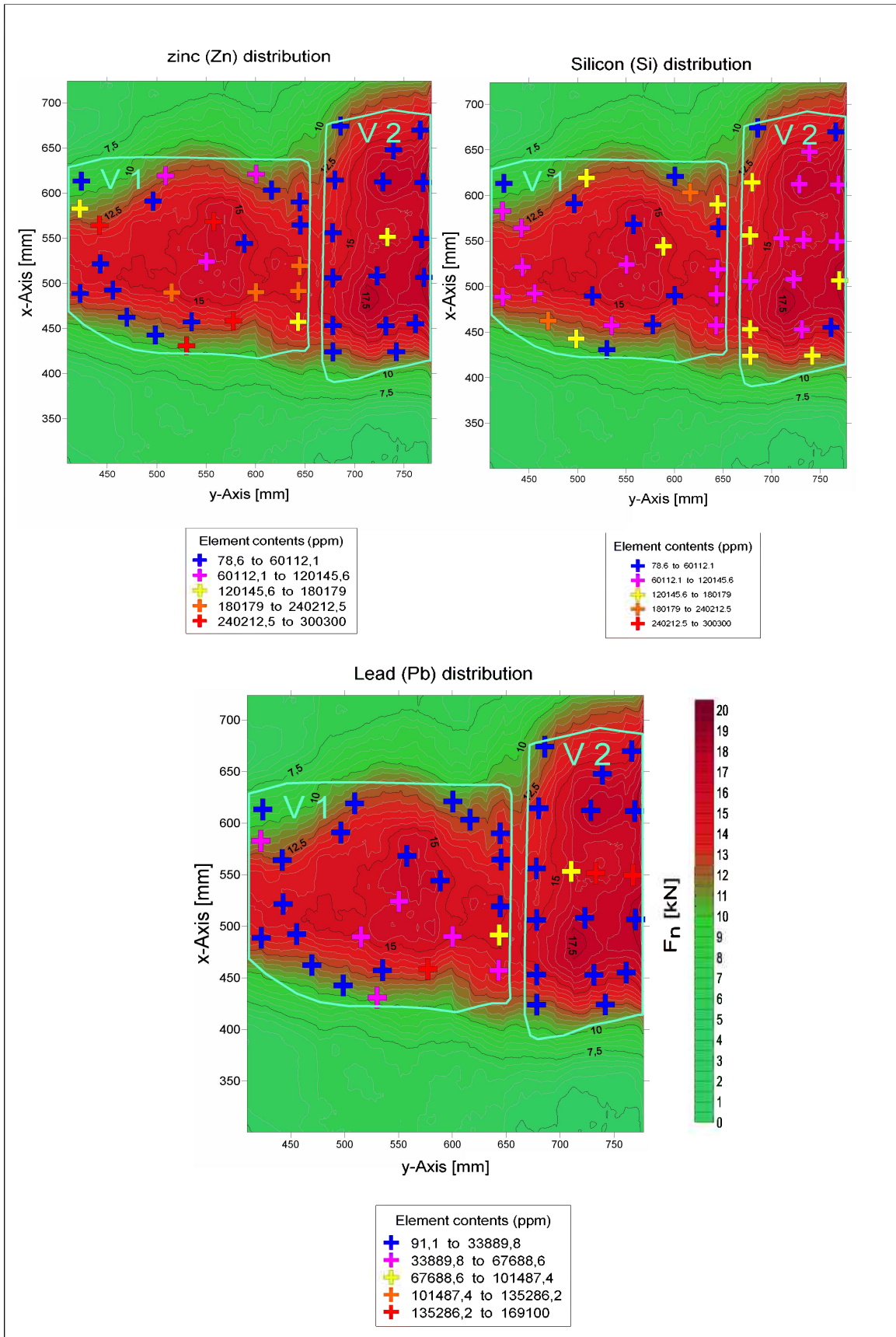


Figure Annex G-8: Element distribution block 2, layer 6: Zinc, Silicon and Lead

hXRF measurement – Block 1, Layer 4 (1)

Reading No	x-Axis	y-Axis	Ca	Cu	Fe	Pb	S	Si	Zn
2115	782.92	816.56	42894.49	176.20	403363.34	< LOD	508018.50	< LOD	2328.46
2116	781.84	800.27	153263.48	167.92	275409.09	301.81	291190.94	6146.54	999.25
2117	754.93	799.88	115797.37	178.91	311041.06	280.85	389562.72	< LOD	1281.59
2118	724.28	801.25	16362.62	217.41	385717.53	2838.09	577077.88	6564.53	1856.37
2119	683.81	800.86	83778.66	778.09	227749.39	619.96	389390.25	31198.41	74362.41
2120	777.32	783.78	21799.00	125.04	403033.56	256.26	562768.69	< LOD	470.56
2121	777.71	765.33	126760.70	166.02	240806.23	33193.79	317954.00	< LOD	838.05
2122	737.05	767.49	18314.89	613.42	378411.22	1540.51	514353.22	11670.94	19054.95
2123	627.24	766.71	37277.33	230.07	366889.34	284.67	519425.28	27563.28	5173.33
2124	776.73	743.74	94449.10	105.96	222870.47	291.51	317297.09	63221.72	963.51
2125	723	742.9	15482.34	4324.36	250550.80	4043.75	451238.81	7397.34	184114.72
2126	681.96	743.49	18384.75	2344.51	399583.97	591.28	559339.63	8883.12	3263.68
2127	617.32	747.06	12466.99	330.66	361240.69	471.60	580208.13	34631.97	2197.80
2128	777.71	706.05	10077.92	258.31	309397.47	162.69	561232.81	4927.08	2429.85
2129	717.44	708.62	7882.23	6972.12	298988.19	715.07	488950.72	12196.79	155539.69
2130	649.64	708.82	10101.21	3598.20	347330.84	8736.35	509189.19	8639.40	69025.12
2131	776.72	687.43	46225.48	397.55	355954.22	635.71	481759.25	21969.31	9688.84
2132	734.49	688.62	85740.81	1817.74	170254.83	372.23	296366.69	23404.92	167691.02
2133	682.35	690.2	13344.70	763.79	272660.94	246.71	445795.47	137968.97	4707.73
2134	631.8	689.21	12590.50	2025.50	346808.47	4516.93	566838.13	30138.94	6193.81

hXRF measurement – Block 1, Layer 4 (2)

Reading No	x-Axis	y-Axis	Ca	Cu	Fe	Pb	S	Si	Zn
2135	778.9	668.01	120941.39	463.21	301824.38	448.87	378345.50	7650.41	15831.75
2136	733.1	668.9	6243.77	374.37	374731.25	251.51	590783.25	17230.09	1229.92
2137	673.01	670.3	54985.55	2923.72	353996.34	642.43	450435.63	97895.71	14805.57
2138	639.68	669.9	28242.79	2572.90	375416.16	8853.31	467041.59	35124.63	782.36
2139	723.32	651.55	23374.72	1850.25	250873.36	64.94	548341.31	6067.54	142553.31
2140	711.14	650.75	6170.32	2587.71	327487.59	169.42	519791.53	56054.79	38216.59
2141	693.18	653.14	30735.72	5179.03	202178.31	2678.43	460851.75	28104.93	246830.06
2142	681	651.94	104535.41	627.80	331605.19	1761.80	406683.00	23561.89	569.38
2143	648.66	651.94	13484.34	14419.49	319777.72	49393.75	459195.09	28417.61	333.01
2144	779.22	629.6	99713.30	2194.93	166121.66	30502.38	316141.50	22145.20	117551.44
2145	753.66	630.6	92670.97	134.79	228800.67	113.72	295839.63	61156.12	11080.29
2146	705.35	631.8	88301.70	2110.25	276833.31	201.77	389835.34	55917.15	16318.56
2147	638.88	633.59	4414.00	320.54	366544.28	11584.26	588092.38	17623.82	5905.26
2148	438.21	851.33	53324.27	854.84	376014.13	2452.32	503633.38	42317.20	727.53
2149	478.12	851.98	12599.16	19363.42	267864.94	83796.67	359877.66	42601.61	66356.95
2150	437.23	832.52	85237.28	3362.39	332009.84	5382.34	403534.81	50102.19	7035.06
2151	475.85	832.85	34848.47	15122.34	179421.75	68582.10	391266.53	69279.63	217602.53
2152	506.03	835.44	3748.31	235.41	40048.35	26608.40	100786.66	366259.47	410.14
2153	510.8	809.59	16890.35	522.61	64148.27	10803.46	157972.70	351640.56	1190.74
2154	511.01	818.73	2918.41	877.88	73101.24	9860.46	230347.61	301327.28	468.44

hXRF measurement – Block 1, Layer 4 (3)

Reading No	x-Axis	y-Axis	Ca	Cu	Fe	Pb	S	Si	Zn
2155	510.4	799.83	29421.10	2092.07	215818.31	20890.91	339794.00	140720.17	16210.46
2156	398.16	801.86	5115.04	< LOD	176939.94	349.45	395174.22	244387.27	93.29
2157	413.41	801.66	99424.42	257.97	332916.06	16652.68	416737.47	19357.83	153.55
2158	441.87	798.61	59221.31	4227.98	338533.22	7254.87	451149.59	37111.78	20454.74
2159	398.36	784.19	79541.37	6920.14	340245.72	31230.47	429415.09	7987.05	309.42
2160	440.45	764.28	104577.23	1081.01	280537.59	33944.62	366763.47	32030.49	943.74
2161	487.42	765.09	72015.43	449.91	367154.19	2977.39	471422.19	26589.88	1288.52
2162	527.68	765.09	58710.70	611.47	287970.72	35760.08	392574.34	54330.41	5534.42
2163	437.29	706.06	93496.13	412.68	332466.28	1785.02	429719.16	28789.73	2859.83
2164	485.22	705.85	65445.57	153.57	375295.22	949.73	497926.88	20138.81	272.46
2165	534.79	705.85	102376.03	296.36	332229.53	3405.21	429010.16	51004.24	1045.88
2166	435.24	687.77	92291.95	7418.19	262565.56	34255.88	332831.50	11110.59	50919.01
2167	483.98	685.92	110701.95	276.07	338084.38	17529.53	414998.13	42815.38	402.28
2168	533.76	686.54	125374.72	939.58	334612.31	3834.41	390660.31	41213.82	304.59
2169	433.8	651.19	< LOD	228.56	83711.18	1137.33	156852.05	427869.53	102.29
2170	483.78	651.8	17735.96	295.44	86833.60	908.69	198568.48	280195.59	139.91
2171	432.15	632.28	16361.08	248.54	87717.60	94.31	165339.53	388335.03	223.92
2172	482.13	633.31	20864.41	214.31	105839.96	333.19	170849.36	378676.66	431.65
2173	523.06	631.25	18125.07	317.79	137712.34	4642.43	314395.22	317637.28	1946.06
2174	433.16	613.49	10160.91	170.55	55122.76	69.11	71508.59	349177.47	500.34
2175	482.04	615.56	103364.90	74.77	9553.50	88.96	33359.51	308545.06	298.84
2176	432.33	598.39	2319.51	135.23	11466.35	235.10	12455.87	367123.25	93.32

hXRF measurement – Block 1, Layer 10 (1)

Reading No	x-Axis	y-Axis	Ca	Cu	Fe	Pb	S	Si	Zn
3214	484.93	872.02	77300.71	5643.77	301729.88	736.19	428420.09	33271.29	1108.66
3215	464.68	847.08	44915.52	17615.61	223974.19	987.07	309387.31	230385.50	3654.13
3216	525.94	844.29	52490.78	606.82	343571.13	2641.72	429594.00	66039.76	1977.75
3217	453	796.64	97734.47	7653.63	301214.63	12331.79	385546.59	13601.36	21701.54
3218	480.92	800.16	99208.06	257.25	313995.75	2148.46	382079.06	22322.95	157.11
3219	527.28	791.47	118997.71	529.94	336195.78	11954.72	369228.59	15121.74	90.41
3220	476.13	737.97	90615.61	193.72	367344.06	2955.37	473483.28	< LOD	168.42
3221	513.99	740.12	77623.05	240.95	360996.31	4048.11	482163.66	12603.17	155.70
3222	465.42	688.9	107888.59	< LOD	341157.31	4313.95	444991.47	< LOD	115.59
3223	512.39	691.05	47835.77	14244.71	202617.45	95050.66	372304.34	11711.12	146608.77
3224	440.54	638.38	85144.53	208.28	381553.28	303.82	478433.00	7292.87	84.28
3225	484.77	641.07	75068.13	1159.26	349408.94	23591.69	457349.31	< LOD	101.88
3226	529.72	640.71	128308.56	109.65	317951.69	495.01	382706.53	16016.83	123.08
3227	429.93	590.76	37330.95	2574.57	294832.47	20308.40	367634.66	104210.88	6959.80
3228	688.51	842.22	22151.02	705.95	354989.56	1388.36	547140.75	12558.80	36811.71

hXRF measurement – Block 1, Layer 10 (2)

Reading No	x-Axis	y-Axis	Ca	Cu	Fe	Pb	S	Si	Zn
3229	725.07	842.2	30070.44	1758.37	303910.09	30146.55	499185.75	11886.41	81198.27
3230	701.85	799.85	10829.55	3238.59	273606.94	24594.77	496359.06	7004.35	145122.14
3231	663.53	800.72	69414.38	1005.37	367682.91	395.65	467707.56	40177.59	34141.62
3232	626.95	795.5	9079.26	581.19	382600.56	1768.23	552218.13	16571.01	29193
3233	700.37	743.1	38526.9	2681.85	271783.44	915.97	470062.09	7345.73	141925.61
3234	660.03	741.93	52874.08	4700.94	357137.5	357.22	520660.84	31713.99	2072.36
3235	624.08	741.35	5229.44	183.07	377620.25	219.28	599143.25	11372.92	507.55
3236	706.51	691.4	5860.22	12467.83	140437.97	1808.91	442954.97	23024.76	349196.25
3237	710.44	674	7960.38	7598	172497.09	2934.32	451466.69	18590.71	319135.16
3238	719.27	652.49	17333.87	6489.02	182492.34	1837.75	449050.13	66434.46	256946.23
3239	685.97	650.47	29644.71	3451.62	127779.22	639.51	289454.56	217185.88	43219.93
3240	651.75	651.57	197874.52	2430.48	268625.16	400.87	380464.28	25467.26	954.08
3241	602.8	650.1	9621.29	272.09	397958.94	318.72	563008.75	21694.24	762.66
3242	650.27	616.09	8448.09	1279.66	317293.66	13576.25	490002.72	25234.52	92848.31

hXRF measurement – Block 2, Layer 3 (1)

Reading No	x-Axis	y-Axis	Ca	Cu	Fe	Pb	S	Si	Zn
2748	463.73	791.15	28475.87	2387.41	227424.11	52945.45	426231.34	68879.85	151611.67
2749	580.23	795.85	28340.51	2379.16	264344.56	548.95	456400.50	26188.30	146359.23
2750	635.6	796.11	17974.99	5486.67	183588.06	902.57	465611.56	13159.14	292475.00
2751	405.74	772.36	22457.28	480.75	313813.44	5585.43	517525.59	6515.70	11311.39
2752	505	761.13	13932.16	225.95	380152.78	520.26	589972.75	7211.90	1503.63
2753	634.56	761.66	147229.33	65.09	188969.92	1109.50	215939.72	42385.23	378.11
2754	405.22	717.29	142179.52	660.08	167644.84	48390.57	278480.31	10496.67	18868.76
2755	480.45	718.07	16159.35	404.79	378032.38	5528.24	566112.69	< LOD	24962.30
2756	540.52	709.46	200918.92	670.63	90947.02	29126.72	85377.92	17247.55	33991.04
2757	635.86	717.29	136776.31	1407.38	186922.86	1200.75	239782.89	31659.04	30251.26
2758	455.89	689.36	46569.16	2035.78	295222.84	4431.44	496240.00	3816.24	105823.98
2759	549.49	685.26	78297.51	4417.58	117818.59	66377.51	334685.63	17588.97	224497.48
2760	617.91	683.16	83506.93	3331.36	164532.06	66127.94	333057.72	81693.77	167004.48
2761	402.57	685.26	25845.21	1000.35	324908.56	13844.30	504124.88	13612.44	800.22
2762	439.93	651.7	159127.28	10748.26	265333.66	3492.93	279294.59	14502.13	313.76
2763	486.1	652.54	34259.35	5769.13	74848.68	343730.47	322077.44	26892.31	44020.30
2764	553.27	650.44	59196.98	4373.72	126794.90	109420.66	319409.91	21442.90	167063.28
2765	639.74	647.93	95263.12	1993.61	242123.34	60838.68	361956.22	19115.37	57270.74
2766	469.73	631.57	154638.95	127.22	226544.33	228.18	298469.00	20080.99	309.86
2767	521.78	616.05	133237.16	368.55	292545.38	954.29	344455.44	34708.69	3742.55
2768	580.97	637.44	26034.00	2698.79	263412.03	72178.06	463221.03	26200.18	111004.88
2769	637.64	627.79	53415.22	6904.95	372839.16	462.91	500894.00	13911.43	837.28

hXRF measurement – Block 2, Layer 3 (2)

Reading No	x-Axis	y-Axis	Ca	Cu	Fe	Pb	S	Si	Zn
2771	725.14	855.57	116975.55	25926.29	283720.13	432.26	366527.09	19943.25	422.81
2772	781.79	853.68	30537.95	241.12	372222.59	366.48	560068.69	10655.37	303.61
2773	722.44	824.03	127900.45	364.44	300620.53	11867.15	402475.59	< LOD	139.11
2774	779.36	822.41	104239.74	2140.24	336723.72	384.13	446332.28	7566.15	3323.50
2775	687.38	791.15	87672.63	518.25	351965.81	203.89	446351.28	< LOD	75.94
2776	730.27	789.26	112376.00	140.21	339805.19	830.36	438563.84	9856.43	177.59
2777	781.25	789.53	42700.27	693.78	67506.17	426.80	164558.16	319654.53	59.61
2778	688.19	764.47	61601.52	452.46	342444.84	4366.76	478795.66	9092.19	347.41
2779	729.19	760.96	93066.37	3398.75	273828.41	12208.77	416845.91	86946.60	1390.83
2780	779.36	766.08	63980.99	1289.80	340247.84	16320.86	491699.41	35644.05	559.61
2781	676.78	734.41	138121.02	467.76	244778.75	27731.36	327298.34	3750.78	6645.29
2782	733.54	733.05	118568.09	308.87	312161.19	35804.50	395971.66	6688.34	72.41
2783	778.63	728.43	59731.58	417.58	379435.78	6339.72	508117.25	12719.87	183.97
2784	675.15	677.14	111675.84	312.63	289901.34	43229.23	384279.22	14573.83	105.62
2785	733.27	679.86	115923.66	1195.20	279608.13	31667.78	329685.53	10450.12	1026.21
2786	779.99	680.94	103099.80	245.32	328770.72	32353.99	435631.63	9597.97	< LOD
2787	674.06	634.81	89719.94	547.33	347959.31	5312.60	383995.50	6363.62	618.33
2788	722.41	635.08	91511.68	1813.20	349865.47	7916.93	437106.84	5570.11	499.54
2789	779.44	632.09	120442.10	948.39	270204.22	52928.34	343698.88	22229.60	897.44
2790	675.19	593.01	94875.21	190.07	323217.78	23089.48	413354.34	26642.85	160.15
2791	736.45	598.75	131479.83	3163.50	212446.70	93873.48	272246.13	23422.95	572.78
2792	769	597.39	148311.53	1417.96	291886.97	1941.37	343635.19	25797.24	94.36

hXRF measurement – Block 2, Layer 6 (1)

Reading No	x-Axis	y-Axis	Ca	Cu	Fe	Pb	S	Si	Zn
2920	439.24	783.01	167696.92	261.67	136965.50	73504.51	179018.02	22065.02	6568.39
2921	519.05	787.9	92820.18	204.16	336468.10	255.46	387500.53	13844.86	1258.58
2922	629.36	782.63	62744.29	543.72	337386.70	3444.77	455133.50	50059.77	4238.86
2923	445.26	746.89	35705.82	5443.91	157078.20	4417.76	424311.75	23249.10	290297.56
2924	517.55	737.11	15922.53	1052.02	373788.40	17222.88	575055.13	< LOD	12227.46
2925	562.35	738.99	7429.15	2845.43	162275.50	1319.90	462193.19	8093.69	324999.44
2926	637.27	742	14684.27	736.14	369950.60	3047.61	549601.81	11521.65	29742.93
2927	550.3	700.25	125884.45	3393.74	91847.68	20471.45	179382.63	13194.72	199520.83
2928	436.98	678.05	53048.91	864.40	360634.60	20008.40	529716.13	8972.55	388.25
2929	480.27	679.18	121328.70	1550.38	241887.10	22266.49	332256.13	8952.24	70007.33
2930	643.29	681.44	58278.50	11718.79	102503.30	118792.61	338150.69	17133.71	288535.56
2931	532.06	662.35	26887.14	1048.46	290100.30	97556.52	483611.31	37087.55	42374.36
2932	600.45	660.07	25595.61	6429.60	100705.00	108321.41	376145.84	18631.75	216444.27
2933	473.55	644.13	16117.16	2948.65	367419.30	14097.66	576641.06	10233.40	3973.02
2934	624.01	646.03	77157.16	4519.88	231453.50	22564.93	374595.31	9634.91	114588.13
2935	473.55	628.94	172368.67	3230.21	210523.40	925.85	247611.55	17737.82	10584.35
2936	503.94	629.32	179488.91	3624.43	122085.90	705.70	86573.01	164217.11	491.90
2937	582.21	627.42	24637.57	3995.49	242823.60	35978.00	474787.69	6198.22	176160.03

hXRF measurement – Block 2, Layer 6 (2)

Reading No	x-Axis	y-Axis	Ca	Cu	Fe	Pb	S	Si	Zn
2938	644.15	630.46	20064.72	3984.15	249903.88	22215.82	515864.88	21533.18	156149.40
2939	548.4	611.1	4890.67	488.66	14861.14	1125.35	50416.74	538903.44	6671.26
2940	624.01	606.16	20971.51	11723.52	134243.48	12824.35	407726.75	23394.08	347833.80
2941	761.87	830.51	44935.06	521.48	379011.66	223.68	496249.47	17523.30	400.21
2942	717.86	831.46	59236.21	246.43	383328.78	169.92	542655.75	3986.47	75.30
2943	738.91	793.71	84904.27	1273.47	358370.03	6087.36	465031.09	8100.69	681.59
2944	718.1	794.66	102434.46	1809.55	342345.38	638.46	461090.97	9733.96	471.52
2945	687.01	798.25	67484.70	234.29	199467.97	490.23	375370.06	207379.17	320.60
2946	752.54	769.81	101773.24	235.57	323687.41	1744.68	441678.19	6841.87	188.98
2947	690.36	772.91	89174.62	253.00	362191.66	1430.98	458731.72	10532.86	750.06
2948	748.84	734.33	74709.87	257.05	371064.69	2025.12	516195.06	9713.75	299.24
2949	719.95	733.27	110896.07	1520.86	150933.72	183370.94	293879.75	21337.34	23045.34
2950	702.86	737.05	30671.56	4407.50	67278.52	320388.00	361479.94	25017.85	63129.35
2951	749.9	707.28	110432.19	207.25	324360.25	6976.11	424003.09	11715.88	238.35
2952	719.5	706.37	120365.39	7301.40	262033.69	41063.27	344322.22	7170.64	4375.27
2953	700.44	708.49	114407.97	263.60	295346.53	24249.12	369457.81	7355.07	1042.35
2954	720.29	672.48	92052.89	176.01	346907.28	7111.25	458162.84	25928.68	402.15
2955	718.15	644.27	91372.80	126.51	361561.78	588.86	479228.13	12970.07	183.05
2956	683.96	645.03	94055.64	257.20	351132.88	451.15	472256.06	11611.24	183.01
2957	717.57	608.78	127802.63	1440.92	337929.31	9038.80	379640.19	16209.97	137.49

Annex I. Recalibration h-XRF

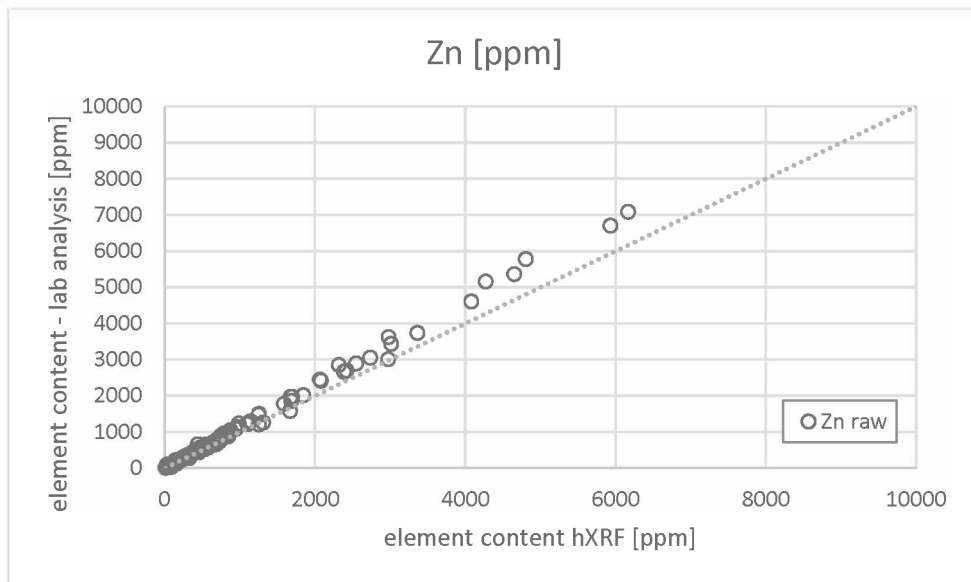


Figure Annex I-1: Comparative hXRF measurements: field-, cup- and chemical-analytical from lab analysis I – Zinc (Zn)

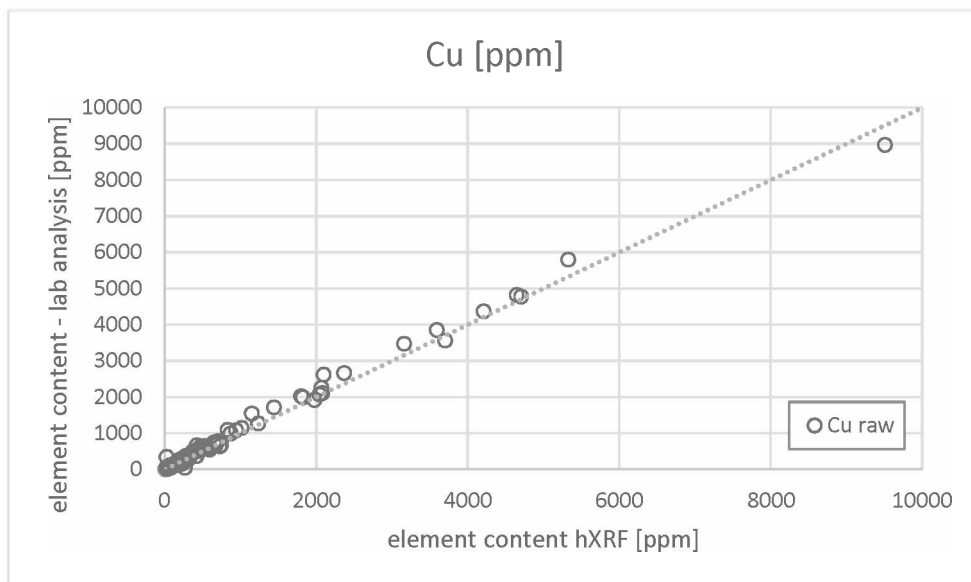


Figure Annex I-2: Comparative hXRF measurements: field-, cup- and chemical-analytical from lab analysis I – Copper (Cu)

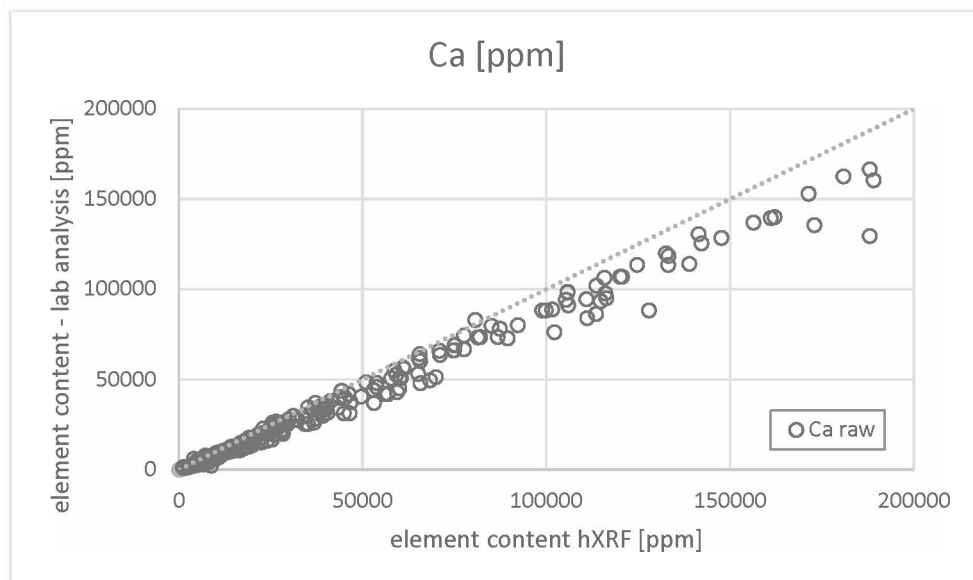


Figure Annex I-3: Comparative hXRF measurements: field-, cup- and chemical-analytical from lab analysis I – Calcium (Ca)

Annex J. Ore recovery

Block 1, Depth of Cut 4 mm

Forces	Block 1 Layer 5			
	Left		Right	
	Ore recovery	Dilution	Ore recovery	Dilution
6 kN	84.45	8.88	<u>44.13</u>	0
8 kN	71.53	0.30		
10 kN	58.39	0		
12 kN	44.19	0		
14kN	6.02	0		
16 kN				
18 kN				

Forces	Block 1 Layer 6			
	Left		Right	
	Ore recovery	Dilution	Ore recovery	Dilution
6 kN	80.98	9.32	72.85	6.83
8 kN	70.28	1.72	74.92	0
10 kN	59.39	0		
12 kN	47.81	0		
14kN	17.66	0		
16 kN				

Block 1, Depth of Cut 6 mm

Forces	Block 1 Layer 7			
	Left		Right	
	Ore recovery	Dilution	Ore recovery	Dilution
6 kN	66.77	3.97	61.40	8.70
8 kN	55.45	0.88	8.09	0
10 kN	42.02	3.97		
12 kN	16.21	0		
14kN				

Annex J Ore recovery

Forces	Block 1 Layer 8			
	Left		Right	
	Ore recovery	Dilution	Ore recovery	Dilution
7 kN	<u>98.18</u>	10.31	89.87	17.56
8 kN	94.44	5.60	77.99	14.60
10 kN	79.35	3.56	22.78	0
12 kN	68.04	3.27		
14kN	58.21	1.87		
16 kN	44.36	0		
18 kN	28.50	0		
20 kN	9.12	0		

Forces	Block 1 Layer 9			
	Left		Right	
	Ore recovery	Dilution	Ore recovery	Dilution
7 kN	93.06	13.56	<u>57.67</u>	9.31
8 kN	88.91	7.01	30.37	2.51
10 kN	77.77	2.92	4.00	0
12 kN	65.07	0		
14kN	52.40	0		
16 kN	38.58	0		
18 kN	80.99	0		
20 kN				

Forces	Block 1 Layer 10			
	Left		Right	
	Ore recovery	Dilution	Ore recovery	Dilution
7 kN				
8 kN	86.83	2.62	49.88	5.74
10 kN	60.78	0	5.50	0
12 kN	40.93	0		
14kN	0.62	0		
16 kN				

Annex J Ore recovery

Forces	Block 1 Layer 11			
	Left		Right	
	Ore recovery	Dilution	Ore recovery	Dilution
7 kN	72.53	4.57	93.42	35.19
8 kN	61.67	1.28	82.31	25.12
10 kN	37.72	0	56.91	17.28
12 kN	5.43	0	4.06	0

Block 2, Depth of Cut 6 mm

Forces	Block 2 Layer 3			
	Left		Right	
	Ore recovery	Dilution	Ore recovery	Dilution
8 kN	87.84	0	96.72	3.80
10 kN	87.84	0	84.25	0
12 kN	59.53	0	56.69	0
14 kN	16.51	0	6.66	0
16 kN				

Forces	Block 2 Layer 4			
	Left		Right	
	Ore recovery	Dilution	Ore recovery	Dilution
8 kN	68.86	0	97.13	3.78
10 kN	8.03	0	97.81	0
12 kN			85.29	2.46
14 kN			64.18	0
16 kN			41.91	0
18 kN			12.73	0
20 kN				

Forces	Block 2 Layer 5			
	Left		Right	
	Ore recovery	Dilution	Ore recovery	Dilution
8 kN	79.20	1.67	77.88	0
10 kN	43.17	0	31.18	0
12 kN	14.55	0	5.58	0
14 kN				

Annex J Ore recovery

Block 1, Depth of Cut 8 mm

Forces	Block 2 Layer 6			
	Left		Right	
	Ore recovery	Dilution	Ore recovery	Dilution
10 kN	93.79	11.11	99.13	0.86
12 kN	79.35	2.30	92.49	0
14 kN	51.14	0	79.96	3.77
16 kN			43.09	0
18 kN				

Forces	Block 2 Layer 7			
	Left		Right	
	Ore recovery	Dilution	Ore recovery	Dilution
10 kN	93.96	1.51	98.23	8.58
12 kN	72.35	0.54	95.04	2.31
14 kN	42.06	0	64.64	0
16 kN			51.33	0
18 kN			34.57	0
20 kN			21.44	0

Forces	Block 2 Layer 8			
	Left		Right	
	Ore recovery	Dilution	Ore recovery	Dilution
10 kN	92.20	2.27	90.75	18.81
12 kN	59.41	0	86.69	10.93
14 kN	30.28	0	80.55	2.82
16 kN	4.54	0	66.72	0
18 kN			46.45	0
20 kN			26.65	0

Forces	Block 2 Layer 9			
	Left		Right	
	Ore recovery	Dilution	Ore recovery	Dilution
10 kN	82.90	16.47	90.99	22.97
12 kN	47.93	2.13	81.58	10.00
14 kN	26.56	0	69.34	18.72
16 kN	7.38	0	52.12	5.09
18 kN			24.15	0
20 kN			6.97	0

Annex K. Technical data of concrete

Technisches Merkblatt

PCI Repaticw®

Daten zur Verarbeitung/Technische Daten

Materialtechnologische Daten

Materialbasis	Quarzsande, schwundkompensierte Zemente, Zusatzstoffe, Zusatzmittel
Komponenten	1-komponentig
Konsistenz/Farbe	pulvrig/grau
Dichte des angemischten Mörtels	ca. 2,3 g/cm ³
Größtkorn	1 mm
Brandschutzklasse	A1fl nach DIN EN 13501-1
Lagerfähigkeit	mind. 6 Monate
Lagerung	trocken, nicht dauerhaft über + 30 °C lagern
Lieferform	25-kg-Kraft-Papiersack Art.-Nr./EAN-Prüfz. 1406/6
Einstufung gemäß DAfStb VeBMR R11	
Fließmaßklasse	F3 (≥ 750 mm)
Schwindklasse	SKVM I
Frühfestigkeitsklasse	A (≥ 40 N/mm ² nach 24h)
Druckfestigkeitsklasse	C 60/75
Expositionsklasse gemäß EN 206	XO, XC4, XD3, XS3, XF3, XA2

Anwendungstechnische Daten

Verbrauch/Ergiebigkeit	25 kg sind ausreichend für einen Hohlraum von ca. 12 Liter.				
Verarbeitungstemperatur	+ 5 °C bis + 30 °C				
Vergusshöhe	5 bis 100 mm				
Anmachwasser für	- 1 kg Pulver	145 ml			
	- 25 kg Pulver	3,6 l			
Mischzeit	ca. 3 Minuten				
Misch-/Fördertechnik	z. B. Fa. M-TEC P20, Fa. PFT Swing K bzw. XP3 XL, Fa. Putzmeister S5, Fa. Ützener S30 HD40				
Verarbeitbarkeitsdauer*	ca. 90 Minuten				
Aushärtezeit*	- Entfernen der Schalung nach	ca. 12 Stunden			
	- Inbetriebnahme von Maschinen nach	ca. 24 Stunden			
Temperaturbeständigkeit nach Aushärtung	- 30 °C bis + 80 °C				
Nachbehandlung	Frei liegende Mörtelflächen mit feuchten Tüchern oder Polyethylenfolie vor Austrocknung schützen.				
Fließmaß*(Rinne)	sofort	5 min	30 min	60 min	90 min
Ausbreitmaß*	≥ 800 mm	≥ 800 mm	≥ 800 mm	≥ 780 mm	≥ 780 mm
Quellmaß* nach	≥ 250 mm	≥ 250 mm	≥ 240 mm	≥ 240 mm	≥ 240 mm
Druckfestigkeit* DIN EN 196-1	24 h ≥ 0,1 Vol%				
(Prisma 4 x 4 x 16 cm)	24 h	7 d	28 d	90 d	
Biegezugfestigkeit*	≥ 55 N/mm ²	≥ 80 N/mm ²	≥ 90 N/mm ²	≥ 95 N/mm ²	
E-Modul*(dynamisch)	≥ 7 N/mm ²	≥ 10 N/mm ²	≥ 10 N/mm ²	≥ 10 N/mm ²	
	≥ 40.000 N/mm ²				

* Bei + 23 °C und 50 % relativer Luftfeuchtigkeit, höhere Temperaturen verkürzen, niedrigere Temperaturen verlängern diese Zeiten. Alle angegebenen Prüfdaten sind Anhaltswerte.